13
4-28-97 J-2 ①

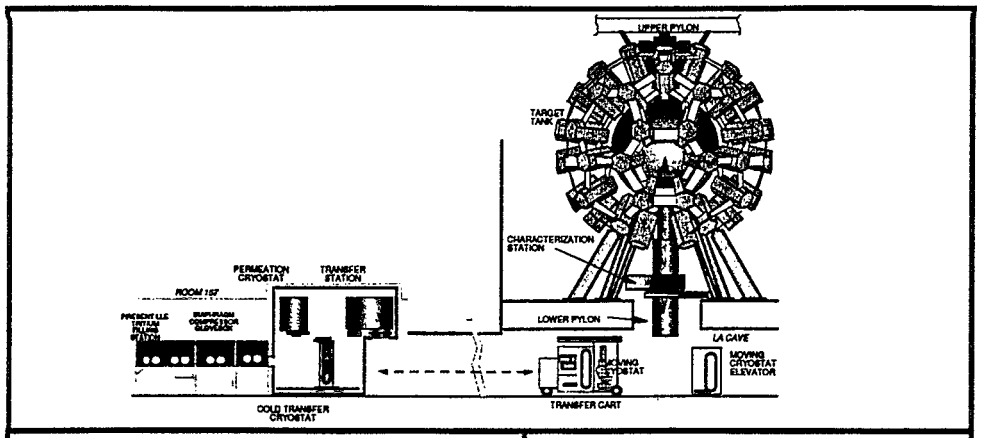

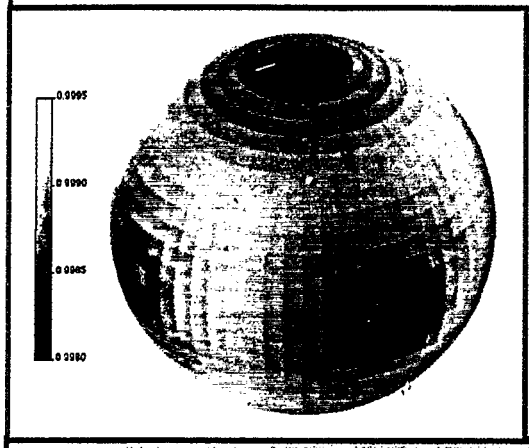

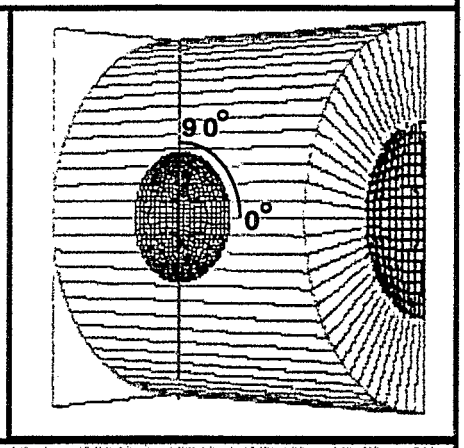

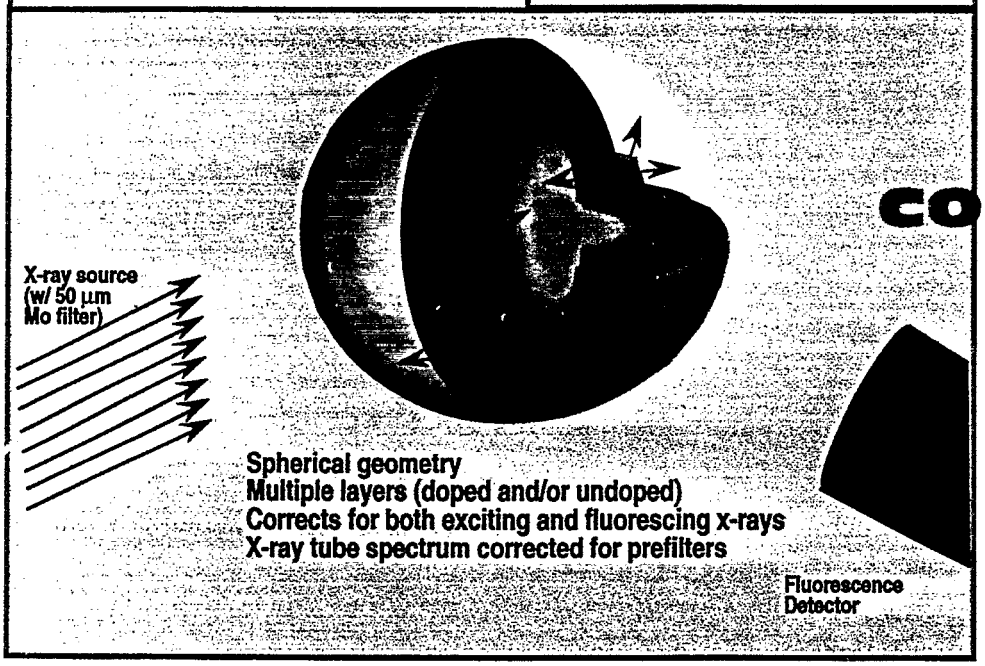

INERTIAL CONFINEMENT FUSION

ANNUAL REPORT

OCTOBER 1, 1995
THROUGH
SEPTEMBER 30, 1996

W.J.S.A.
W. J. SCHAFER ASSOCIATES, INC.

Soane Technologies Inc.

GENERAL ATOMICS

GA–A22549
UC-712

INERTIAL CONFINEMENT FUSION TARGET COMPONENT FABRICATION AND TECHNOLOGY DEVELOPMENT SUPPORT

ANNUAL REPORT TO THE U.S. DEPARTMENT OF ENERGY

OCTOBER 1, 1995 THROUGH SEPTEMBER 30, 1996

by
PROJECT STAFF
Martin Hoppe, Editor

Work prepared under
Department of Energy
Contract No. DE-AC03-95SF20732

DISTRIBUTION OF THIS DOCUMENT IS UNLIMITED

GENERAL ATOMICS PROJECT 3748
DATE PUBLISHED: FEBRUARY 1997

MASTER

GENERAL ATOMICS

DISCLAIMER

Portions of this document may be illegible in electronic image products. Images are produced from the best available original document.

DISCLAIMER

This report was prepared as an account of work sponsored by an agency of the United States Government. Neither the United States Government nor any agency thereof, nor any of their employees, make any warranty, express or implied, or assumes any legal liability or responsibility for the accuracy, completeness, or usefulness of any information, apparatus, product, or process disclosed, or represents that its use would not infringe privately owned rights. Reference herein to any specific commercial product, process, or service by trade name, trademark, manufacturer, or otherwise does not necessarily constitute or imply its endorsement, recommendation, or favoring by the United States Government or any agency thereof. The views and opinions of authors expressed herein do not necessarily state or reflect those of the United States Government or any agency thereof.

The FY1996 Target Fabrication and Target Technology Development Team

General Atomics
San Diego, California

Neil Alexander, Wes Baugh, Chuck Beal, Gary Bentley, Dave Bernat, Gottfried Besenbruch, Karl Boline, Lloyd Brown, Sharon Considine, Don Czechowicz, Walt Egli, Fred Elsner, Chuck Gibson, Jane Gibson, Kett Gifford, Ileese Glatter-Schneir, Dan Goodin, Steve Grant, Annette Greenwood, Matt Hansink, Eric Hoffman, Martin Hoppe, Dave Husband, Jim Kaae, Greg Laughon, Roy Mangano, Barry McQuillan, Wayne Miller, Abbas Nikroo, Lonnie O'Brien, Joe Pontelandolfo, John Ruppe, Chuck Schneidmuller, Ken Schultz, Clyde Shearer, John Sheliak, Rich Stephens, Dave Steinman, Bob Stemke, Ted Torres, John Vanderzanden, Don Wall, Wane Wier, David Woodhouse.

W. J. Schafer Associates
Livermore, California

Tom Alberts, Thom Bahrs, Don Bittner, John Burmann, Frank Carey, Andrea Denton-Paul, Steve Dropinski, Illges Faron, Scott Faulk, David Diffenderfer, Chuck Hendricks, Derek Mathews, Michael McClellan, Eric Monsler, Michael Monsler, Brian Motta, Craig Rivers, Jim Sater, Diana Schroen-Carey, Keith Shillito, Tom Walsh.

Soane Technologies, Inc.
Hayward, California

Travis Boone, Lisa Cheung, Don Nelson, Thai Nguyen, Sue Carter.

ABSTRACT

On December 30, 1990, the U.S. Department of Energy entered into a contract with General Atomics (GA) to be the Inertial Confinement Fusion (ICF) Target Component Fabrication and Technology Development Support contractor. In September 1995 this contract ended and a second contract was issued for us to continue this ICF target support work. This report documents the technical activities of the period October 1, 1995 through September 30, 1996. During this period, GA and our partners WJ Schafer Associates (WJSA) and Soane Technologies, Inc. (STI) were assigned 14 formal tasks in support of the Inertial Confinement Fusion program and its five laboratories. A portion of the effort on these tasks included providing direct "Onsite Support" at Lawrence Livermore National Laboratory (LLNL), Los Alamos National Laboratory (LANL), and Sandia National Laboratory Albuquerque (SNLA). We fabricated and delivered over 800 gold-plated hohlraum mandrels to LLNL, LANL and SNLA. We produced nearly 1,200 glass and plastic target capsules for LLNL, LANL, SNLA and University of Rochester/Laboratory for Laser Energetics (UR/LLE). We also delivered over 100 flat foil targets for Naval Research Lab (NRL) and SNLA in FY96. This report describes these target fabrication activities and the target fabrication and characterization development activities that made the deliveries possible.

The ICF program is anticipating experiments at the OMEGA laser and the National Ignition Facility (NIF) which will require capsules containing cryogenic layered D_2 or deuterium-tritium (DT) fuel. We are part of the National Cryogenic Target Program to create and demonstrate viable ways to generate and characterize cryogenic layers. Substantial progress has been made on ways to both create and characterize viable layers.

During FY96, significant progress was made in the design of the OMEGA Cryogenic Target System that will field cryogenic targets on OMEGA. This included major design changes, reduction in equipment, and process simplifications.

This report summarizes and documents the technical progress made on these tasks.

TABLE OF CONTENTS

1. TARGET FABRICATION PROGRAM OVERVIEW 1–1

1.1. Introduction 1–1

1.2. LL01 Onsite Support for LLNL 1–1

1.3. LL02 Micromachined Target Components 1–2

1.4. LL03/LA02/UR01 Composite Polymer Capsules 1–3

1.5. LA01 Onsite Support for LANL 1–8

1.6. NR01 NRL Target Deliveries 1–8

1.7. SL01 Fabrication of Foils, Hohlraums, and Deuterated Films 1–9

1.8. UR02 Shell Characterization Development 1–10

1.9. CR/LL1 Cryogenic Layering Development 1–10

1.10. CR/LL2 Foam Shell Development 1–11

1.11. CR/LA1 Beta Layering Support at LANL 1–12

1.12. CR/LA2 DT Layering Characterization by NMR 1–12

1.13. CR/UR1 OMEGA Cryogenic Target System Engineering 1–13

2. COMPOSITE POLYMER CAPSULE DEVELOPMENT AND PRODUCTION 2–1

2.1. Poly(alpha-methylstyrene) Shell Production and Development 2–1

2.1.1. Overview of PAMS/GDP Process 2–1

2.1.2. Production Parameters for OMEGA PAMS Shells 2–5

2.2. Polystyrene Shells by Microencapsulation 2–6

2.2.1. Production of Polystyrene Shells for OMEGA 2–6

2.2.2. Development of Chlorine-Doped Shells for OMEGA 2–7

2.3. Coatings Fabrication — Doped GDP Coatings 2–12

2.4. Characterization 2–19

2.4.1. Precise Outer-Diameter Measurements 2–19

2.4.2. Determination of Wall Thickness by Mass 2–21

2.4.3. Twenty-Six Point Measurement of Capsules 2–22

TABLE OF CONTENTS (CONTINUED)

2.4.4. Improved X-Radiography 2–25
2.4.5. XRF Calibration 2–29

2.5. References 2–33

3. MICROMACHINED TARGET COMPONENTS 3–1

3.1. "Top Hat" Aluminum Witness Plates 3–1

3.2. Thin-Walled Tubes 3–4

3.3. Thin Copper Discs With a Bessel Function-Shaped Dimple 3–7

3.4. Deuterated Polyethylene Films for Sandia Targets 3–9

4. NIKE TARGET DELIVERIES 4–1

4.1. Thickness Uniformity 4–1

4.2. Thickness Control 4–2

4.3. Leveling 4–4

4.4. Aluminum Coating 4–5

5. CRYOGENIC SCIENCE AND TECHNOLOGY DEVELOPMENT 5–1

5.1. CR/LL1 Cryogenic Layering Development 5–1

5.1.1. Smoothing of DT Ice by Electrical Heating of the Saturated Vapor 5–1
5.1.2. IR Heating Surface Roughness Experiments 5–10
5.1.3. Modeling of Surface Roughness for IR Heating 5–14
5.1.4. Modeling of IR Illumination Schemes Inside a Hohlraum 5–14

5.2. Beta-Layering Support at LANL 5–18

5.3. IR Layering Sphere 5–23

5.4. Foam Shell Development 5–28

5.4.1. Aerogel Foam Shell Production 5–28
5.4.2. Shell Overcoating 5–30

5.5. References 5–33

TABLE OF CONTENTS (CONTINUED)

6. OMEGA TARGET SYSTEM ENGINEERING 6–1

6.1. D_2 Equipment Testing 6–2

6.2. DT Equipment Design 6–4

6.2.1. Fill Station 6–4
6.2.2. Cold Transfer System 6–5
6.2.3. Transfer Station 6–7
6.2.4. Cryogenic Target Positioning System 6–8

7. PUBLICATIONS 7–1

LIST OF FIGURES

Fig. 1–1. Cumulative deliveries for glass and composite capsules 1–7

Fig. 2–1. Fit of experimental data to PVA flow equation..... 2–5

Fig. 2–2. Interference patterns from target-quality 9 × 900 μm polystyrene shells produced via controlled-mass microencapsulation..... 2–7

Fig. 2–3. Photographs of solidified ~900 μm diameter poly(4-chlorostyrene) shells with 8 μm and 16 μm wall thicknesses 2–9

Fig. 2–4. Cumulative yields throughout the microencapsulation processing of 16 x 900 μm shells produced with poly(4-chlorostyrene) with 28 K MW/2.0 PD and 346 MW/9.52 DP..... 2–10

Fig. 2–5. Bubble formation during sonication of 14 x 980 μm poly(4-chlorostyrene) shells 2–10

Fig. 2–6. Effect of sonication on final structural yield of 14 x 980 μm poly(4-chlorostyrene) shells 2–11

Fig. 2–7. Comparison of the survivability of 14 x 980 μm shells of P_4ClS and PClMS..... 2–12

Fig. 2–8. Qualitative plot of the effect of mixing chlorinated hydrocarbons with T2B and hydrogen..... 2–13

Fig. 2–9. Chlorine concentration as a function of coating thickness for chlorobutene films 2–14

Fig. 2–10. Precision of OD measurement procedure is very good 2–20

Fig. 2–11. Unnoticed previously, measurements of composite capsule over time show that dimensions may change with age 2–21

Fig. 2–12. Roll pattern used in our 26 point wall measurement experiments 2–23

Fig. 2–13. Determination of change in optical path length between inner and outer surfaces 2–23

Fig. 2–14. Operating the microscope x- and y-axis stage positioner controls allows us to roll the capsule to any desired orientation 2–24

LIST OF FIGURES (CONTINUED)

Fig. 2–15. (a) Single radial second derivative line, from the old method..... 2–27

Fig. 2–16. Calculating local derivatives for ZQuad 2–28

Fig. 2–17. Radial profile produced by the new ZQuad..... 2–28

Fig. 2–18. Exponential curve fit of Si doped GDP data 2–30

Fig. 2–19. Theoretical model includes explicit corrections for XRF calibration.. 2–31

Fig. 2–20. Calculated intensity of the resulting fluorescence spectrum for targets with an undoped inner mandrel 2–33

Fig. 2–21. Model data recalculated assuming a 7% decrease in Si concentration.. 2–34

Fig. 3–1. Illustration of "Top Hat" witness plate configuration 3–2

Fig. 3–2. Sketch of Top Hat attached to an arbor 3–2

Fig. 3–3. Tool interference drawing 3–3

Fig. 3–4. Photo of finished Top Hat 3–3

Fig. 3–5. Illustration of a thin-walled gold tube with a tapered wall thickness 3–4

Fig. 3–6. Schematic of setup for plating in the diamond turning machine..... 3–5

Fig. 3–7. Photo of small gold tube with tapered wall thickness 3–5

Fig. 3–8. Drawing of gold and silver tube..... 3–6

Fig. 3–9 Photo of gold and silver tube..... 3–7

Fig. 3–10. Drawing of disc with dimple 3–8

Fig. 3–11. Sketch of copper disc on mandrel 3–9

Fig. 3–12. Profile of dimple compared to a Bessel Function 3–9

Fig. 3–13. SABRE target design for deuterated polyethylene films..... 3–11

Fig. 3–14. PBFA-II target design for deuterated polyethylene films..... 3–11

LIST OF FIGURES (CONTINUED)

Fig. 4–1. Acrylic boat used to float wafers in ultrasonic tank 4–2

Fig. 4–2. Graph of casting thickness vs. mass ratio for obtaining desired film thickness 4–3

Fig. 4–3. Diagram of method used to level castings with laser beams. 4–4

Fig. 5–1. DT ice layer before heating of the DT gas inside the cell 5–4

Fig. 5–2. Geometry and variables used in the analysis of the layering rate 5–5

Fig. 5–3. Layering rates corrected for DT age vs. rf power applied to the cavity 5–6

Fig. 5–4. DT ice layer after rf heating of the DT gas in the cell. 5–8

Fig. 5–5. Comparison of the power spectra of the DT ice surface before and after heating 5–9

Fig. 5–6. S_n vs. rf power for several n 5–9

Fig. 5–7. Sketch of the experimental layout 5–11

Fig. 5–8. Optical path depth interferograms of HD layers formed by ~50 mW of non-smoothed and smoothed 2.57 μm radiation 5–11

Fig. 5–9. Surface roughness decreases as the heating rate increases to 400 mW/cm^3 5–12

Fig. 5–10. IR smoothed layers have a similar spectral shape to D-T 5–13

Fig. 5–11. IR temperature gradient for a 100 μm thick layer with various sinusoid amplitudes 5–15

Fig. 5–12. Geometry of the tiled enclosure comprising 1/4 of hohlraum 5–16

Fig. 5–13. Intensity entering the shell due to equal power emitted from various regions 5–17

Fig. 5–14. Linear combination of intensity distributions 5–17

Fig. 5–15. Surface roughness evolution for native beta-layered DT solid layers at 19.65 K and 18 K, and for a DT solid layer smoothed with 1.125 mW heater power. 5–18

Fig. 5–16. Time evolution for DT solid surface roughness at 19 K and 19.5 K, for 80 μm and 130 μm solid layer thicknesses for native beta-layering 5–19

LIST OF FIGURES (CONTINUED)

Fig. 5–17. D_2 solid layer freeze/thaw cycling at 0.5 mW heater power and 18 K equilibration temperature 5–20

Fig. 5–18. D_2 solid layer facet/smooth cycling at 18 K, zero faceting power and smoothing powers from 2.0 mW to 0.25 mW 5–21

Fig. 5–19. D_2 solid layer equilibration power stepping at 18 K 5–22

Fig. 5–20. Low power defaceting of a D_2 solid layer surface at 18 K 5–23

Fig. 5–21. Calculated brightness map of interior of integrating sphere 5–24

Fig. 5–22. Power absorbed in (a) the plastic layer, and (b) the ice layer as a function of the angle between the source and the local surface normal . 5–25

Fig. 5–23. Normalized heat input into (a) plastic layer and (b) ice layer as a function of location on the cryotarget 5–26

Fig. 5–24. SEM micrographs of the interfacial polymer layers 5–31

Fig. 5–25. Interferograms showing the extreme thinness of the interfacial walls, and the high degree of uniformity across the wall 5–31

Fig. 5–26. Change in surface finish that can be attained by changing the rinsing protocol 5–32

Fig. 5–27. SEM micrograph shows the surface finish of a thin wall 5–33

Fig. 6–1. Filled shells have distinctive appearance 6–3

Fig. 6–2. DT fill station 6–4

Fig. 6–3. The overall layout of the Cold Transfer System with one of the Cold Transfer Cryostats removed 6–6

Fig. 6–4. A cold transfer cryostat shown with shroud partially extended 6–7

Fig. 6–5. Transfer station 6–8

LIST OF TABLES

1–1. FY96 target fabrication tasks 1–2

1–2. NOVA and OMEGA capsule requirements 1–4

1–3. NIKE NRL target deliveries 1–8

2–1. Desired OMEGA shell specifications and delivered values 2–7

2–2. Chlorinated polymers obtained and characterized for development 2–8

2–3. Chlorinated hydrocarbons used in the experiments and the maximum chlorine concentration obtained with each dopant 2–13

2–4. Possible precursors for transition metal doped GDP 2–16

2–5. Shrinkage of GDP films after pyrolysis as a function of doping 2–18

5–1. Combinations of interior and exterior oil phases 5–29

DISCLAIMER

This report was prepared as an account of work sponsored by an agency of the United States Government. Neither the United States Government nor any agency thereof, nor any of their employees, makes any warranty, express or implied, or assumes any legal liability or responsibility for the accuracy, completeness, or usefulness of any information, apparatus, product, or process disclosed, or represents that its use would not infringe privately owned rights. Reference herein to any specific commercial product, process, or service by trade name, trademark, manufacturer, or otherwise does not necessarily constitute or imply its endorsement, recommendation, or favoring by the United States Government or any agency thereof. The views and opinions of authors expressed herein do not necessarily state or reflect those of the United States Government or any agency thereof.

1. TARGET FABRICATION PROGRAM OVERVIEW

On December 30, 1990, the U.S. Department of Energy entered into a contract with General Atomics (GA) to be the Inertial Confinement Fusion (ICF) Target Component Fabrication and Technology Development Support contractor. In September 1995 this contract ended and a second contract was issued for us to continue this ICF target support work. This report documents the technical activities of the period October 1, 1995 through September 30, 1996. GA was assisted by W.J. Schafer Associates (WJSA) and Soane Technologies, Inc. (STI) and we have carried out the ICF Target Fabrication tasks as a fully integrated team effort.

1.1. INTRODUCTION

In FY96, the GA/WJSA/STI team maintained previous production capabilities and added new or improved capabilities in all areas of ICF target fabrication. In addition, significant progress has been made on the development and testing of the OMEGA Cryogenic Target System Engineering project.

During FY96, the GA/WJSA/STI team was assigned 14 formal tasks, as shown in Table 1-1. These tasks are described briefly here. Additional technical detail on selected topics is given in Sections 2 through 6 of this report.

1.2. LL01 ONSITE SUPPORT FOR LLNL

Our onsite team at Lawrence Livermore National Laboratory (LLNL) was composed of Diana Schroen-Carey, Andrea Denton-Paul, Craig Rivers, Derek Mathews, and John Ruppe. They provided support in micromachining of target components, assembling target components into complete targets, and characterizing target components and capsules for their use in NOVA ICF experiments.

TABLE 1-1
FY96 TARGET FABRICATION TASKS

Task No.	Task Title Description	Total $K	Task Leader
LL01	Onsite support for LLNL	538	Miller
LL02	Micromachined target components	1,142	Kaae
LL03	Composite polymer capsules	860	Miller
LA01	Onsite support for Los Alamos National Laboratory (LANL) at LLNL	245	Miller
LA02	Composite polymer capsules	830	Miller
NR01	NRL target development	826	Hendricks
SL01	Fab. of foils, filters and polymers	810	Kaae
UR01	Polymer capsules for Laboratory for Laser Energetics (LLE)	1,460	Miller
UR02	Shell characterization development	137	Stephens
CR/LL1	Cryogenic layering development	775	Bittner
CR/LL2	Foam shell development	347	Schroen-Carey
CR/LA1	Beta layering support at LANL	281	Simpson
CR/LA2	DT layer characterization by nuclear magnetic resonance (NMR)	18	Alexander
CR/UR1	OMEGA-Upgrade target system engineering	3,990	Besenbruch
	Total	$11,690	

1.3. LL02 MICROMACHINED TARGET COMPONENTS

In FY96, this task was divided between LLNL and LANL.

For LLNL the effort was to:

1. Provide precision machined mandrels for use as target components and as coating substrates.
2. Provide supporting technologies such as electroplating, physical vapor deposition, subcomponent assembly, characterization and metrology.
3. Supply production drawings and documentation.

In FY96, we machined 702 hohlraum mandrels of 37 different varieties, then gold plated, characterized and delivered them to LLNL. In addition, 23 copper sine wave plates, 51 aluminum wedge witness plates and various sine wave profiles in copper and molybdenum were produced for LLNL.

We also produced quantities of various more complex components for LLNL. These other components consisted of:

1. "Top-hat" aluminum witness plates.
2. Thin-walled gold tubes with constant wall thicknesses.
3. Thin-walled gold tubes with tapered wall thicknesses.
4. Thin-walled gold and silver tubes with tapered wall thicknesses.
5. Small copper disks with Bessel-function-shaped dimples.

For LANL the effort was to:

1. Produce precision machined and plated hohlraum mandrels.
2. Provide supporting characterization.

In FY96, we machined 138 hohlraum mandrels of four varieties, then gold plated, characterized and delivered them to LANL.

In order to consolidate the micromachining effort, the Rocky Flats' No. 3 lathe was disassembled at WJSA, where it had been moved from Rocky Flats National Laboratory; moved to General Atomics; reassembled and made operational. Upgrades for the controller and the position encoders of this lathe were ordered. Fixtures to hold the position encoders were designed and are being fabricated at WJSA.

1.4. LL03/LA02/UR01 COMPOSITE POLYMER CAPSULES

The composite polymer capsule production process changed significantly in FY96. Previously, a typical NOVA capsule (Table 1-2) consisted of a polystyrene shell coated with a polyvinyl alcohol (PVA) permeation barrier, over-coated with a glow discharge polymer (GDP) ablation layer, and filled with a diagnostic gas, typically argon. These

capsules, although they served the NOVA program well, have several inherent limitations:

1. The inner polystyrene shell has poor wall thickness uniformity (~15% non-concentricity). The shells are made using the drop tower technique. The process has been studied and optimized for years; significant improvements in wall thickness uniformity using this technique are not likely.

2. The diameter of the inner polystyrene shell is limited to about 700 μm using the drop tower. The optimum diameter is about 450 μm. Making larger shells using the drop tower technique is not promising since wall thickness uniformity worsens as the diameter increases.

3. The wall thickness of the inner polystyrene shell has not been made thinner than about 2 μm.

4. The PVA barrier layer has very poor thickness uniformity (~40% non-concentricity).

Capsules required for OMEGA differ considerably from those required for NOVA (Table 1-2). The capsules are nearly twice the size and may have one, two, or three layers as thin as 1 μm and doped with deuterium, chlorine, silicon, germanium, or titanium.

TABLE 1-2
NOVA AND OMEGA CAPSULE REQUIREMENTS

	NOVA CAPSULE	OMEGA CAPSULE
Inner diameter	440 μm	890 μm
Inner layer thickness	3 μm	1–20 μm (depends on experiment)
Inner layer dopants	D, Cl	D, Si, Ti
Middle layer thickness	3 μm	1–20 μm (depends on experiment)
Middle layer dopants	None	D, Cl, Ge, Si, Ti
Layer thickness uniformity	≤5.0 μm (total wall)	≤0.5 μm (total wall)
Voids in layers	None allowed	None allowed
Surface finish, RMS	<1000 Å	<5000 Å (sum of modes 2–1000)

To make OMEGA capsules we had to drastically change our fabrication process; drop tower technology could not make the required large diameter shells with thin uniform walls. Thus, we adopted the GDP/PAMS approach pioneered by Steve Letts of LLNL. Letts made GDP shells by taking a bead of poly(α-methylstyrene) (PAMS) and coating it with GDP. Heating the coated bead in an inert atmosphere (i.e., nitrogen) causes PAMS to depolymerize. The monomer permeates out, leaving behind a GDP shell. Unfortunately, the GDP shell was usually deformed during the pyrolysis. With the technical assistance of Letts, the technology was transferred to GA where we substituted a hollow PAMS shell, made by microencapsulation, in place of the bead. With a PAMS shell mandrel, deformation of the resulting GDP shell is generally avoided during pyrolysis.

We applied the GDP/PAMS technique to fabricate OMEGA capsules in FY96. Several areas needing further development were identified. The most significant was the capsule shrinkage (in some cases up to 10% or more) that occurs during pyrolysis, a function of the GDP-dopant, time of pyrolysis, and other variables. If the precise amount of shrinkage is not anticipated, the finished capsule will not meet the desired diameter specification. Target delivery pressures forced us to study the shrinkage phenomenon with production shells. The experience we gained gave us the ability to roughly predict shell shrinkage and helped us to identify the variables that need to be taken into account in future experiments.

Another R&D area involving the GDP/PAMS process is the affect of pyrolysis on dopant concentration. We learned through experience that the concentration of some dopants, especially chlorine, was decreased when shells were pyrolyzed to remove the PAMS mandrel. Experiments will be conducted throughout FY97 enabling us to either anticipate or eliminate this change in dopant concentration.

One of the more notable successes of the GDP/PAMS process in FY96 was the fabrication of very thin walled shells. We fabricated 900 μm GDP shells with walls as thin as 0.8 μm. Such shells will serve as capsules for cryogenic targets for OMEGA in a few years.

OMEGA capsules also required the development of new GDP-dopants, specifically, deuterium, silicon, chlorine and titanium. The development of deuterium and silicon dopants was straightforward, perhaps because they are similar to dopants currently in use. Deuterium has the same chemical properties as hydrogen and silicon has similar chemical properties to carbon and germanium. Titanium proved to be more difficult; it is a transi-

tion metal with chemical properties unlike previous dopants. Nevertheless, we made capsules having a layer of titanium-doped GDP several microns thick. Chlorine-doped GDP was also challenging. Control of the Cl concentration is difficult, primarily due to the thermal instability of the Cl in the GDP. GDP-dopant development will continue in FY97. The number of elements we can now put into GDP layers is seven: hydrogen, deuterium, carbon, silicon, chlorine, titanium, and germanium.

We also made significant improvements in NOVA capsule fabrication. In FY96, there was a major concern that NOVA composite polymer capsules needed improved wall uniformity, measured as Δw (where, $\Delta w = wall_{max} - wall_{min}$). We employed "sizzle-coating" of shells in our GDP system in response to this need. By bounce-coating the shells very gently ("sizzling") the heavy side stays down and the deposition of GDP evens out non-uniformities due to the inner mandrel and PVA layers. In FY95, the Δw of some capsules was as high as 5.0 μm, while many capsules had a Δw of 2.0 μm or more. By the end of FY96, thanks to sizzle-coating, capsules almost always had a Δw of less than 1.5 μm and most were 0.8 μm or less.

Development of new fabrication techniques required the simultaneous development of new and improved characterization techniques. These included measuring more elements with the XRF, more precise layer thickness and diameter measurements, and improvements in measuring surface finish. These improvements will be discussed later in this report.

Target deliveries increased significantly in FY96. With OMEGA coming on line, we delivered 45% more capsules and glass shells (Fig. 1-1). Along with the increase in number and complexity, many more varieties of composite capsules were delivered. Capsules are shipped in batches, each batch having different specifications. In FY96, we shipped over 75% more batches than were shipped in FY95. In addition to "target quality" batches we also sent many samples: hundreds of polystyrene, PAMS, and GDP shells; flats and shells with doped GDP layers; foils; and special measurements.

We also streamlined our procedures to keep up with the delivery schedule for the national ICF experimental program. We employed a number of shortcuts that greatly increased our productivity. Among these are coating and processing different batches together whenever possible to save time and resources. We also developed streamlined characterization procedures, especially for layer thickness, diameter, and concentricity.

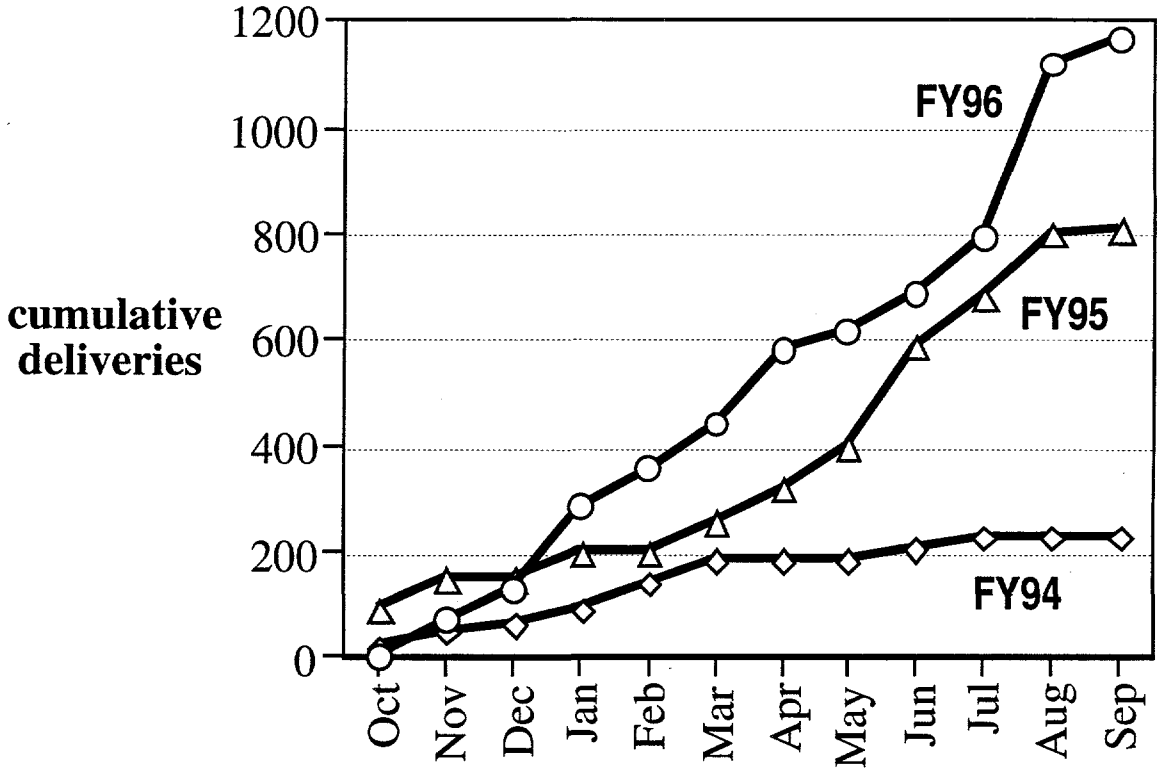

Fig. 1-1. We delivered nearly 1,200 capsules and glass shells for experiments in the national ICF program, a 45% increase. The number of types of capsules increased even more, by 76%.

In summary, our FY96 accomplishments included:

- Delivery of ~1200 composite polymer capsules and glass shells — 45% increase
- Delivery of many types of composite capsules, 80 batches, — 76% increase
- Brought the GDP/PAMS technique into production — increased shell diameter and wall thickness ranges, and improved wall uniformity
- Developed four new dopants in the GDP layer — deuterium, Si, Cl, and Ti
- Fabricated targets with an inner layer as thin as 1 μm, doped or dopant-free
- Decreased the Δw for NOVA capsules by 50%
- Fabricated 1 mm shells with 1 μm walls — critical for OMEGA cryogenic program
- Improved precision in characterization for diameter, layer thickness, and concentricity.

1.5. LA01 ONSITE SUPPORT FOR LANL

We provided two technicians to give onsite support for LANL under this task. At LLNL, Kett Gifford assembled and characterized numerous LANL targets. At LANL, starting in April, Steve Dropinski provided onsite support of target machining, assembly and characterization.

1.6. NR01 NRL TARGET DELIVERIES

During FY96 the targets listed in Table 1-3 were delivered to NRL for use in the NIKE laser program. The targets for the NIKE laser are flat hydrocarbon polymer foils with surface morphology, foil curvature, geometrical dimensions, and chemical composition which meet the specifications set forth in detail by the NIKE project team at NRL. During FY1996, WJSA has improved the quality of the NIKE laser targets shipped to NRL. Improvements have been made in areas of casting, film handling, and target foil mounting processes.

TABLE 1-3
NIKE TARGET DELIVERIES

Single foil flat targets	229
Double foil targets	62
Sin(x) targets	303
Step-ramp targets	45
Randomly rough targets	110
Aluminized targets	93
Un-cut films on silicon wafers	7
Other targets including sapphire, aluminum disk, unmounted aluminum, etc.	38
Total	887

1.7. SL01 FABRICATION OF FOILS, HOHLRAUMS AND DEUTERATED FILMS

This task consisted six subtasks, one of which was deleted in January before any work was requested by Sandia National Laboratory (SNL). These tasks were:

1. Planar Targets
2. Foam Target Components (deleted in January)
3. Hohlraums
4. Physics Package Components
5. Onsite Support
6. Deuterated Coatings.

Under the first subtask, 106 planar targets were fabricated consisting of 6.5 μm of gold coated on a 1.5 μm thick Mylar film and supported by a 2 inch diameter brass retaining ring. The gold and Mylar thicknesses were characterized and the targets were delivered to SNL.

Under the second subtask, 142 deuterated polyethylene films cast on two different stainless steel substrates were fabricated, characterized and delivered to SNL.

The SNL hohlraums are larger than those fabricated for NOVA in task LL02, but otherwise they are similar in shape and require similar gold coating thicknesses. Forty-eight hohlraums were machined, gold-plated and delivered to LLNL. There, additional machining was carried out before delivery to SNL, as we did not have the capability to do the additional machining in-house. Late in the fiscal year, we acquired a high-precision drill-press in order to do the additional machining required by SNL. Another 42 hohlraums have been machined and gold plated and are awaiting specifications from SNL before the additional machining is carried out.

Under the third subtask, 61 polycarbonate break-out plates coated with a thin layer of reflective aluminum were produced for SNL. The surface finish on these breakout plates was acceptable but an improvement in the surface finish is needed for future tests. We carried out a machining study to compare the finish obtained on polycarbonate with that obtained on acrylic. The finish obtained on acrylic was better than that on polycarbonate. Aluminum-coated break-out plate profiles were then produced in both acrylic and in polycarbonate and were sent to SNL for evaluation.

In the onsite support task, Tom Alberts was assigned full time to SNL. There he fabricated flat-foil targets to satisfy fast turnaround needs, defined needs that could be filled in task SL01, assisted with pre-test and post-test target characterization and helped with target assembly.

1.8. UR02 SHELL CHARACTERIZATION DEVELOPMENT

In FY97, cryogenic ICF targets will require characterization of their inner surfaces. As described in the FY95 annual report, we selected an optical profiler by Chapman Instruments, and verified its capabilities on flat films. Chapman was to build a version of their profiler suitable for our AFM spheremapper; we would rent and test it in FY96; and buy it in FY97. During the year, Chapman's attention was diverted by other pressing business, and the company did not build the necessary device. Our goal, to test and buy an optical head from Chapman has therefore been postponed until FY97.

Coincident with the Chapman delay, characterization of shell dopants proved to be a much thornier problem than anticipated, and at the FY96 midyear review, the task language was modified to include that as a development task. X-ray μ-fluorescence (XRF), with its unique capability to quantitatively determine concentrations of most elements simultaneously and non-destructively, and in an efficient manner, has proven to be the method of choice for total dopant ($Z > 11$) concentration within ICF capsules. Dopant homogeneity (as well as concentration) within the target can be determined using Rutherford Backscatter Spectroscopy (RBS). Other methods which have provided information are SEM/EDXS; combustion analyses; mass spectroscopy and thermogravimetric analysis (TGA).

1.9. CR/LL1 CRYOGENIC LAYERING DEVELOPMENT

High gain cryogenic targets for ICF are spherical capsules which contain a layer of DT ice surrounding a volume of DT gas in thermal equilibrium with the solid. The roughness of the inner surface of the cryogenic fuel layer inside these targets is one of the imperfections which cause implosions to deviate from perfect one-dimensional performance. Reductions in the surface roughness of this fuel layer will improve the ability of the National Ignition Facility (NIF) to achieve ignition. In FY96 we worked closely during the past year with the cryogenic group at LLNL in developing two techniques to smooth the DT ice layer.

The first technique generates a heat flux across the ice surface by applying an electric field to the DT vapor in the center of a shell. This vapor has a small but significant conductivity due to ionization caused by β-decay of tritium in the vapor and the solid. The oscillating electric field causes energy deposition in the gas ("Joule heating"). We performed experiments using a 1.15 GHz microwave cavity to apply an electric field to frozen DT inside a sapphire test cell. The cell and cavity geometries allow visual observation of the frozen layers. We find that the resulting heat flux reduces the overall roughness of the ice surface by at least a factor of three from that of native β-layering alone.

The second technique uses monochromatic infrared radiation to selectively heat rotational-vibrational bands of specific molecular hydrogen isotopes (D_2 in this experiment). This smoothing technique causes volumetric heating of the ice layer and is an analog of the β-layering technique. IR heating has an advantage in that the amount of heat generated inside the bulk ice layer is not limited by the β-decay of tritium. This technique is the only known solid layering technique for non-tritiated hydrogen. Planar layers as smooth as 0.3 μm rms have been generated with this technique.

This task also supported a modeling effort to assist in layer development; a study of modal dependence of smoothing ability for bulk heating (β-layering and IR heating); and a study of the smoothing ability of a surface heat flux (joule heating). We have also started looking at issues concerning fielding of the IR technique for an indirect drive target and examined uniform illumination schemes of a shell mounted inside a hohlraum.

1.10. CR/LL2 FOAM SHELL DEVELOPMENT

FY96 was the third year of a joint task with LLNL to produce foam capsules appropriate for current cryogenic layering experiments and candidate targets for the future National Ignition Facility. The capsule designs specified hollow spherical interiors, 90 to 100 μm foam walls, 5 to 10 μm solid barrier overcoats and final diameters of 1 to 2 mm. Areas of concern included optical transparency, wall uniformity and sphericity, and final surface finish. During FY94, we began foam shell production by building droplet generator microencapsulation facilities. We also determined that Resorcinol-Formaldehyde (RF) could produce foam walls with the required optical transparency. During FY95, we developed production capability for RF foam shells. In FY96, we focused upon the development of the solid barrier layer. The technique chosen for applying the barrier overcoat was interfacial polymerization.

The technical report in Section 5.4 describes the matrix of experiments undertaken to determine the range of properties we can expect from the barrier overcoats produced by interfacial polymerization. The range of wall thicknesses was from sub-micron to 150 microns, uniformity in some cases was excellent, and surface finish ranged from tens to hundreds of nanometers. The surface finish was not optimized, especially for thicker walls, but we have determined what experiments are required to further that goal. The chemistry used was the reaction of an acid chloride (in an organic phase) with an amine or hydroxide (in the aqueous phase). This is well established chemistry, but we undertook a novel approach. We used mixtures of small molecules and polymers as the reactants in the aqueous phase. This allowed us to adjust the wall thickness by adjusting the cross-link density in the polymer wall that was formed. A polymer with a high cross-link density restricts diffusion of the reactant molecules through it resulting in a self-limiting reaction that can produce very uniform walls of predetermined thickness.

1.11. CR/LA1 BETA LAYERING SUPPORT AT LANL

The FY96 beta-layering work at LANL included both D_2 and DT solid layering experiments in 2 mm toroidal cells using an internal heater for solid layer smoothing. Two separate 2 mm toroidal cells of the same type and configuration were used in these experiments, with the newer cell modified to reduce dead volume and allow individual temperature control of the layering cell and D_2/DT fill line. We used these cells to measure D_2 and DT solid surface RMS roughness and layering rate constants. The two toruses were designed to minimize the "light piping" effect observed in earlier 1 mm torus experiments where it was found that light transmitted by the solid layer dramatically reduced layer edge contrast, making it difficult to accurately define edges and thereby surface roughness. Further, the cell contains an axial heater to allow solid D_2 and DT layering and smoothing. The effects of equilibration temperature and layer thickness on surface roughness and roughness evolution were determined. The results of these layering experiments are presented in Section 5.2.

1.12. CR/LA2 DT LAYERING CHARACTERIZATION BY NMR

This task was to characterize samples of D-T undergoing beta-layering symmetrization for possible isotopic fractionation. A doubly tuned, 1-dimensional (1-D) spatially resolved NMR probe is to be used for this study. By resonating the probe with

the deuteron and triton resonant frequencies, it is possible to determine the ratio of deuterium to tritium with respect to location within the sample.

The NMR probe was successfully completed at the end of FY95. Unfortunately, before the probe could be used in a fractionation experiment, the NMR spectrometer was moved to a facility that was not tritium compatible. This relocation was the result of an internal LANL re-organization which left the experiment with neither a spectrometer nor a site. A tentative new site was located at LANL's Tritium Systems Test Assembly (TSTA) building. Options were investigated for finding a replacement spectrometer. A report was written recommending a Tecmag spectrometer with Oxford Instruments 4.7 tesla superconducting NMR magnet as a suitable replacement. This would cost approximately $174,000. A final decision regarding this recommendation remains to be made.

1.13. CR/UR1 OMEGA CRYOGENIC TARGET SYSTEM ENGINEERING

A number of significant accomplishments were achieved in FY96 in the area of process testing and equipment design. The prototype fill station and cold transfer cryostat were operated at General Atomics with D_2 to demonstrate the process of high pressure filling and transport of cryogenic targets and to provide input to the DT equipment design. Significant progress was also made in the design of the OMEGA Cryogenic Target System, including major design changes, reduction in equipment, and process simplifications.

The major project milestone entitled "Filled Shell Performance Demonstration" was successfully completed with D_2 filling of GDP polymer targets to high pressures (~1100 atm), condensing the D_2 below 31 K, removing the targets from the Fill Station and cryogenically transporting them in the Cold Transfer Cryostat. These tests demonstrated the feasibility of high pressure filling, cooling, and transporting of cryogenic polymer targets with the UR/LLE C-mount design.

Based on the results of prototype equipment testing, major design changes were made for the DT production equipment. In completing these changes, special emphasis was placed on simplifying the process and equipment to improve operation and maintenance, increasing reliability and safety, and reducing equipment cost. A major change in the overall system occurred when the decision was made to move the Transfer Station from La Cave under the target chamber to room 157 and place it in the same glove box as the

Fill Station. This requires using the Moving Cryostats to transfer individual targets from Room-157 to La Cave. Making this change reduces congestion under the target tank and will make operation of the Transfer Station independent of target shots since it is no longer in La Cave. A second major design change was the decision to insert and remove targets through the bottom of the cryostats to simplify maintenance.

Details of the progress on the Omega Cryogenic Target System Engineering tasks can be found in Section 6.

2. COMPOSITE POLYMER CAPSULE DEVELOPMENT AND PRODUCTION

A major element of the ICF target fabrication activity is development of new techniques for production of improved targets for future deliveries. Some of these activities are described here.

2.1. POLY(ALPHA-METHYLSTYRENE) (PAMS) SHELL PRODUCTION AND DEVELOPMENT

In the summer of 1995, LLNL scientists transferred to General Atomics their knowledge of the PAMS/GDP process for making ICF targets. General Atomics was to take this technical knowledge, and to bring it to a production task. By the beginning of the 1996 fiscal year (October 1), the individual pieces of the process had been identified and made functional for steady production of shells. By January of 1996, we were delivering target quality OMEGA shells to LLE, and those deliveries continued throughout the year, as the process was improved.

2.1.1. OVERVIEW OF PAMS/GDP PROCESS

The PAMS/GDP process is a sequence of steps, starting from the production of hollow poly(α-methylstyrene) (PAMS) shells, and ending with a shell composed of GDP (glow discharge polymer). This GDP shell is then the innermost material layer of the final ICF target.

Preparation of the PAMS Shells. The shells are produced in a dual orifice droplet generator, modeled after the device used at Osaka University. All solutions are filtered to 0.2 micron to minimize debris. A drop of water (W_1) is placed within a drop of PAMS/fluorobenzene solution (O_1), at the tip of a dual orifice needle. (The W_1 is brought down an inner stainless steel needle, centered within a second glass needle through which the PAMS solution is flowing.) The PAMS solution is 11 wt % in fluorobenzene. Both solutions are fed by syringe pumps. Control of the relative flows of the O_1 and W_1 controls the wall thickness of the final PAMS shell. Fluorobenzene is our solvent of choice, because it is a

single solvent for dissolving PAMS (404 K MW), and has a density (1.024 at 20°C) nearly matching the density of water.

The encapsulated W_1 in O_1 drop is formed at the tip of the needles, and is stripped off by a flow of surrounding poly(vinyl alcohol) solution. (We have settled on a PVA solution of 0.1 wt%, with 25 K MW PVA and 88% hydrolyzed.) The PVA solution and the encapsulated drops are swept down a glass collection tube, placed flush with the needle tips, and brought into a stirred one liter beaker. The size of the encapsulated drops, and thus the size of the final PAMS shells, is predominantly controlled by the PVA flow and the i.d. of the collection tube.

Once the beaker is filled with PVA solution and the encapsulated droplets, the beaker is transferred to a water bath at 60°C, where the solution is stirred for 3–4 hours to extract the fluorobenzene from the PAMS. The water filled shells are then washed with filtered deionized water to remove any residual PVA, and finally transferred into 25% ethanol/water solutions, to osmotically remove the interior W_1.

This ethanol extraction step initially proved to be a roadblock in the PAMS process. In past work with polystyrene, we would move the shells daily from 25% to 50% to 75% to 100% ethanol. A bubble would nucleate within the polystyrene shells, and the shells would float to the surface. The "floaters" would be transferred to a vacuum oven, to remove the rest of the water. Most of the "floaters" would be good shells, not cracked or otherwise flawed. With PAMS however, there would be massive cracking of PAMS shells in the 50% ethanol solution, which never occurred in the polystyrene case. Ultimately, we found that the nucleation of the bubble in the PAMS was crucial to having a good yield of PAMS shells. The osmotic removal of W_1 by the ethanol results in large osmotic pressure differences across the shell wall. This pressure difference can collapse or crack the shell, unless a bubble is nucleated, which relieves the pressure difference. We found that after 1–2 days in 25% ethanol, placing the beaker of shells in a lab ultrasonic bath for 5–60 seconds would nucleate the bubble immediately. Once a bubble was present, the shells could be removed to a vacuum oven for complete water removal.

In the fall of 1995, we were producing PAMS shells in a generic chemistry lab. The PAMS shells seemed to always have surface debris, which we could not eliminate. This debris would be magnified some ten-fold upon GDP coating, so a micron sized speck on the PAMS shell resulted in a substantial dome on the GDP shell. In January and February 1996 the process for making PAMS shells was moved into a small clean room. The shell batches

consistently had better surface cleanliness compared to batches made in the chemistry lab and should improve the quality of the future GDP mandrels. The PAMS process has remained in the clean room.

Diameter Control. The droplet generator readily makes shells near 1000 micron o.d., with a very narrow size distribution. This very narrow size distribution is both a blessing and a curse. The curse is that with the narrow size distribution, it is very easy to "miss" making the required size shell. A person can spend an entire day setting up and making shells only to find at the end of the day that the shells made were 940±10 microns o.d., when 960 microns o.d. was sought. Ideally, we would be able to measure the wet droplet size just after the droplets come off the needle, and correlate that size with the final shell size. In that way we could tune the system while it is running in order to ensure proper shell diameter. However, a detector system which will work satisfactorily to measure the shells in real time has not been identified.

As an alternative, we have tried to mathematically model the system. If we adequately model the forces upon the droplet, we can know the size of the droplet at the moment the net force on the drop knocks it off the needle. We would know what experimental settings to make, in order to obtain the correct final shell 4 hours later.

The sum of the forces on the drop are:

$$F = (\Delta\rho)\ (4/3)\ \pi\, r^3 g + \pi\, R^2 \Delta P - 2\pi R\, \gamma \sin\alpha + 6\pi\, V\, \eta\, r$$

= force of gravity on shell + pressure on needle + surface tension drop/needle + Stokes Law stripping flow

$\Delta\rho$ = difference of drop density and PVA fluid (0.01–0.02 g/cc)

r = radius of drop (o.d. of drop = d = 2r)

g = 980 cm/s^2 = gravitational acceleration

R = radius of needle drop is exiting (D = 2R)

ΔP = pressure to begin to blow drop ($\Delta P = 2\,\gamma/r$)

γ = surface tension of drop (fluorobenzene = 27 dyne/cm)

α = contact angle of drop with needle (set $\sin\alpha = 1$)

V = linear velocity of PVA stripping fluid around drop, within collection tube (collection tube i.d. = D)

η = PVA stripping fluid viscosity (1.04 cp by Mark-Houwink calculation, 0.1 wt% PVA

For the typical settings to make 1000 micron shells the mass term is insignificant compared to the other terms. Collecting terms and units, writing the linear velocity V as a function of PVA flow and collection tube i.d., and correcting the decreased annulus area of the flow as a function of the drop size growing within the collection tube, results in the following equation for the wet shell diameter d at the moment F = 0, for a given PVA flow setting:

$$\text{PVA Flow (cc/min)} = (5\pi\gamma/\eta)(D^2 - d^2)(2R/d)(1 - 2R/d)$$

Thus, the collection tube i.d. (D), the needle diameter (2R), and the PVA flow have a strong impact on the size of the wet shell o.d. (d). The diameter of the dry shell (d*), is approximately $\sqrt{2}\ d^* = d$, when the syringe pump flows are equal.

The use of this equation to estimate settings for the droplet generator entails several approximations and assumptions. First, it assumes the drops break off cleanly at the needle. In reality, the drop deforms in shape and the liquid stretches until broken, so there are rheological issues ignored and the wet droplet is certainly not a sphere. Second, the use of the simplest form of Stokes Law for the PVA stripping ignores the use of Reynolds Numbers (Re), friction factors, and turbulence. Stokes Law is most appropriate for Re < 1, while typical values of Re down the collection tube are 100–1000. The Stokes Law also presumes the stripping fluid flow sees the entire surface of the drop. However, the glass needles block or obscure the PVA fluid flow from seeing the top of the drop. Given these approximations, we would have to run samples and see how well the equation fits the experimental data.

A series of runs were made during the summer, with the participation of Michael Sixtus, a high school teacher who interned with General Atomics. Figure 2-1 shows an example of a fit of this equation to experimental data, where he varied the PVA flow from 300 cc/min to 50 cc/min, and we measured the average dry shell diameter. In this fit, all the known experimental values were used, except the term 2R was treated as a free valued parameter. To let 2R float, is to recognize that the shell does not break off from the needle (of dimension 2R), but rather the droplet liquid itself forms a narrow neck and breaks off. Ultimately, from

the series of runs made, it appears that the PVA flow equation used above can direct us to dialing in a shell diameter, to about 5–10%, but not to an accuracy of 1% or better.

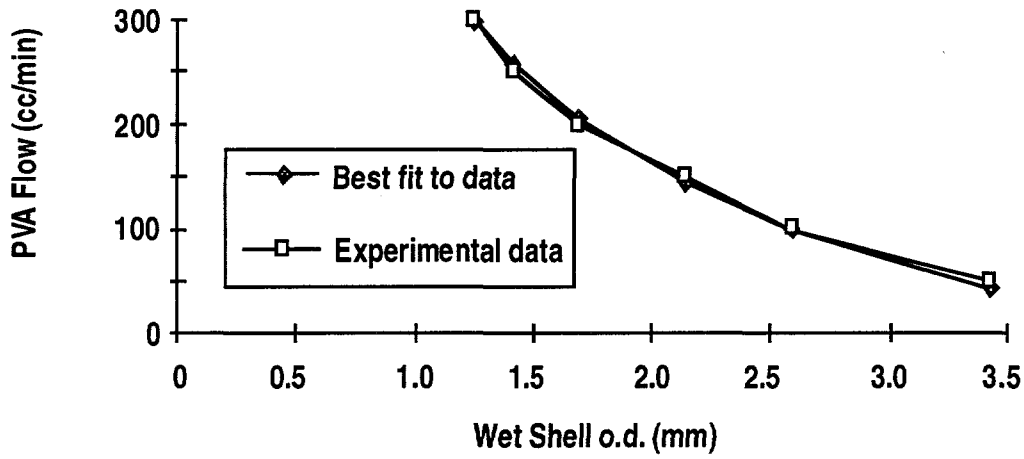

Fig. 2-1. Fit of Experimental Data (Run 960726) to PVA flow equation. The value of 2R was found to be 0.06 mm, which had no relationship to the needle dimensions.

Preparation of the GDP Mandrel. The dry PAMS shells are screened for the proper size and minimal non-sphericity, before being passed to GDP coating. Some 50–1000 shells are placed in a bounce coater, and the GDP is deposited, at a typical rate of 1 micron per hour. Dopant gases can be added, to place dopants into the GDP coating as required (Section 2.3).

After the GDP deposition, the shells (GDP atop PAMS) are placed in a tube furnace in a nitrogen gas flow, and the temperature is slowly raised to 300°C. At 300°C, the PAMS depolymerizes back to α-methylstyrene monomer, and the monomer diffuses through the GDP and is swept away by the inert gas. This pyrolysis step leaves behind a GDP shell. This pyrolysis step can also result in some dimensional changes in the GDP shell (Section 2.3).

2.1.2. PRODUCTION PARAMETERS FOR OMEGA PAMS SHELLS

For the production of OMEGA PAMS shells near 900–1000 microns o.d., with an 18–20 micron PAMS wall thickness, the following operating conditions were typically used. The W_1 and O_1 syringe pump flows were each 50 cc/hr, and the PVA flow was near 300 cc/min. The collection tube had an i.d. of 4 mm. The glass needle had an i.d. of 0.9 mm, and the W_1 metal needle had an o.d. of 0.5 mm. At these settings, we produced shells at

about 40–50 per second, and the entire run to fill six one liter beakers was finished in some 20 minutes. The final dry PAMS shells had an o.d. of typically 960 microns, with a standard deviation of about 10 microns. Individual shells had sphericities of >99.5% with excellent wall uniformity. Turning the PVA flow down towards 50 cc/min resulted in dry shells of o.d. near 2500–2700 microns. The shells had considerably worse sphericity and wall thickness uniformity. While shells with o.d. from 960 to 2700 microns were made with the 4 mm collection tube, changing to a 2.2 mm collection tube permits us to make shells from 300–1100 microns in o.d.

For further information, please contact Dr. B. McQuillan (GA)

2.2. POLYSTYRENE SHELLS BY MICROENCAPSULATION

During FY96, we successfully made the transition from research and development to the production of target-quality polystyrene (PS) mandrels for OMEGA. A number of technical challenges were solved including the control of cracking and dimpling, vacuoles, deposits, and debris. Once a sufficient OMEGA mandrel supply was generated, an additional development effort was undertaken to produce chlorinated mandrels for OMEGA diagnostic experiments. Several chlorinated materials were investigated to produce chlorinated mandrels via direct microencapsulation.

2.2.1. PRODUCTION OF POLYSTYRENE SHELLS FOR OMEGA

During the first six months of FY96, PS shells were produced at an average rate of ~200 target-quality shells per month. A total of 1385 mandrels were put into subsequent target production processing. A comparison of the desired OMEGA specifications and the delivered values are shown in Table 2-1. The diameter, wall thickness, concentricity, and vacuole level specifications were all achieved. The interference images of 9 × 900 μm shells (9 μm walls, 900 μm diameter) shown in Fig. 2-2 are typical of the quality of the deliveries.

TABLE 2-1
DESIRED OMEGA SHELL SPECIFICATIONS AND DELIVERED VALUES.

Specification	Desired Value	Delivered Value
Shell diameter	850–1000 μm	911 ± 35 μm
Wall thickness	5–15 μm	8.6 ± 0.7 μm
Concentricity	P1 < 1 μm; NC < 10%	NC < 5%
Vacuoles > 5 μm	0	0
3–5 μm	30	0
1–3 μm	50	≈ 0
<1 μm	200	Not determined

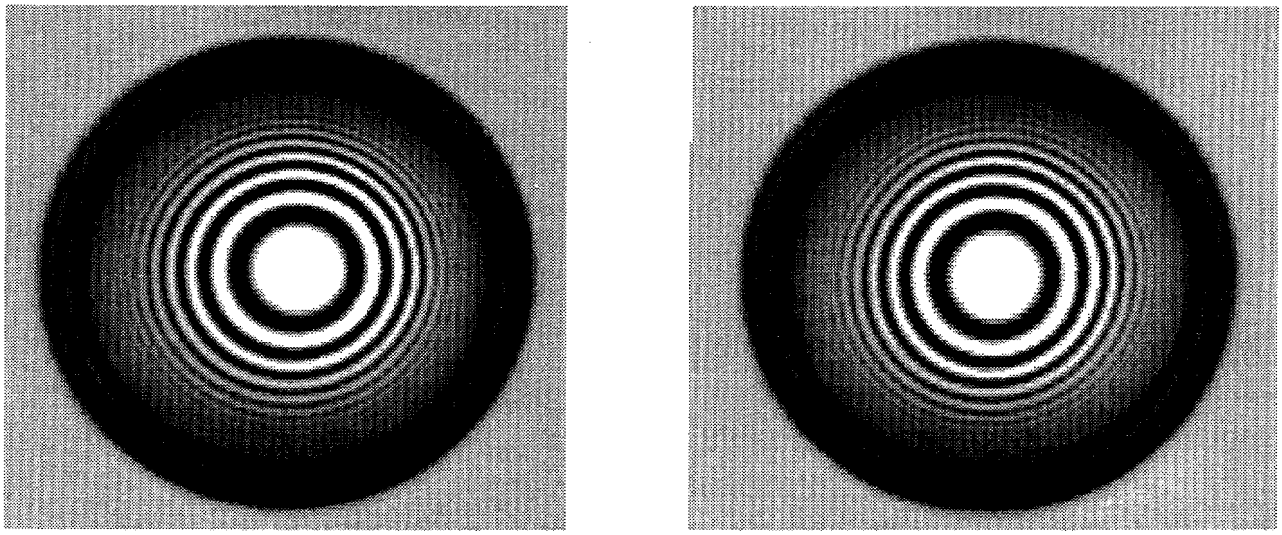

Fig. 2-2. Interference patterns from target-quality 9 × 900 μm polystyrene (90 K MW, 1.04 PD) shells produced via controlled-mass microencapsulation.

2.2.2. DEVELOPMENT OF CHLORINE-DOPED SHELLS FOR OMEGA

Experiments planned for OMEGA require capsules with chlorinated layers. Although the PAMS/GDP technique is well-suited for producing exotic multi-layered doped targets, chlorine doping of GDP was problematic. Apparently, a Cl depletion layer or concentration gradient was being formed during the PAMS pyrolysis processing. Direct controlled-mass microencapsulation was proposed as a possible alternate method to produce chlorinated mandrels.

The following development strategy was adopted to produce chlorinated mandrels. Starting from the optimized processing conditions of OMEGA PS shell production, we strove to: (1) achieve encapsulation with a chlorinated material, (2) improve survivability by increasing molecular weight (MW) and decreasing polydispersity (PD), (3) optimize processing conditions by employing sonication. Several candidate chlorinated materials were obtained commercially or by custom synthesis. Table 2-2 shows a database of these materials including the molecular weights and polydispersities.

TABLE 2-2
CHLORINATED POLYMERS OBTAINED AND CHARACTERIZED FOR DEVELOPMENT

Polym.	Structure	Manfr.	w (k)	PD*	Encaps.†
PS	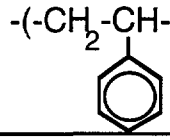	Press. Chem.	90	1.04	√
P4ClS	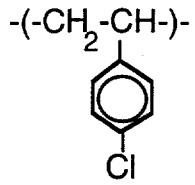	GA	28	2.00	√
"		Polysci.	387	3.19	
"		Polysci.	346	9.52	√
"		Dajac	544	10.85	
"		SPP	491	1.95	
PClMS	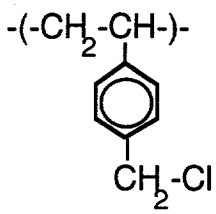	SPP	55	2.72	
"		SPP	503	3.71	√

*PD = polydispersity (M_w/M_n)
†Indicates which polymers were successfully encapsulated.
GA = General Atomics, custom synthesized by Barry McQuillan
SPP = Scientific Polymer Products

Note: The last column indicates which materials were successfully encapsulated and partially process-optimized.

Attempts to produce 9 × 900 μm OMEGA-sized shells with relatively low MW poly(4-chlorostyrene), P_4ClS, resulted in severe shell cracking, even prior to any ethanol extraction processing, as shown in Fig. 2-3. Although cracking was significantly reduced by increasing wall thickness to 16 μm, it was clear that achieving 5 × 900 μm chlorinated mandrels to serve as the inner-most layer of multi-layered diagnostic capsules would be very difficult.

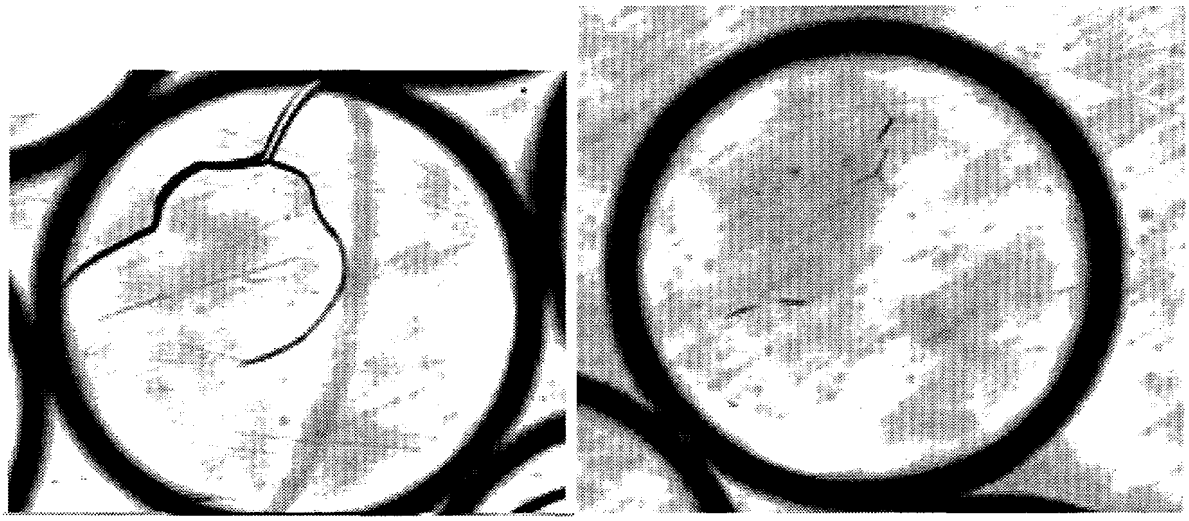

Fig. 2-3. Photographs of solidified ~900 μm diameter poly(4-chlorostyrene) (28 K MW, 2.0 PD) shells with 8 μm (left) and 16 μm (right) wall thicknesses.

We sought to improve shell survivability by using a higher MW polymer, P_4ClS (346 K). Unfortunately, this material also had a higher PD (9.52). It was hypothesized that greater MW would improve strength, while greater PD would be detrimental. As shown in Fig. 2-4, the higher MW material exhibited improved survivability (despite the increased PD), as evidenced by the better cumulative yield with each processing step.

Having established that higher MW improves shell strength, we optimized the processing conditions to reduce wall thickness and improve yield. This was accomplished primarily by employing sonication steps intermittently during ethanol/water extraction steps. Sonication improves yield by initiating bubbles in the osmotically-stressed core. The formation of a bubble maintains a water vapor pressure in the core as water is drawn out into the ethanol-rich exterior, which mitigates the osmotic imploding forces that can cause dimpling and cracking. As shown in Fig. 2-5, bubbles were initiated in about 40% of the P_4ClS shells exposed to ethanol. However, too much sonication can crack or shatter shells. Yield was optimized by employing several 5-second sonication exposures, as shown in Fig. 2-6. By

optimizing the use of sonication, the wall thickness of the P_4ClS (346 K MW, 9.52 PD) was reduced from 16 to 14 μm, while increasing over-all yield from 8% to 40%.

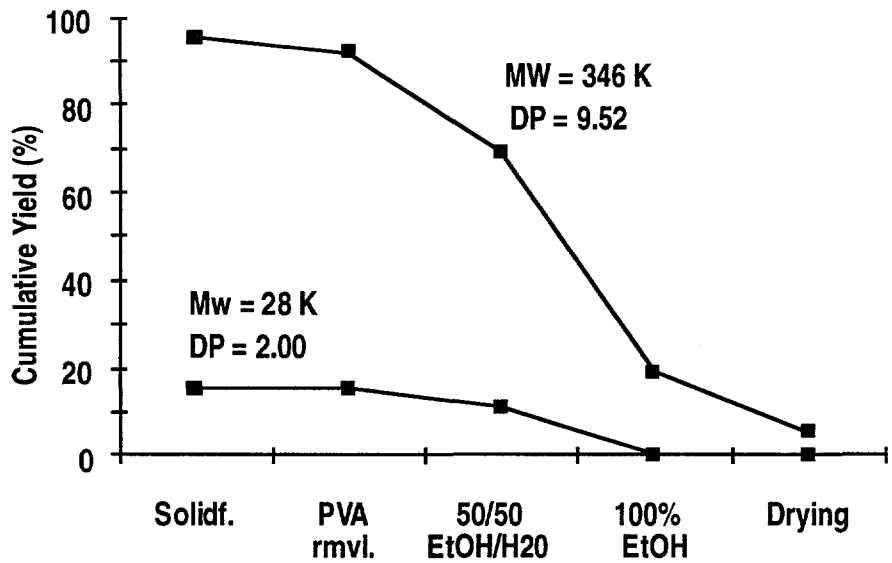

Fig. 2-4. Cumulative yields throughout the microencapsulation processing of 16 x 900 μm shells produced with poly(4-chlorostyrene) with 28 K MW/2.0 PD (lower curve) and 346 MW/9.52 DP (upper curve).

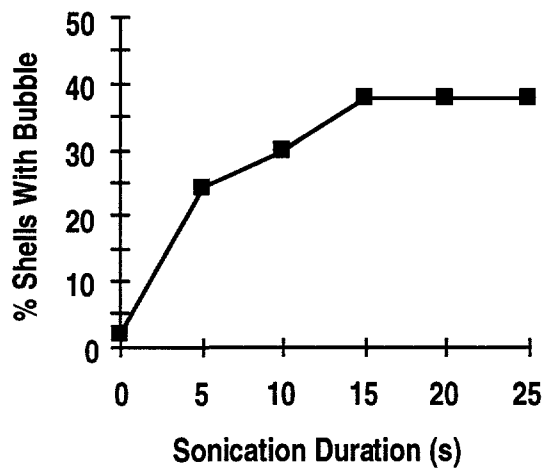

Fig. 2-5. Bubble formation during sonication of 14 × 980 μm poly(4-chlorostyrene) shells. Shells were soaked in 50/50 ethanol/water for 24 hours prior to sonication

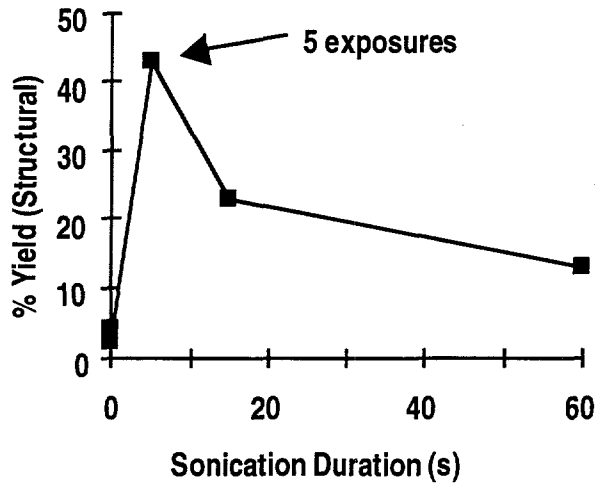

Fig. 2-6. Effect of sonication on final structural yield of 14 × 980 μm poly(4-chlorostyrene) shells. Shells were solidified, rinsed of PVA, soaked in 50/50 ethanol/water for 24 hours, sonicated for the indicated durations, soaked in 100% ethanol for 24 hours, then oven dried at 60°C for 48 hours.

We repeated the development strategy with a poly(chloromethylstyrene) (PClMS) of 503 K MW and 3.71 PD. Although it was hoped that the higher MW and lower PD would provide improvements over the P_4ClS (346 K MW, 9.52 PD), the PClMS was inferior to P_4ClS, as shown in Fig. 2-7. The cracking, dimpling, and cumulative yields of PClMS were consistently worse than P_4ClS. It is believed that the methyl group of PClMS reduces packing efficiency and lowers cohesive energy density, causing increased brittleness and lower yields.

In conclusion, chlorinated mandrels were successfully produced via direct controlled-mass microencapsulation. Sonication was employed to reduce cracking and dimpling damage during extraction, resulting in acceptable over-all yields. The best-effort shells were produced with P_4ClS (346 K MW, 9.52 PD) and had dimensions of 14 × 980 μm and target-quality concentricity and vacuole levels. Further reductions in wall thickness may be possible with additional optimization of extraction duration and sonication timing and by employing higher MW chlorinated materials with higher packing efficiency and cohesive energy density.

This work was done by Dr. T. Boone at Soane Technologies. For additional information contact W. Miller (GA).

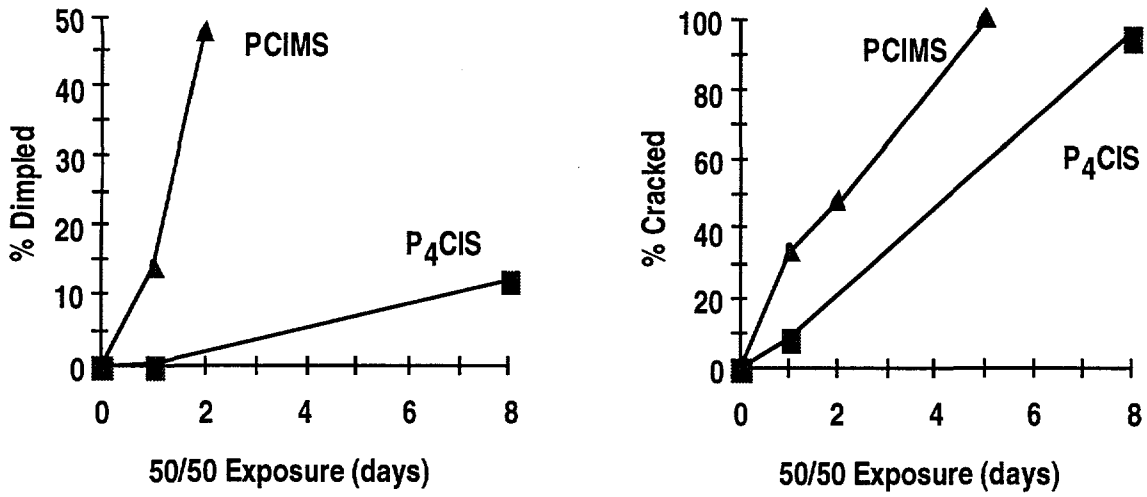

Fig. 2-7. Comparison of the survivability of 14 ×980 μm shells of P4ClS (346 K MW, 9.52 PD) and PCIMS (503 K MW, 3.71 PD). Left: dimpling as a function of 50/50 ethanol/water exposure duration. Right: cracking as a function of 50/50 ethanol/water exposure duration.

2.3. COATINGS FABRICATION — DOPED GDP COATINGS

Cl-GDP Coatings. Development of chlorine-doped GDP (Cl-GDP) for LLE, which was started last year was continued this year. There is a discrepancy in the bulk Cl concentration of the films as measured by Rutherford Backscattering (RBS) versus determination by x-ray fluorescence (XRF) or by the combustion technique. However, due to the thermal instability of Cl doped plasma polymer which severely reduces the usefulness of this polymer in the ICF program, resolution of this discrepancy has not been a priority issue. Experiments to resolve the differences between the techniques are being conducted as time allows.

Cl-GDP films made using a chlorinated hydrocarbon precursor alone yielded stress free, amber colored high quality films. Addition of hydrogen and/or trans-2-butene (T2B) resulted in dark or black coatings with reduced chlorine content and increased stress (Fig. 2-8). The chlorine concentration was controlled by the choice of the dopant. Table 2-3 lists the chlorine content of various GDP films in atomic percent, as measured by XRF, obtained using several different chlorine containing dopants.

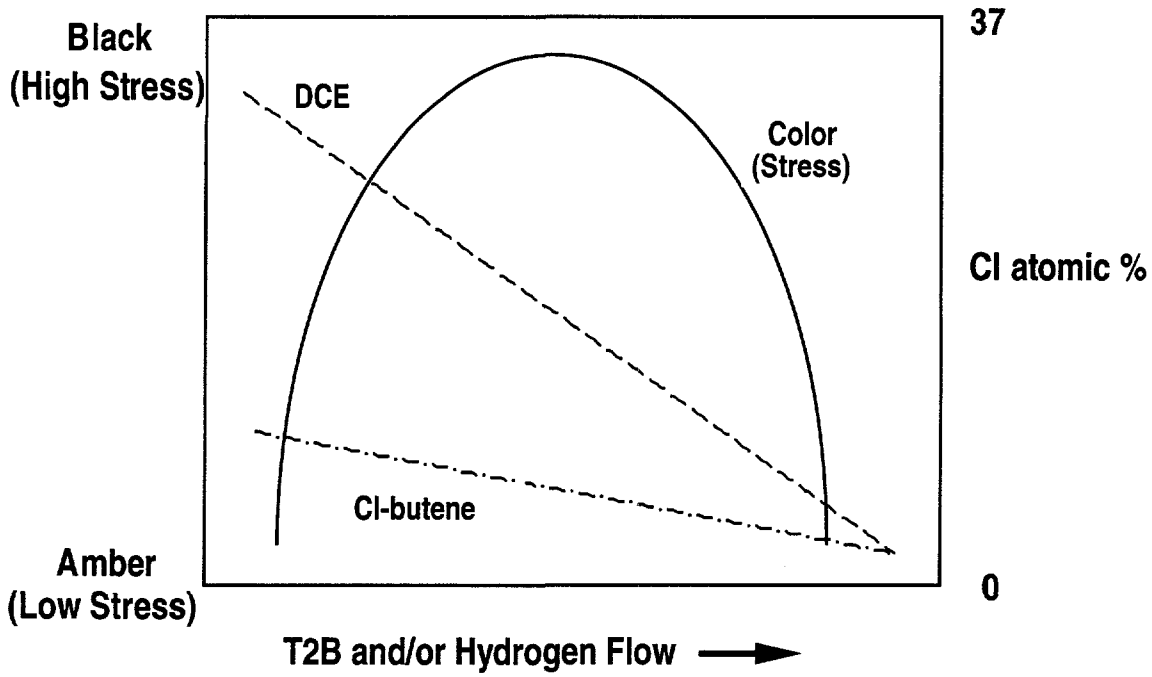

Fig. 2-8. Qualitative plot of the effect of mixing chlorinated hydrocarbons with T2B and hydrogen. The dashed lines represent the chlorine content for two different dopants. Coatings made with the chlorinated hydrocarbon alone have the highest Cl content and are at the same time light-colored and stress-free. As more and more T2B and/or hydrogen are added to the coating process, films become darker and more stressed and contain less Cl. Films made with little relative chlorinated hydrocarbon flow are also stress-free and light-colored but contain little chlorine (undoped GDP).

TABLE 2-3
CHLORINATED HYDROCARBONS (Cl-HC) USED IN THE EXPERIMENTS AND THE MAXIMUM CHLORINE CONCENTRATION OBTAINED WITH EACH DOPANT

Cl — HC	Max. Cl Atomic %
Chlorobutene	6
Chloromethane	17
Dichloromethane	22
Dichloroethene	35
Chlorobenzene	6

Low resolution (≈5 μm) EDAX measurements on the cross-section of these films revealed no major inhomogeneity in the chlorine concentration in the bulk of the sample. However, high resolution (≈10 nm) RBS measurements indicated a large gradient in the chlorine concentration of the films. In particular, there appeared to be a depletion of chlorine

near the surface, which generally disappeared ≈2 μm into the bulk. XRF measurements on thin (>2 μm) samples also indicated a lower bulk chlorine concentration than those of thicker (>2 μm) films (Fig. 2-9). Since GDP films are known to pick up oxygen (up to 8 at. %) during exposure to air under ambient conditions, the observed chlorine depletion near the surface of the Cl-GDP films may be the result of replacement of labile chlorine by oxygen or hydroxide.

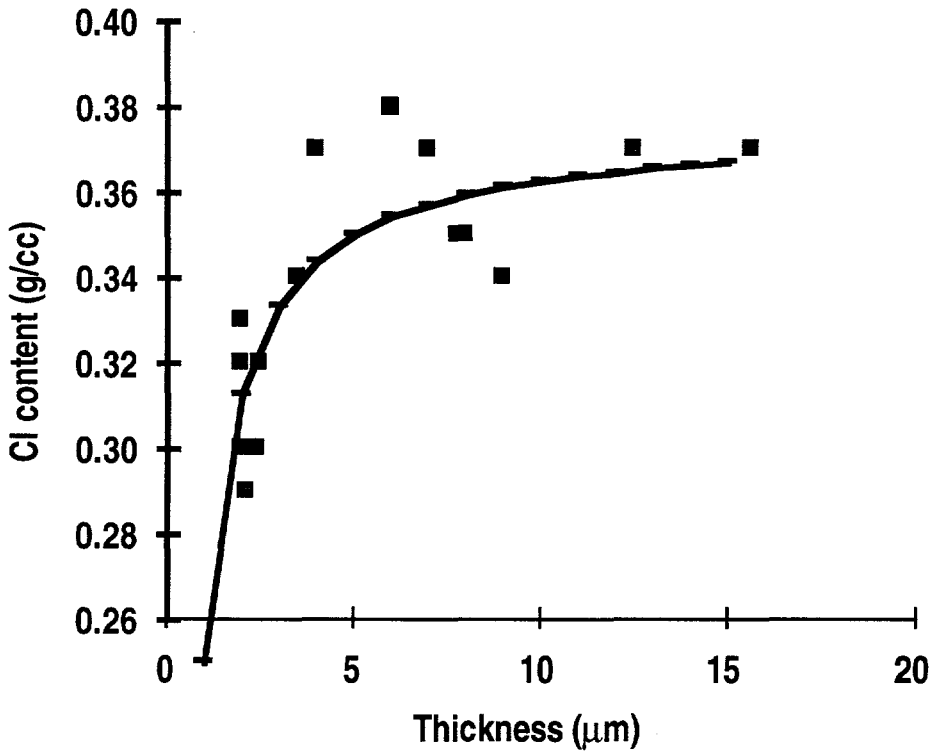

Fig. 2-9. Chlorine concentration as a function of coating thickness for chlorobutene films. Coatings thinner than ~2 μm have lower chlorine content possibly because of liberation of HCl as the film oxidizes.

RBS measurements also indicated bleeding of chlorine from the doped layer into an adjacent undoped layer in a multi-layer film. As chlorine is thermally unstable in most polymers, and even more unstable in these plasma polymers, it is conceivable the migration of the chlorine may be substantially caused by the RBS measurement beam itself. Otherwise, it might have taken place because of plasma heating of the Cl-GDP layer during the deposition of the undoped GDP overcoating or a combination thereof.

The surface of Cl-GDP films were usually covered with many domes. There were also numerous spherical beads on the surface. These beads were analyzed by EDAX and

appeared to be plasma polymer. The tubes were very black after short coating runs. Normal GDP tubes are usually light brown. There appeared to be an excessive amount of coating taking place in the tube compared to the substrates. Lack of hydrogen in the Cl-GDP process leads to a very organically rich plasma. This leads to the possibility of gas phase polymerization. Any small debris would also act as a nucleation site and be quickly coated. To avoid excessive coating in the tube, the plasma in the coating tube was lowered towards the substrates by modifying the helical resonator. The resonator coil was effectively shortened by shorting out all the turns except for the bottom seven. The RF tap down was also moved from the seventh turn to the second turn of the coil. With these changes the resulting coating no longer contained beads, and the number of domes on the surface decreased. The surfaces, however, continued to have more domes than undoped GDP films. Because of the lower gas flows in this system, the shells needed to be bounced more vigorously than in the undoped GDP systems. We have observed that vigorous bouncing of PAMS shells can result in the appearance of domes and beads even in the undoped GDP film deposition process. The residual domes might have come about by this mechanism.

Si-GDP Coatings. Tetramethylsilane (TMS) was added to the standard GDP process as the dopant to obtain silicon-doped GDP films. In the rather well developed germanium-doped GDP process, tetramethylgermane is added as a dopant to trans-2-butene (T2B) and hydrogen. To obtain silicon-doped GDP, tetramethylsilane was added to the GDP process in an analogous manner. The current coating parameters yield about 5.5 atomic % Si as determined by combustion analysis. RBS measurements on these samples revealed the presence of 8 at. % O in addition to the 5.5 at. % Si. Si-doped GDP films are lighter in color than undoped GDP films. These films contain little residual stress and the surface finish is similar to Ge-GDP (background surface finish is ~4 nm).

Deuterated GDP. In order to coat shells with deuterated GDP, a bouncer system was added to a GDP coater used for coating flat substrates with deuterated GDP. Previously deuterated T2B (D-T2B) along with deuterium (D_2) was used in this system. We used CD_4 along with D_2 for coating shells. The main advantage of CD_4 over D-T2B is that it is less expensive, ≈$50 per liter compared to $1000 per liter for D-T2B. With CD_4, the coating parameters had to be changed, since using the parameters used for D-T2B led to etching rather than coating. D_2 flow was reduced from over 6 sccm to 2 sccm. The RF power was reduced from 10 watts to about 3 watts. With these change, the resulting deuterated coatings were similar to undoped GDP films although they were somewhat lighter in color. The index of refraction for these films was almost identical (1.585) to undoped GDP films. Samples of

D-GDP mandrels prepared by the PAMS technique were analyzed using Nuclear Resonance Analysis (NRA). This analysis indicated 100% deuteration of the GDP was maintained during the pyrolysis of the PAMS mandrel.

Ti-GDP Coatings. GDP coatings doped with transition metals are needed as a diagnostic tool for experiments on the OMEGA laser. The preferred transition metal is titanium (Ti). The desired doping level is ~1 at. %. A hydrocarbon containing Ti or other transition metals is needed for this process. Many of the possible organo-metallic compounds are unstable in air. Additionally, there are very few that do not contain oxygen or a halide. The guidelines for the composition of the films as described by LLE experimentalist, however, allow the presence of a few atoms of oxygen per atom of transition metal. Also, films containing both Ti and Chlorine are also permissible. Table 2-4 lists some possible dopants. The dopant for the GDP process must be volatile enough to be used in our system. Ferrocene appears to ideal. It does not contain oxygen or a halide. It is volatile and is air stable. However, since Ti doping is preferred over doping with other transition metals, $TiCl_4$ was chosen as the initial dopant.

TABLE 2-4
POSSIBLE PRECURSORS FOR TRANSITION METAL DOPED GDP

Dopant	CH only	Air Stable	Hazard	Volatility(25°C)
$Fe(CO)_5$	No	No	Low	28 Torr
$CpCo(CO)_2$	No	No	Low	2 Torr
$Ni(CO)_4$	No	No	High	391 Torr
Ferrocene	Yes	Yes	Low	2.5 Torr
$TiCl_4$	No	No	Medium	10 Torr

Possible dopant precursors picked out from transition-metal organometallic compounds. The dopant needs to have high vapor pressure and low toxicity to be used in the coating system. A few atoms of oxygen or chlorine per atom of metal are allowed. in the final GDP.

For the coating process, normal GDP parameters were used and $TiCl_4$ was added at <0.1 sccm. The first observation is that the coatings with high Ti content (>0.7 at. %) start off grayish and rapidly change to an off white color within one minute after exposure to air. These films crack and lose their integrity. This is presumably because of rapid oxidation of

the Ti in the films. Coatings with lower Ti contents retain their integrity and do not change color noticeably. The films deposited in the coating tubes always change color, but usually over a number of hours. This seems to indicate that high amounts of Ti are deposited in the coating tube itself.

GDP-like films containing ~0.5 at. % Ti have been made. OMEGA-size shells have been coated with such films and delivered to LLE. The major problem at the moment is the apparent irreproducibility of the Ti content of the films from run to run using the same coating parameters. Initially, the Ti at. % (measured by XRF) of the films changed between 0.1 and 1.3 at. % for the same coating parameters. Changing a few suspect components has improved the reproducibility and the Ti content now varies between 0.35 and 0.5 at. %. More work is needed in this area to obtain better reproducibility.

GDP/PAMS Production of Target Quality Shells. In FY96, almost all the plastic shells shipped to UR for various orders were pure GDP shells. UR required plastic shells with diameters in the range of 850–950 μm and thicknesses in the range of 1–30 μm for experiments on the OMEGA laser. Previously, polystyrene mandrels made by the shake and toss technique or by droplet generator were used. However, polystyrene mandrels with walls thinner than 7 μm in this diameter range were never made. In addition, the yield of high quality PS shells with walls between 7 and 10 μm was very low. We used the depolymerizable mandrel technique to make GDP shells in the desired size range. The starting mandrels are PAMS shells made in a droplet generator. These shells are then coated with undoped or doped GDP in standard GDP coaters. The specifications for a given order dictate the amount and types of coatings deposited on the PAMS. PAMS become volatile and depolymerizes at around 300°C. Therefore, after the GDP coating, the inner PAMS mandrels are pyrolyzed away leaving pure GDP mandrels. Moreover, because large quantities of PAMS shells can be made rapidly in the droplet generator, the yield is much higher in this technique.

This technique allows a thin doped layer to be the inner most layer of a shell. In addition, because GDP is inherently stronger than polystyrene, high quality large thin walled shells can be made. Using this technique, shells with doped innermost layers (e.g., Ti- and deuterium-doped) as thin as 1 μm have been made. High quality large diameter shells (~900 μm diameter) with walls as thin as 0.8 μm have also been made.

The pyrolysis procedure used is similar to the original one developed by S. Letts, et al., at LLNL. The shells are pyrolyzed in a tube furnace equipped with a temperature controller. The samples are placed near the center of the tube. A thermocouple reads the furnace tem-

perature directly above the samples. Initially, before the furnace is turned on, the tube is evacuated and then it is filled to atmospheric pressure with nitrogen. Subsequently, the furnace is turned on and the pyrolysis run starts. During pyrolysis, nitrogen continues to flow in the tube and exits through a bubbler. The flowing gas ensures temperature uniformity in the area in which the samples are placed. The furnace temperature profile is as follows:

Ramp up from room temperature to 200°C at 10 deg/min

Ramp up from 200°C to 300°C at 0.2 deg/min

Hold at 300°C for T minutes.

Shut off oven and cool down to room temperature in ~4 hours

The main variable in the procedure is the final hold time T. The minimum duration necessary for T was found to be about one hour. This was confirmed to be independent of GDP wall thicknesses up to about 20 μm. The limiting rate in the procedure appears to be the PAMS depolymerization rate. Permeation through GDP takes place fast enough that there is no noticeable dependence on GDP thickness. Much longer hold times, typically 16 hours, were used in most pyrolysis runs.

GDP mandrels shrink, both in diameter and wall thickness, during pyrolysis. The amount of shrinkage depends on the type of dopant present in the film and the length of the final temperature hold time T. Table 2-5 shows the shrinkage values for different types of GDP films for 16 hours of hold time. Notice that Si-doped GDP, in contrast to the other types, does not shrink. For multi-layer shells containing a Si-doped layer, the lack of shrinkage in the Si-doped layer, sometimes led to low relief wrinkling of the Si-doped layer.

TABLE 2-5
SHRINKAGE OF GDP FILMS AFTER PYROLYSIS AS A FUNCTION OF DOPING

GDP Shell Type	ID Shrinkage (%)	Wall Shrinkage (%)
Undoped	6	10
Ge	2	4
Si	0	0
Cl	6	10
CD	6	10

The pyrolysis process can also affect the dopant concentration of films doped with elements, such as chlorine and bromine, that are thermally unstable in a polymer matrix. Chlorine doped GDP films lose about 80% of their chlorine content during pyrolysis. Films doped with silicon, germanium and titanium, however, showed no significant change in their doping levels after pyrolysis. Also, Nuclear Resonance Analysis (NRA) indicated there was no exchange of deuterium for hydrogen when deuterated GDP coated PAMS were pyrolyzed.

For further information, please contact Dr. A. Nikroo (GA)

2.4. CHARACTERIZATION

Tighter tolerances and increased target delivery rates necessitate the need for new or improved characterization techniques. Some of these development activities are described here.

2.4.1. PRECISE OUTER-DIAMETER MEASUREMENTS

Increased accuracy requirements for the determination of diameters of capsules for the ICF program have led to the development of an improved diameter measurement technique. This enhanced measurement technique utilizes tungsten carbide or sapphire balls with National Institute of Standards and Technology (NIST) traceable diameters and sphericity.

Previous o.d. measurements relied on square, planar NIST traceable standards and a line measurement tool in the National Institute of Health (NIH) *Image* program which limited accuracy and precision to about 0.5%.

Our new method of measurement, which relies on spherical standards and measurement of the capsule perimeter under precise lighting conditions, has a factor of five better measurement precision. The calibration procedure begins with the setup of the microscope. The microscope lighting is centered and apertures and camera adjusted to give maximum lighting uniformity. A NIST traceable ball of the appropriate size is then used to calibrate the the built-in "wand" feature of the NIH *Image* program for both the pixels per micron and pixel aspect ratio. After calibration, the lighting conditions are strictly maintained so that measurements of the highest precision can be obtained on the samples.

Based on a six month study of the measurement method, the accuracy and precision of this improved method is ±0.1%, or ~1 μm, for a 1 mm diameter capsule. Figure 2-10 graphically depicts the measurement precision of data taken over a six month time span as determined using a Jenavert microscope and two rigidly mounted glass shells.

During the trials to determine our measurement precision as a function of time, we discovered that some types of polymer capsules can change dimensions over time. Two capsules from LLE order P-96 were included in the study. These shells were maintained under ambient laboratory conditions. The diameters of these two capsules, as depicted in Fig. 2-11, are increasing at the rate of about one micron per month. Si-doped GDP mandrels and undoped GDP on polystyrene or PAMS mandrels included in this investigation exhibited no measurable change in o.d. over the six month period.

For further information, please contact Dr. M. Hoppe (GA)

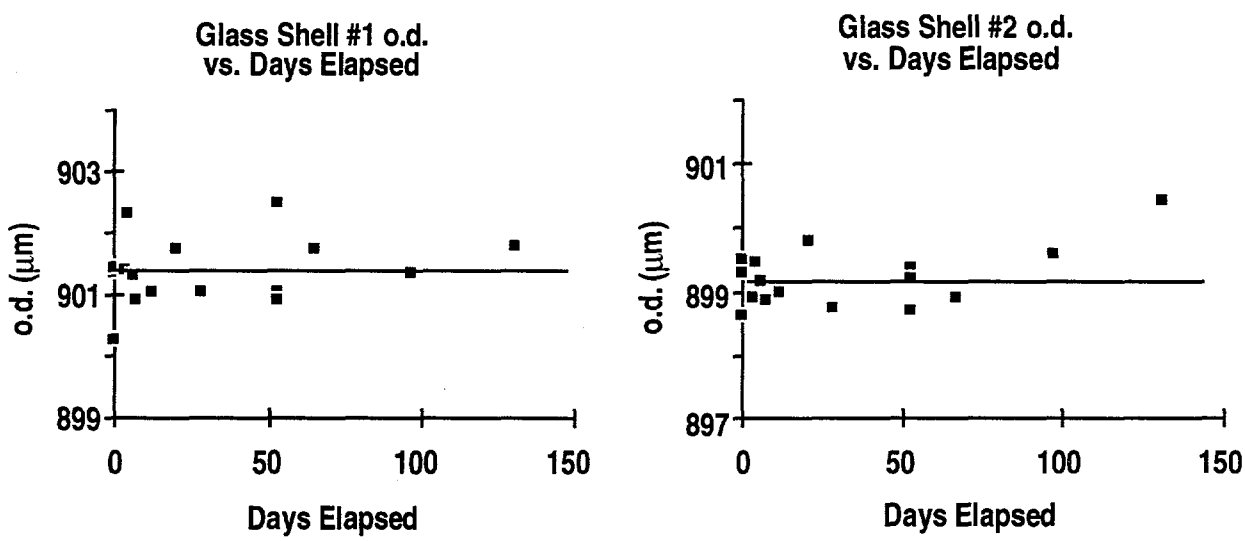

Fig. 2-10. The measurements taken over a period of time, on rigidly mounted glass shells, demonstrate the precision of this method is very good (<1 μm standard deviation).

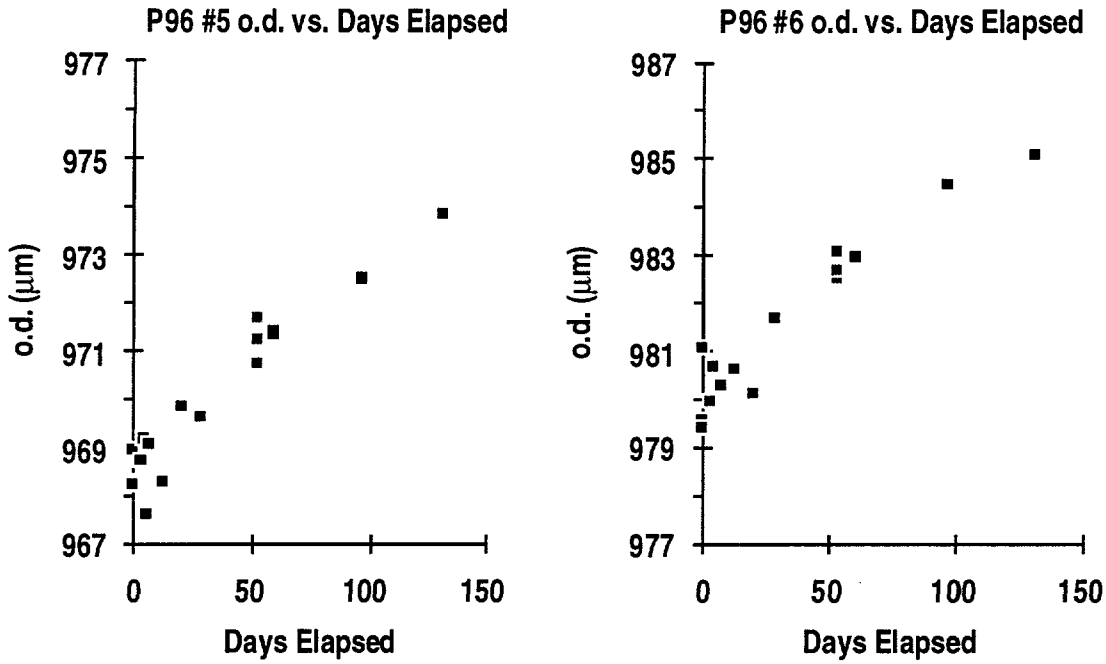

Fig. 2-11. Unnoticed previously, measurements of composite capsule over time show that dimensions may change with age.

2.4.2. DETERMINATION OF WALL THICKNESS BY MASS

The average wall thickness of deliverable shells is one of the critical parameters determined for deliverable capsules. It is also one of the hardest to determine properly. We have used a number of techniques in the past to measure average wall thickness including: direct optical microscopy, optical interference microscopy, and x-radiography. This year we added a weighing technique to determine wall thickness.

The previously used techniques had two failings: they were not very accurate and they did not determine the parameter in which the customer was truly interested, mass per unit area. The uncertainty came from a variety of sources. Optical interference measurements depend on knowing the effective index of refraction of the shell wall. Direct measurement of wall thickness (discussed in the next section) can avoid that, as can x-radiography, but neither of them average the thickness over the whole shell without time-consuming multiple measurements. In addition, one of the critical parameter for these capsules, the mass per unit area, is derived using an assumed wall density of unknown certainty.

Using a shell's mass, along with its diameter, to characterize the wall thickness properly averages over the whole shell surface. Also, in the determination of mass per unit area, the

uncertainty due to the assumed wall density is avoided. This method is also simple, fast, and generally more accurate than previously used techniques. Our ATI-Cahn model C-35 microbalance has a precision of 0.1 μg, and an accuracy of ±0.2 μg (~0.2% of a typical Omega sized capsule's mass). We can measure diameters to ±1 μm (~0.1% of a typical diameter), so the calculated mass per unit area is uncertain to <1%. Mass measurements take only a few minutes per shell.

For further information, please contact Dr. R. Stephens (GA)

2.4.3. TWENTY-SIX POINT MEASUREMENT OF CAPSULES

In response to concerns that low mode number wall thickness fluctuations might limit ICF capsule performance, we have developed a technique for measuring wall thickness at multiple, evenly spaced points on capsule surface's by making a simple modification to our interferometric Nikon microscope. We have used this new technique to characterize composite Nova capsules.

With this technique, we measure a capsule's wall thickness at 26 points around its surface, at nearly uniform 45 degree spacing, in the pattern shown in Fig. 2-12. It takes about one hour to do a single capsule. The data collected should be sufficient to model the wall thickness fluctuations as the sums of spherical harmonics, Y_n^m, up to n = 4.

To measure a capsule's wall thickness at any given point, we use a Nikon reflectance interferometer configured with a piezo-electric stage that can measure relative stage positioning to ±0.1 μm. The piezo stage is used to find the change in the optical path length (OPL) between the inner and outer wall surfaces at the point where the capsule touches the sample mirror (Fig. 2-13).

The wall thickness at that point is then deduced from the relationship:

Wall Thickness = Δ Stage Height/n_{wall} where n_{wall} is the index of refraction of the capsule wall

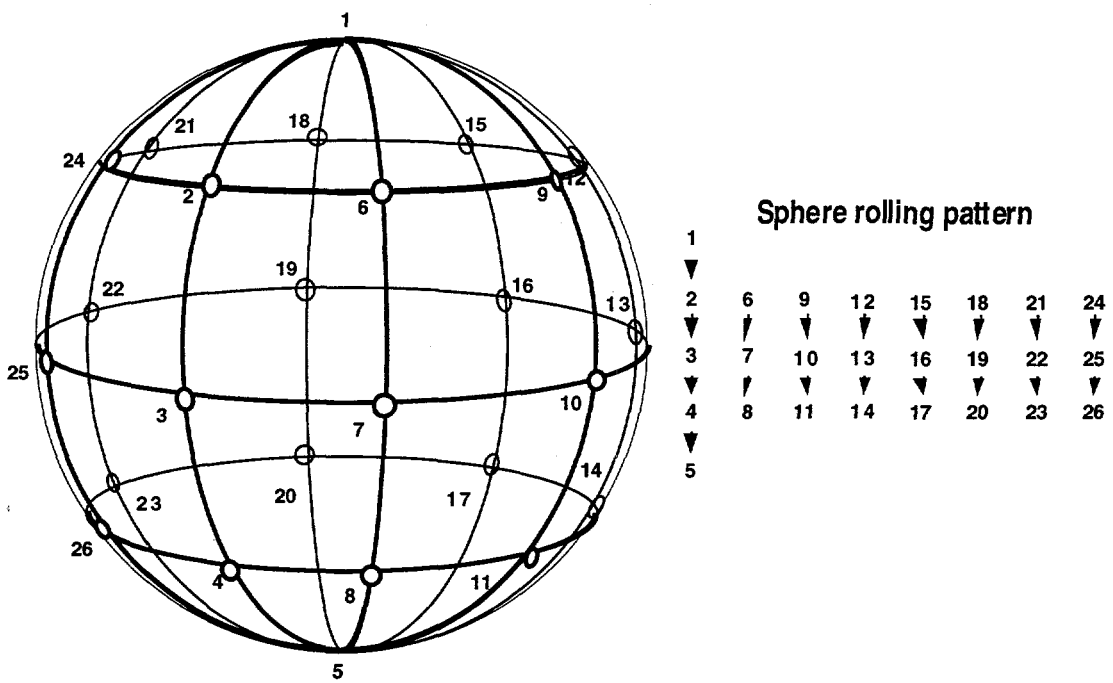

Fig. 2-12. The roll pattern used in our 26 point wall measurement experiments is illustrated. The numbers on the sphere show the sequence in which the data is taken. Starting at the north pole, one measures in 45 degree steps down to the south pole, returns to the equator, and repeats a pattern of rolling the capsule 45 degree along its equator, going to 45 degree north, to 45 degree south, and back to the equator, and repeating until we have gone all the way around.

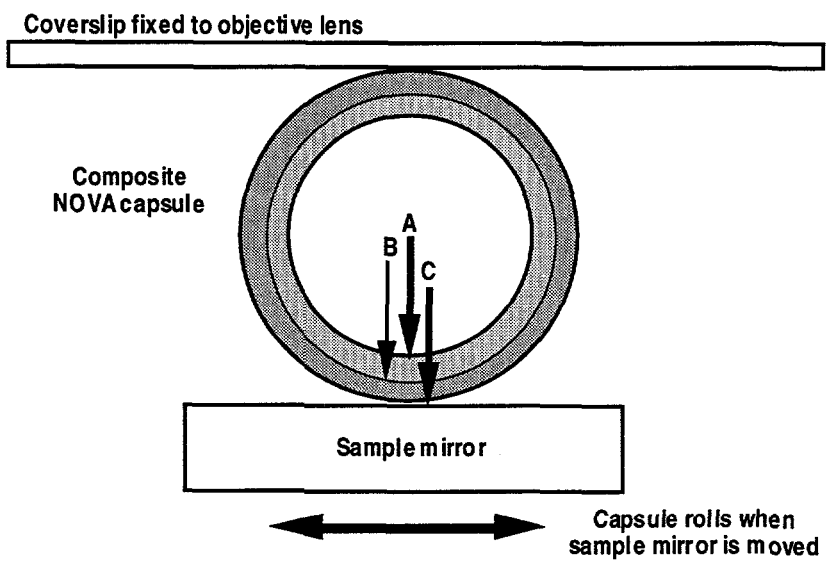

Fig. 2-13. The piezo-electric stage is used to raise the sample mirror to the height at which the OPL to the microscope's reference mirror matches the OPL to the inner wall surface, point A. Likewise, the stage height is found for the OPL match to outer wall surface, point C, or for an interface between coating layers, point B.

To measure the 26 evenly spaced points on the capsule surface, we use the microscope stage positioner controls to roll the capsule to each desired orientation. We accomplish this by hanging a coverslip below the microscope's objective lens such that the capsule is gently sandwiched between the coverslip and the sample mirror (Fig. 2-14). (A second coverslip is placed in the reference arm of the interferometer so that the OPL to the reference mirror remains the same as the OPL to the sample mirror.) When we operate the microscope stage controls, the piezo-electric stage, and sample mirror upon it, move in the x-y plane while the coverslip remains fixed in place. Consequently, the capsule acts as a ball bearing and rolls between the two surfaces. Because the stage controls have x and y micrometer digital readouts, we are able, with knowledge of the capsule's diameter, to roll the capsule precisely to any desired orientation.

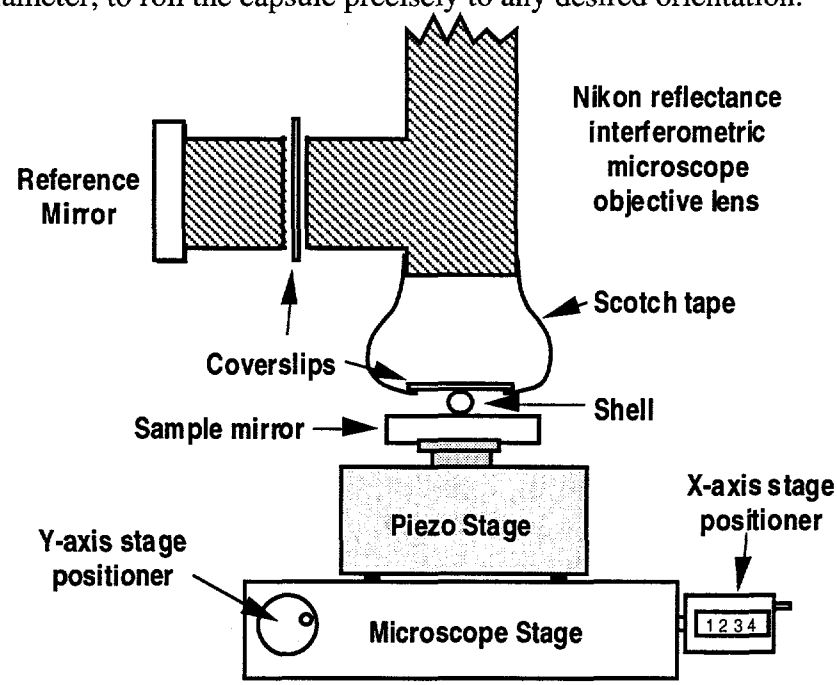

Fig. 2-14. Operating the microscope x- and y-axis stage positioner controls allows us to roll the capsule to any desired orientation.

To evaluate the measurement variability of the 26 point technique, we measured several capsules. The agreement with previous wall thickness measurement techniques is good. The uncertainty of our new measurements is ~1% of the wall thickness.

There is both angular and thickness uncertainty in our measurements. We checked the angular uncertainty by going through the whole procedure with a marked ball such that it should have ended back at the starting point. In several trials, the ending point was never more than ~15 degrees from the starting point, much less than the 45 degree step

size. We checked the measurement uncertainty in the thickness both by multiple measurements of a capsule and measurements by several operators. For this procedure, the capsule was kept in its mount the whole time so that each measurement would be at approximately the same point on the capsule. The standard deviation of the differences in the individual measurements (repeated by the same operator and by different operators was ~0.14 μm for ~10 μm wall capsules. Thicker capsules (~50 μm walls) were a little harder to measure because the fringes were more numerous and less distinct due to dispersion. The standard deviation between the two measurements on the thicker capsule was 0.34 μm (<1% of wall thickness).

For further information, please contact D. Steinman (GA)

2.4.4. IMPROVED X-RADIOGRAPHY

Prior to FY96, our x-radiographic analysis computer program could deliver only average layer thicknesses for a single shell cross-section [Ref. 2-1]. In FY96 we improved the analysis program allowing it to determine layer interface positions at individual radii as a function of angle. This enables us to better examine wall uniformity and shell concentricity using x-radiography.

The Old Method. The pixel values of a digitized shell image correspond directly to the amount of x-rays absorbed by each line through the shell. Using the old x-radiography analysis method, we would calculate 3000 radial lines evenly spaced around a shell image, using the two dimensional Taylor series expansion

$$\begin{aligned} f(x,y) = {} & f(x_0,y_0) + \frac{df}{dx}(x-x_0) + \frac{df}{dy}(y-y_0) \\ & + \frac{\frac{d^2f}{dx^2}(x-x_0)^2 + 2\frac{d^2f}{dxy}(x-x_0)(y-y_0) + \frac{d^2f}{dy^2}(y-y_0)^2}{2} \\ & + \frac{\frac{d^3f}{dx^3}(x-x_0)^3 + 3\frac{d^3f}{dx^2y}(x-x_0)^2(y-y_0) + 3\frac{d^3f}{dxy^2}(x-x_0)(y-y_0)^2 + \frac{d^3f}{dy^3}(y-y_0)^3}{6} \\ & + \ldots \end{aligned} \tag{1}$$

to find z values at non-pixel coordinates (the computer routine that performs this calculation is called ZQuad). Having obtained 3000 plots of x-ray absorption vs. radius, we could then take the finite radial second derivative of each plot and average them together to eliminate

the systematic noise present in each individual plot [Fig. 2-15(a) and (b)]. Figure 2-15(c) shows the quality of radial lines produced by the new method, as discussed below.

The New Method. A closer examination of each individual second derivative plot revealed that the noise problem was caused by taking the radial second derivative of each absorption vs. radius plot finitely. Since each value calculated by ZQuad uses the nearest pixels to approximate a value at a given point (Fig. 2-16), there are small breaks in the surface continuity at pixel boundaries. These small breaks translate into huge spikes in the finite second derivative of radial lines plotted along this surface. To eliminate this noise, the new procedure employs a modified ZQuad that directly calculates the infinitesimal radial second derivative of Eq. (1):

$$\begin{aligned}\frac{d^2 f}{dr^2}(x,y,\theta) = {} & \frac{d^2 f}{dx^2}(\cos\theta)^2 + 2\frac{d^2 f}{dxy}(\cos\theta)(\sin\theta) + \frac{d^2 f}{dy^2}(\sin\theta)^2 + \frac{d^3 f}{dx^3}(x-x_0)(\cos\theta)^2 \\ & + \frac{d^3 f}{dx^2 y}(y-y_0)(\cos\theta)^2 + 2\frac{d^3 f}{dx^2 y}(x-x_0)(\cos\theta)(\sin\theta) + 2\frac{d^3 f}{dxy^2}(y-y_0)(\cos\theta)(\sin\theta) \\ & + \frac{d^3 f}{dxy^2}(x-x_0)(\sin\theta)^2 + \frac{d^3 f}{dy^3}(y-y_0)(\sin\theta)^2 + \ldots\end{aligned} \tag{2}$$

Now that we are able to obtain measurements from individual radii, we can use x-radiography to quantify a wider range of shell characteristics, including layer concentricity and uniformity (Fig. 2-17).

For further information, please contact D. Bernat or Dr. R. Stephens (GA).

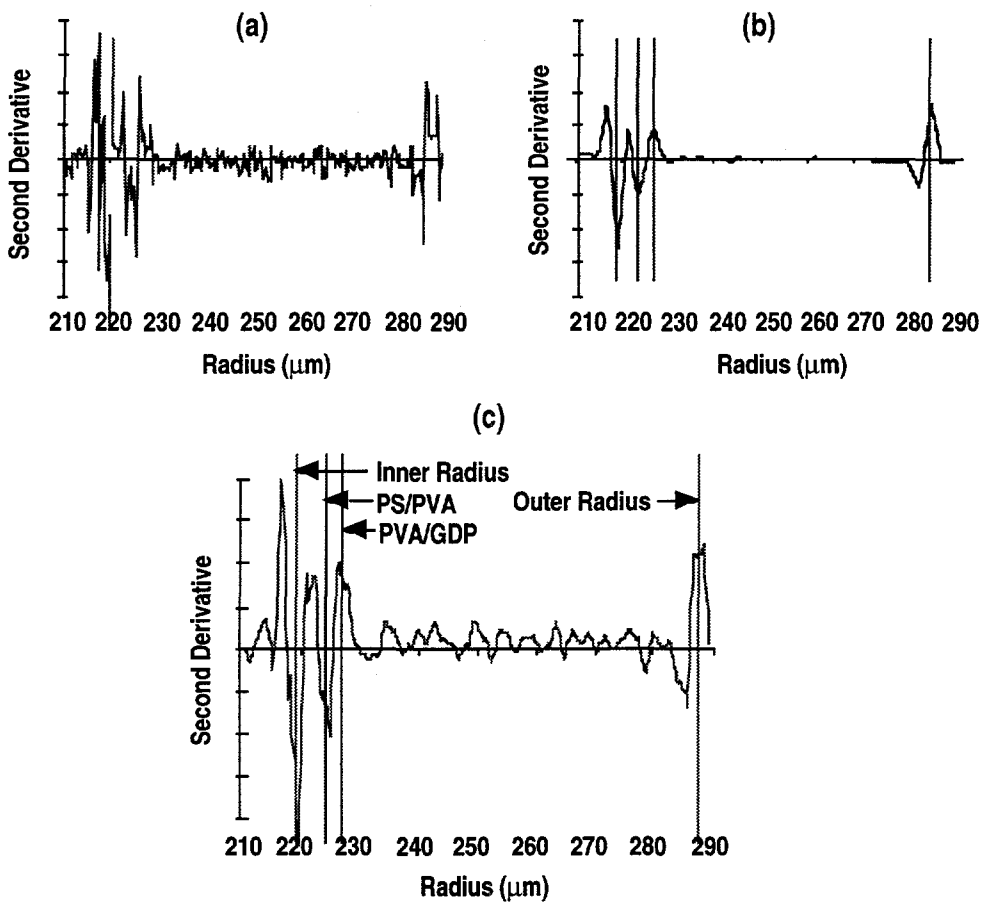

Fig. 2-15. (a) A single radial second derivative line, from the old method. (b) 3000 such lines from all around the shell, averaged. (c) A single second derivative radial line from the new method.

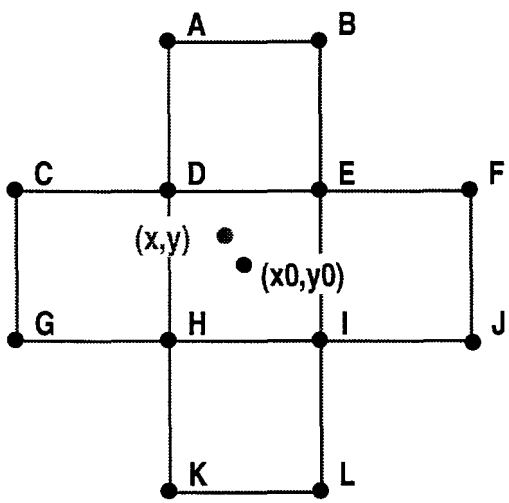

$$\frac{df}{dy} = \frac{I+H}{2} - \frac{E+D}{2}$$

$$\frac{d^2f}{dxy} = (I-H)-(E-D)$$

$$\frac{d^3f}{dxy^2} = \frac{(L-I)-(E-B)}{2} - \frac{(A-H)-(D-A)}{2}$$

$$\frac{d^3f}{dx^3} = \frac{F+J}{2} - 3\frac{E+I}{2} + 3\frac{D+H}{2} - \frac{C+G}{2}$$

Fig. 2-16 (above): Calculating local derivatives for ZQuad.

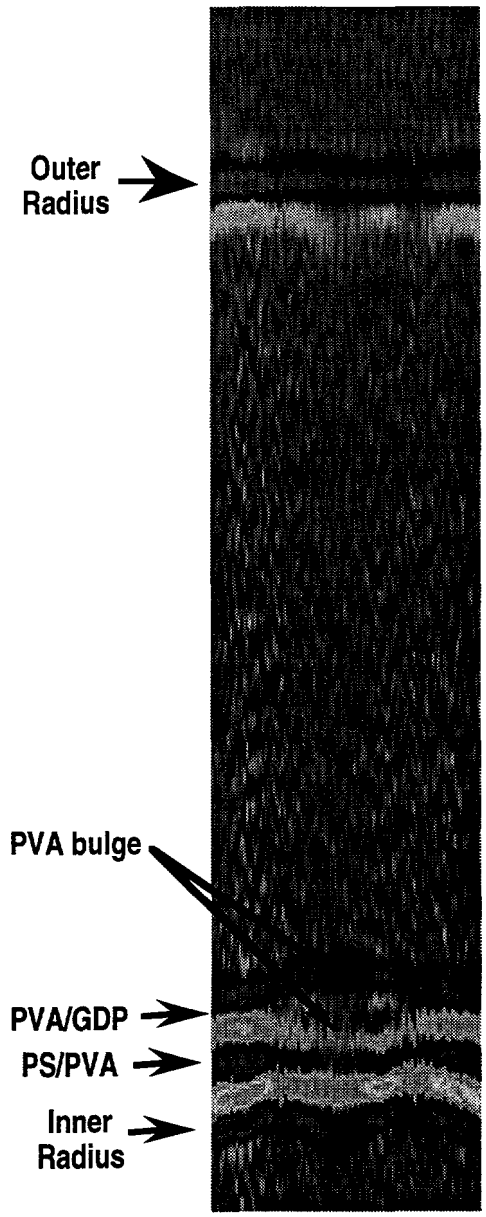

Fig. 2-17. Radial profile produced by the new ZQuad. Due to the quality of the individual radial lines (shown as vertical lines in the radial profile), we can confidently measure the bulge in the PVA layer as being 3 μm thick (from 2.4 μm at 45 degree to 5.4 μm at 170 degree).

2.4.5. XRF CALIBRATION

Our XRF system was previously calibrated for Ar and Ge in capsules. XRF calibration for Si, Cl, and Ti have been completed or are nearly complete. In quantitative analyses via the XRF method, the observed fluorescent x-ray intensities must be corrected for various factors: spectral intensity distribution of the incident x-rays; fluorescent yields; matrix enhancements and absorptions; geometry; detector efficiency; etc. Obviously, for the highest accuracy, calibration of the XRF instrument requires the use of appropriate standards. Since neither suitable commercial standards nor software for analyzing multi-layered hollow spheres are available, we have developed our own appropriate standards and models for precise instrument calibration.

The calibration of the XRF unit is essentially a three step process:

1. Determine the instrument sensitivity for the analyte of interest
2. Prepare and characterize samples of the appropriate geometry doped with the analyte of interest
3. Model results from Step 2 to support the calibration and to allow for changes in sample parameters without the need for recalibration

Determining Instrument Sensitivity. The number of analyte x-ray counts detected per atom per second, in the absence of appreciable absorption or enhancement effects, is the instrument sensitivity factor. This is accomplished first and takes care of effects due to detector efficiency as a function of fluorescence energy and other miscellaneous parameters not specifically addressed. Since chlorine (Cl) was the first element to be calibrated, this was accomplished by analyzing small, thin walled, Cl containing polystyrene spheres precisely measured for o.d. and wall thickness (~450 μm o.d. × ~3 μm wall). These hollow spheres were also analyzed by the commercial combustion method and thus contained an accurately known amount of Cl. Instrument sensitivity for future dopants are then determined by referencing the analyte signal against the Cl in a thin film of sample containing a known stoichiometric ratio of analyte to Cl. For instance, in the determination of the instrument sensitivity for titanium (Ti), pure titanocene dichloride [$(C_5H_5)TiCl_2$] was dissolved in a benzene/polystyrene solution and cast as a thin film (~1 μm thick). Measurement of this film by the XRF system yields the sensitivity of Ti relative to Cl since the Ti:Cl ratio in the film is precisely 1:2. Using sensitivity values determined in this fashion allows for approximate calibration of the XRF system until the time consuming improved calibration process outlined below can be completed.

Preparation and Characterization of Samples. In calibrating the method for improved analysis of capsules the second step is to prepare capsules with varying thickness of GDP doped with a constant concentration of the desired analyte. Constant concentration of analyte is verified by performing the GDP coating process in steps. In the first coating step, mandrels are coated with a couple of microns of doped GDP and then analyzed. These capsules are then returned to the coater along with new uncoated mandrels. A second coating of a couple of microns is applied and analyzed. Analysis of the newly added shells confirms that the concentration of dopant in the second coating process was approximately identical to that in the first step. This process is continued until the final coating thickness is reached — usually about 40 μm. After the coating steps are completed and the precise shell dimensions (o.d., total wall and layer thicknesses, mass and density) and XRF readings are taken, the shells are sent to a commercial elemental analysis laboratory for very precise determination of the total elemental concentrations (i.e., C,H,O,N and analyte of interest). A plot of the XRF signal (corrected for diameter) against doped GDP thickness (Fig. 2-18), in combination with the elemental analysis results by combustion, gives you an accurate calibration of the system for capsules of that particular size and analyte concentration.

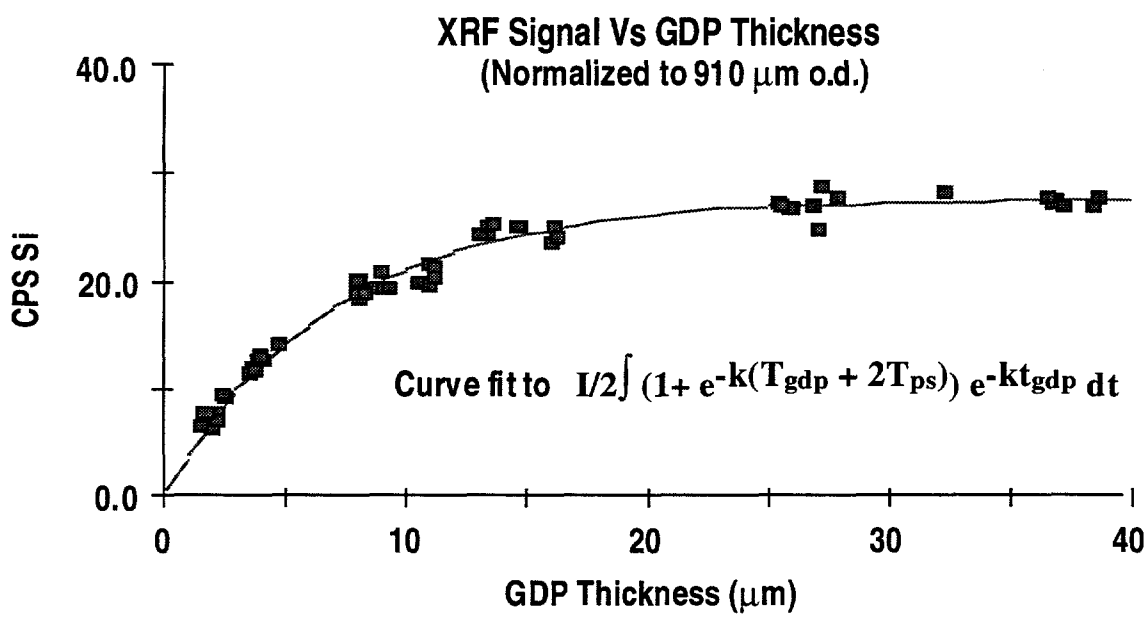

Fig. 2-18. Exponential curve fit of Si doped GDP data for a single Si concentration allows for an accurate calibration of the XRF system for capsules of this particular composition and analyte concentration.

Modeling the Results. A model which includes explicit parameters for the pertinent physics and target dimensions is the next step in the calibration process. This modeling

accurately allows for non-linear changes in various target dimensions and layers given the calibration constant determined by relating the calculated fluorescent intensities to the experimental observations from the previous step. Figure 2-19 illustrates conceptually all of the physical parameters taken into account by the theoretical model developed specifically for the ICF program.

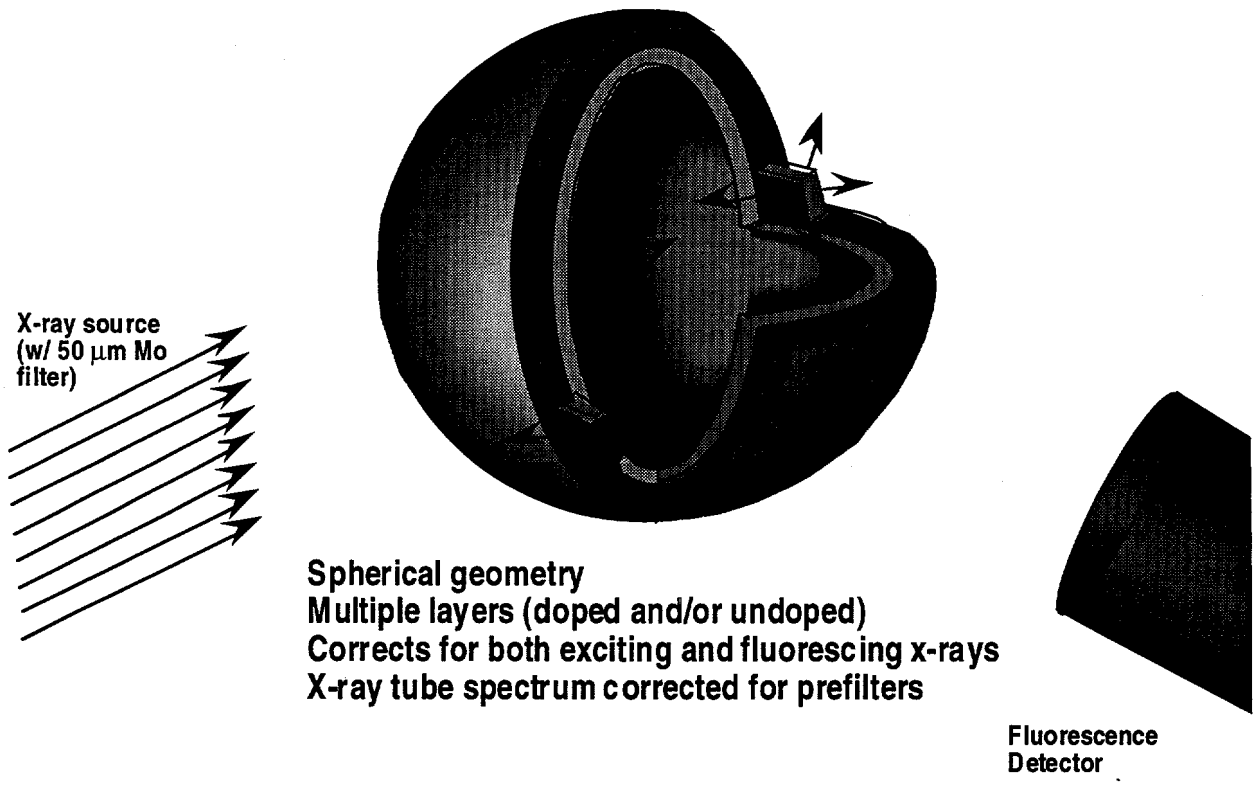

Fig. 2-19. The theoretical model includes explicit corrections for geometry, allows for multiple layers (doped and undoped), corrects for absorption of excitation and fluorescence x-rays, and x-ray filtering of the tube spectrum.

Fundamental parameter methods for quantitative x-ray analysis requires, among other things, a knowledge of the spectral distributions of x-ray tubes used for sample excitation. The algorithm used in this model, developed by Pella, Feng and Small, [Ref. 2-2] is based upon extensive microprobe data and includes the calculation of the continuum and the ratio of the characteristic line(s) to the underlying continuum intensity at the wavelength of the characteristic lines. The equation for the x-ray tube continuum distribution is expressed as:

$$I(\lambda) = 2.72\text{x}10^{-6} Z(\lambda/\lambda_0 - 1)(1/\lambda^2) f W_{ab} \qquad (3)$$

where Z is the atomic number of the x-ray tube target material; λ is the wavelength; f is a term which corrects for absorption of continuum x-rays by the target and W_{ab} is a correction term for absorption by the Be window of the x-ray tube.

Since we generally only use a Mo x-ray tube operated at a single voltage (40 keV), the ratio of the intensity of the characteristic/continuum x-rays is not explicitly calculated in this model but is extracted from a graph of the characteristic/continuum ratios for various target elements [Ref. 2-3]. Once the spectral distribution (corrected for source filters if utilized) impinging on the target is known the next corrections required relate to the ICF capsule. Corrections for x-ray absorption of both the exciting x-rays and the fluorescent x-rays are calculated. This task is accomplished by subdividing the doped spherical capsule into its component layers. The doped layer is then further divided into 10 degree × 10 degree segments (polar coordinates) which results in 648 separate volume elements per doped layer (both the number of layers and the segment size are user selectable). X-ray absorption correction factors are calculated for each volume element on a SUN computer workstation, for both the exciting and fluorescent x-rays, utilizing elemental mass absorption coefficients for various capsule components. Elemental mass absorption coefficients as a function of x-ray energy are taken from data tables generated by Lawrence Livermore National Laboratories [Ref. 2-4]. The calculated intensity of the resulting fluorescence spectrum for each target is plotted as a function of doped layer thickness and compared to the experimental data. A prefactor (which essentially relates to the instrument sensitivity factor) in the model data is then adjusted to give the best fit of the model data to the experimental data. Once this step is complete, recalibration of the XRF system for changes in target dimensions and elemental concentrations is readily accomplished by use of the model only. Figure 2-20 illustrates the expected intensity curves for various concentrations of silicon (Si) dopant and three different undoped inner mandrel thicknesses.

Development of this precise model allowed for the detection of a previously unnoticed small change in silicon concentration in one of our silicon (Si) doped GDP coating experiments. This small change in concentration is apparent when examining the fit of the model data to the experimental data shown previously in Fig. 2-20. If the model data is recalculated assuming a 7% decrease in Si concentration after the initial 14 μm of doped GDP had been deposited, the fit to the data is much better (Fig. 2-21). Analysis of the control samples put into the GDP coater at various times during the coating run are consistent with this observation of decreased Si doping level.

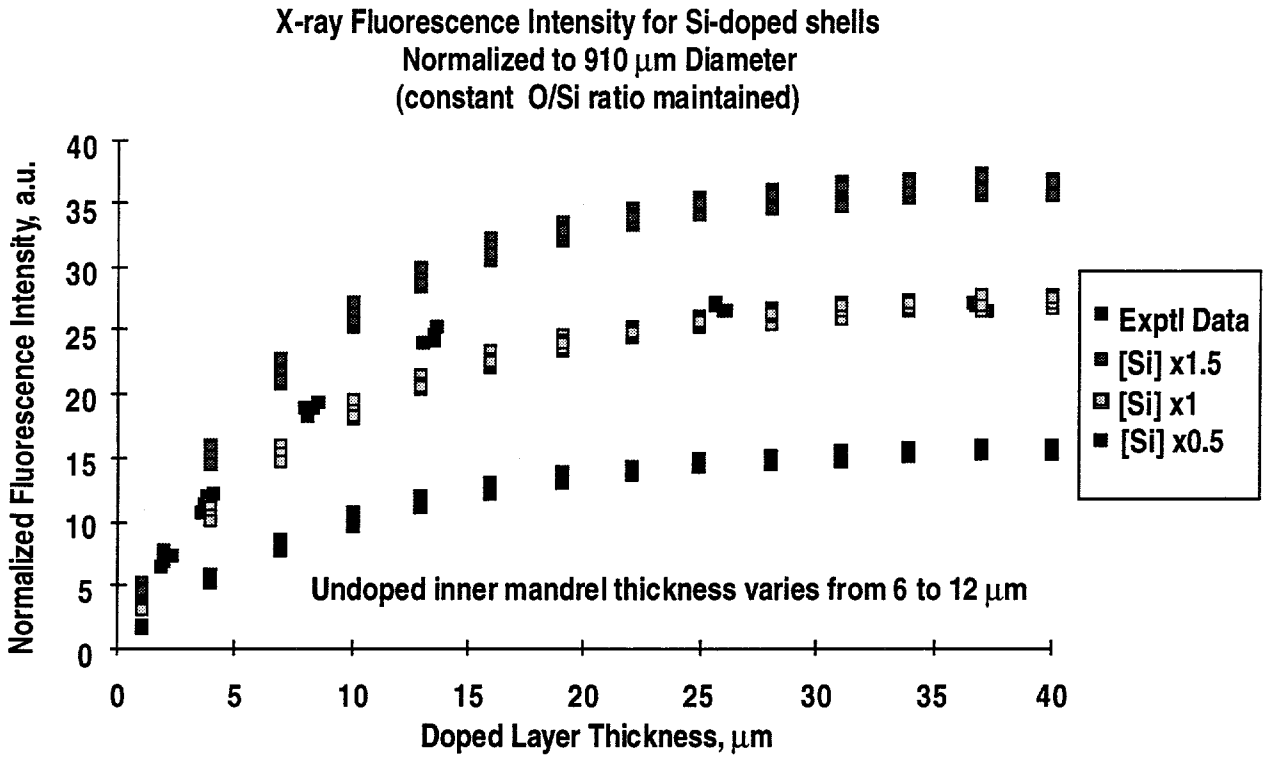

Fig. 2-20 The calculated intensity of the resulting fluorescence spectrum for targets with an undoped inner mandrel thickness of 6, 9 or 12 μm and three different Si concentrations is plotted as a function of doped layer thickness. The middle curve ([Si]x1) is the fit of the experimental data.

For further information, please contact Dr. R. Stephens or Dr. M. Hoppe (GA)

2.5. REFERENCES

[2-1] R.B. Stephens, "1994 ICF Annual Report," General Atomics Report GA-A21966 (1995), p. 2-18.

[2-2] C. Brundle, C. Evans, and S. Wilson, *Encyclopedia of Materials Characterization,* Butterworth-Heinemann and Manning (1992).

[2-3] P. Pella, L. Feng, and J. Small, "An Analytical Algorithm for Calculation of Spectral Distributions of X-Ray Tubes for Quantitative X-Ray Fluorescence Analysis," *X-Ray Spectrometry*, **14(3)**, 125 (1985).

[2-4] "Compilations of X-ray Cross Sections," Lawrence Livermore National Laboratory Report UCRL-50174-SEC 2-R1.

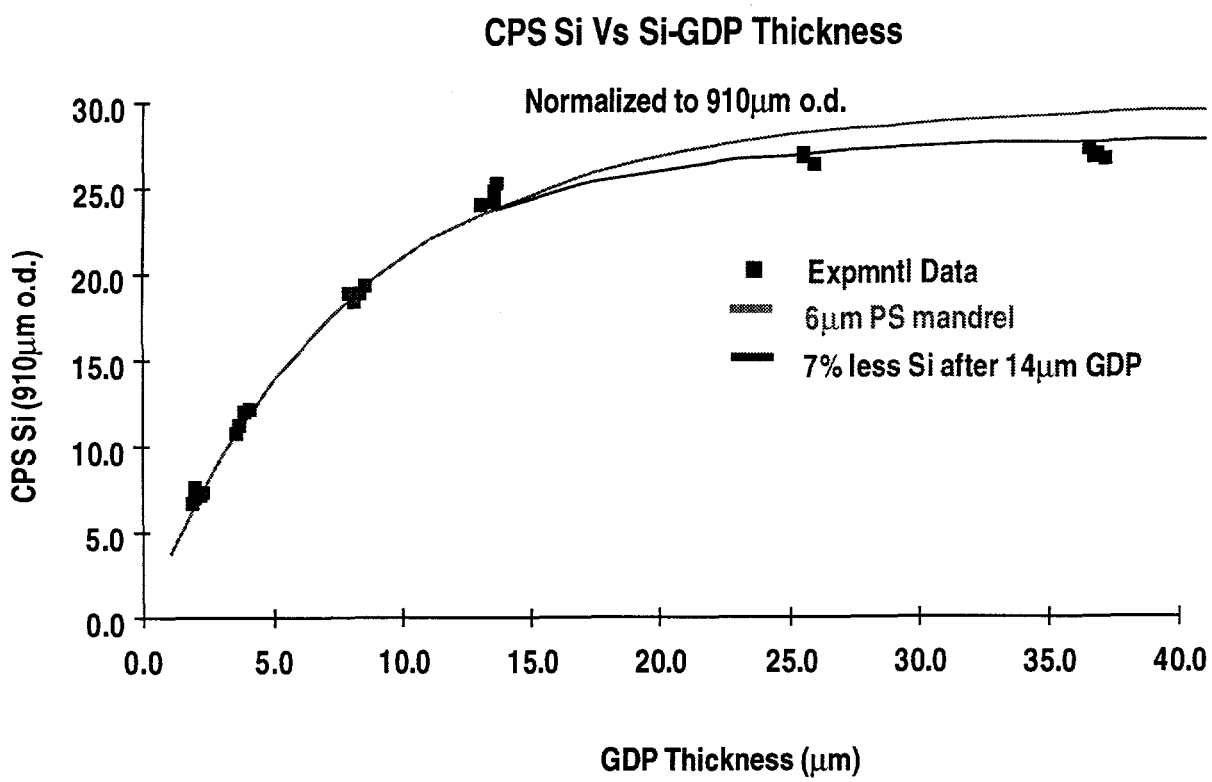

Fig. 2-21. The model data is recalculated assuming a 7% decrease in Si concentration after the initial 14 μm of doped GDP had been deposited. The fit to the experimental data is improved significantly.

3. MICROMACHINED TARGET COMPONENTS

In FY96, we began to produce components that were more complex than the hohlraum mandrels and wedge witness plates that we produced in prior years. This increase in our micromachining capability was a result of the experience we gained producing hohlraum mandrels and witness plates. A number of the complex components that we produced and the techniques that we used to produce these components are described below.

3.1. "TOP HAT" ALUMINUM WITNESS PLATES

A drawing of a top hat witness plate is shown in Fig. 3-1. The production of these witness plates posed a number of challenges. First, the witness plates are quite small so that machining and handling had to be carried out with extreme care so as not to damage the component. Second, the witness plates required two separate machining operations, one to finish one side of the plate and the second to finish the other side. Finally, machining of the recess required the use of a specially produced diamond tool.

The first machining operation produced a shaped plate that was attached to an arbor as is shown in Fig. 3-2. At this stage the top of the hat was longer than the specified length. The diamond tool used to machine the recess was specially designed so that the bottom corner did not interfere when cutting the inner diameter as shown in Fig. 3-3.

After measuring the dimensions with a laser micrometer and a machinist's microscope, the partially machined plate was separated from the arbor by cutting at the small-diameter neck. The machined side was then glued to a previously machined plate using an acetone soluble cement, and the plate was mounted onto the lathe. The surface of the top of the hat was used as a reference and the part was machined to reduce the length of the top to the specified value. The plate was then removed from the lathe, the cement was removed with acetone and the lengths were measured with an interference microscope. We found we easily were able to control diameters to ± 4 μm on these parts.

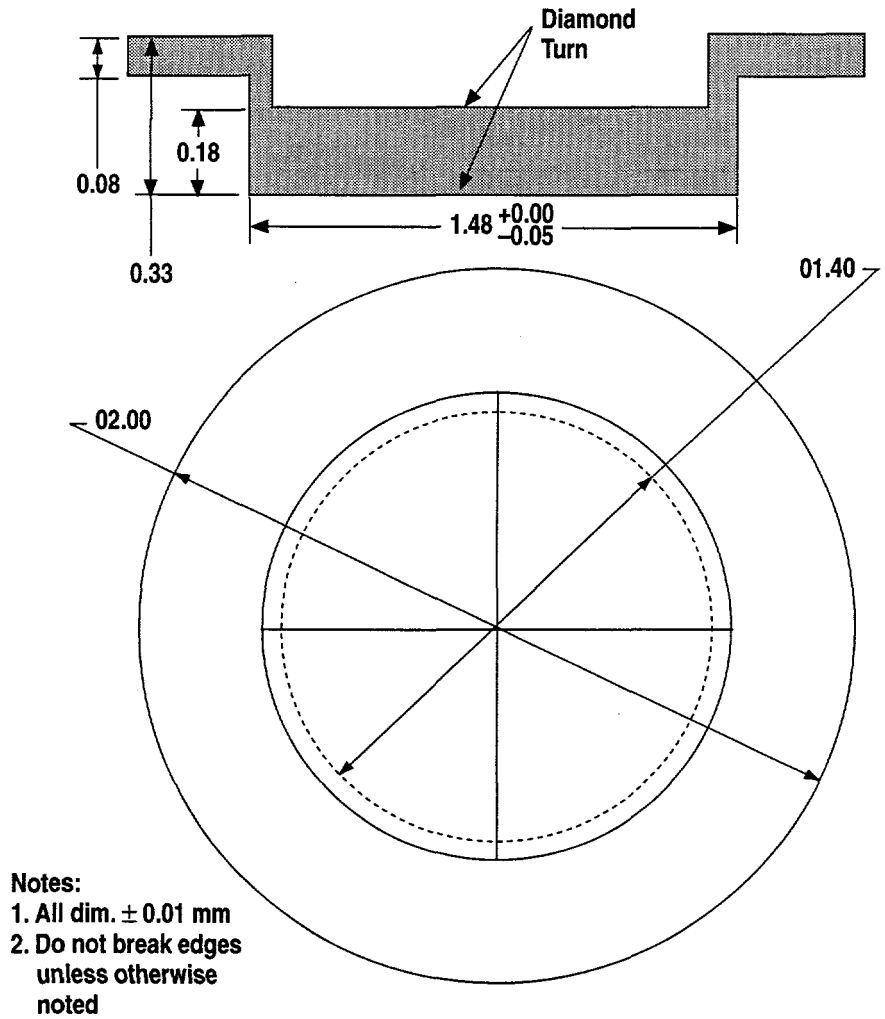

Fig. 3-1. Illustration of "Top Hat" witness plate configuration

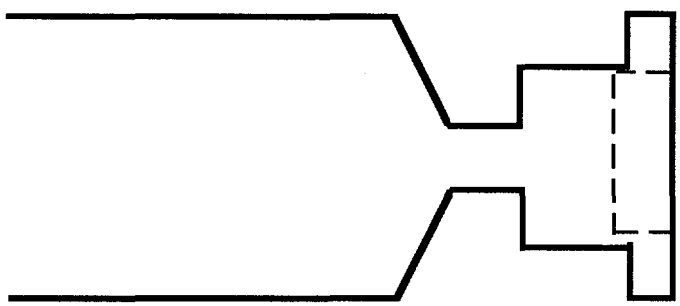

Fig. 3-2. Sketch of Top Hat attached to an arbor

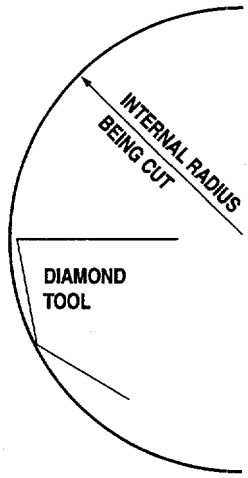

THE BOTTOM CORNER OF THE DIAMOND INTERFERES WITH THE RADIUS OF THE HOLE

Fig. 3-3. Tool interference drawing

A photograph of a finished aluminum top hat is shown in Fig. 3-4. The diameter of this piece is about 2 mm.

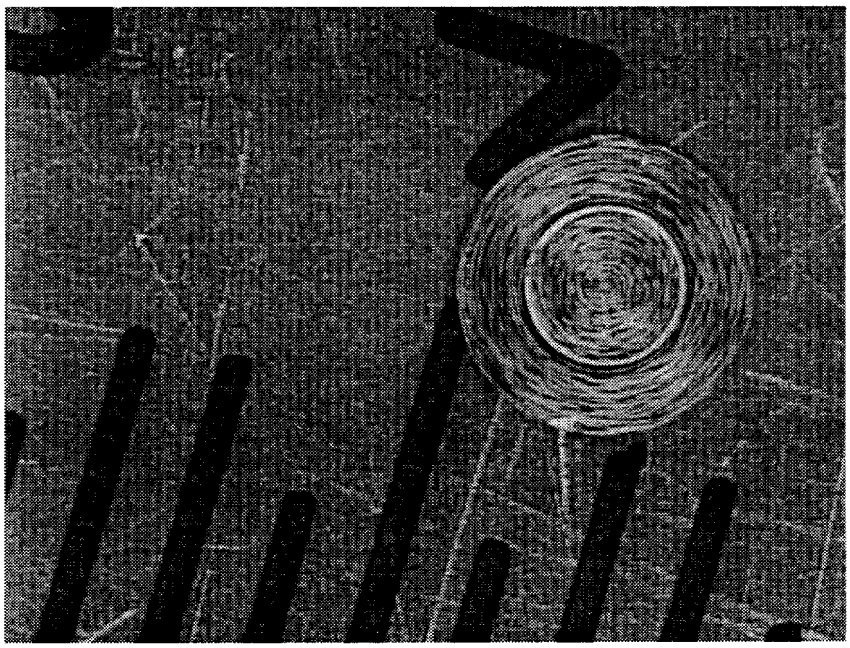

Fig. 3-4. Photo of finished Top Hat

3.2. THIN-WALLED TUBES

Gold Tubes With Constant Wall Thicknesses. The very small, thin-walled gold tubes that we produced were made using techniques that were identical to the techniques that we use to produce hohlraum mandrels. That is, a copper mandrel was machined to the required inner diameter of the tube and then the mandrel was plated with gold. However, in this case rigorous control was required during machining and plating because the tube diameters were small and the gold thickness was very thin (2 μm).

Gold Tubes With Tapered Wall Thicknesses. A drawing of a thin-walled very small gold tube with a tapered wall thickness is shown in Fig. 3-5. These tubes were identical in diameter to the tubes described above. Because it is not practical to deposit a tapered gold coating, it was necessary to machine the gold coating after deposition to produce the taper. However, if the mandrel was removed from the lathe for plating, as is the method that is used for hohlraum mandrels where machining after plating is not required, it would be very difficult, if not impossible, to obtain the required uniformity in the tube thickness when it was reinserted into the lathe because the part would not turn concentrically. Therefore, the mandrel could not be removed from the lathe for coating. This required us to develop a technique for plating the tube mandrel in the lathe. The setup developed to do this is shown schematically in Fig. 3-6. The BD10 gold plating solution that we use to plate hohlraum mandrels was used in plating the tube mandrels in the lathe. Since the plating operation required about one hour, we found that it was imperative that we machine a reference diameter on the shaft above the tube mandrel so that we could adjust the drift of the lathe position encoders during the plating operation. In this way we could achieve dimension control on the diameters to about ± 0.5 μm. We delivered the tubes to LLNL with the copper mandrels in place. The mandrels were dissolved out at LLNL prior to use. A photograph of one of these small diameter gold tubes with a tapered wall thickness is shown in Fig. 3-7.

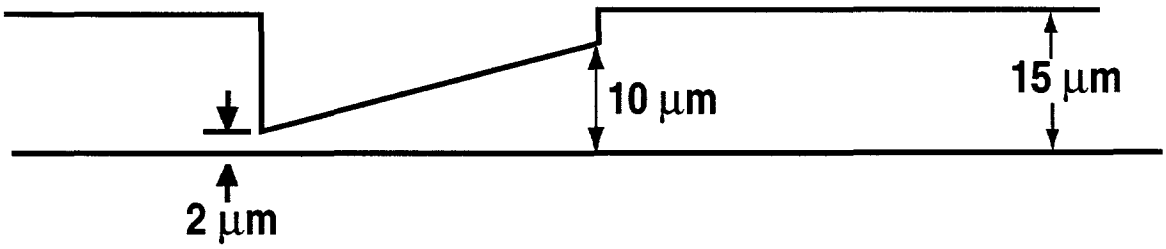

Fig. 3-5. Illustration of a thin-walled gold tube with a tapered wall thickness

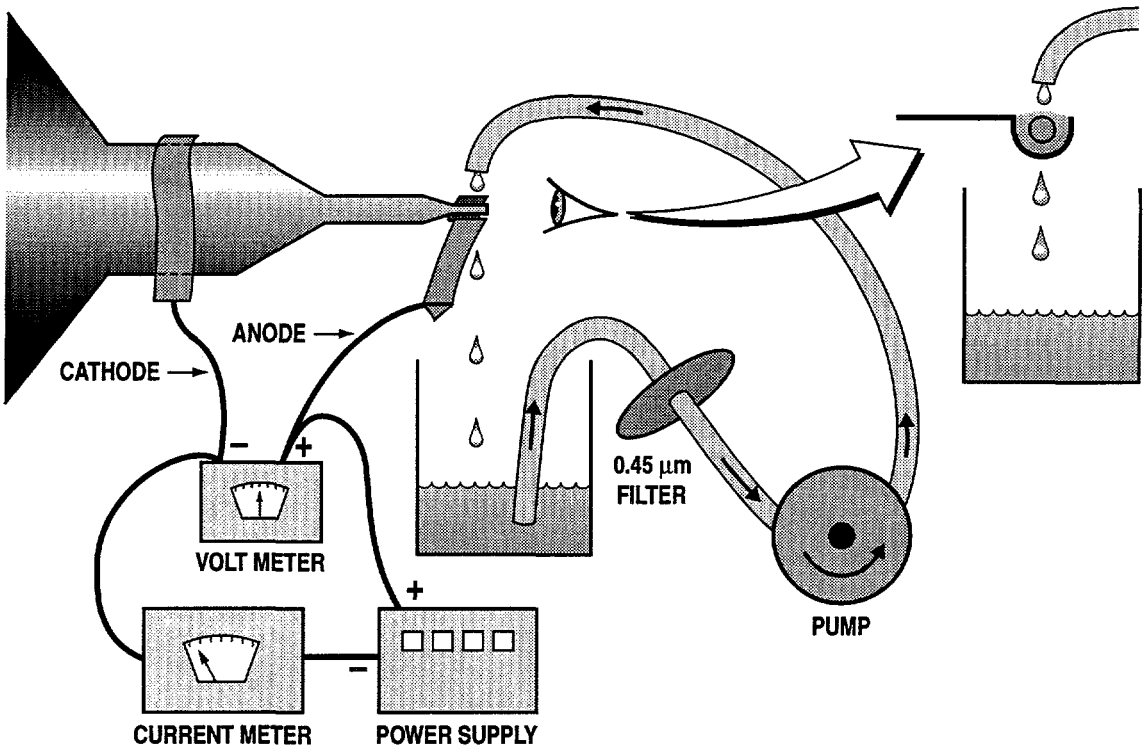

Fig. 3-6. Schematic of setup for plating in the diamond turning machine

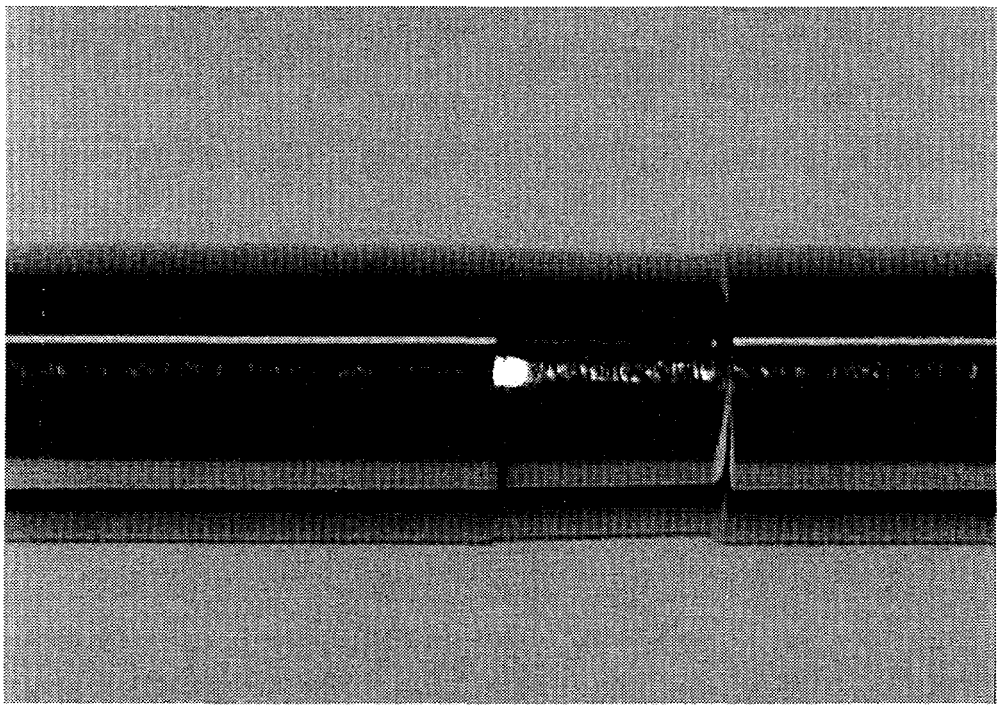

Fig. 3-7. Photo of small gold tube with a tapered wall thickness

Gold And Silver Tubes With Tapered Wall Thicknesses. The most complex components we produced this year were thin walled, small gold and silver tubes with tapered wall thicknesses. A drawing of one of these tubes is shown in Fig. 3-8. They were identical in diameter to the other tubes we produced. The difference was the silver region in the middle of the tube. This silver region presented a special difficulty. Acids that readily dissolve copper also dissolve silver. Thus we could no longer use copper for the tube mandrel. Because we use diamond tools to machine the mandrels to obtain a fine surface finish and rigid dimensional control, the choice of other mandrel materials is limited to those that do not form carbides. It is difficult to obtain high-quality electroplated coatings on aluminum which is the other logical choice after copper. We considered using a plastic with a sputtered conductive coating that would then be remachined to obtain concentricity, but sputtered coatings do not adhere well to plastics. Ultimately, we selected zinc for the mandrel material. It dissolves in hydrochloric acid which does not affect silver or gold and machines well with diamond tools. It's only drawback is that it is soft and deforms easily so it must be machined very carefully to prevent plastic bending during machining. To overcome this liability, we are currently investigating the use of a 0.85 Zr/0.15 Al alloy for use as the mandrel. (The initial tubes were made with pure zinc mandrels.)

The machine-plating sequence used to produce the thin-walled gold and silver tubes was as follows:

1. Machine the zinc mandrel to the specified inner diameter of the tube.
2. Without removing the mandrel from the lathe, plate a thick layer of silver on the zinc mandrel. (Plating involved the application of a silver dip-coating to seal thesurface before beginning electroplating because the electroplating solution reacted with the zinc.)

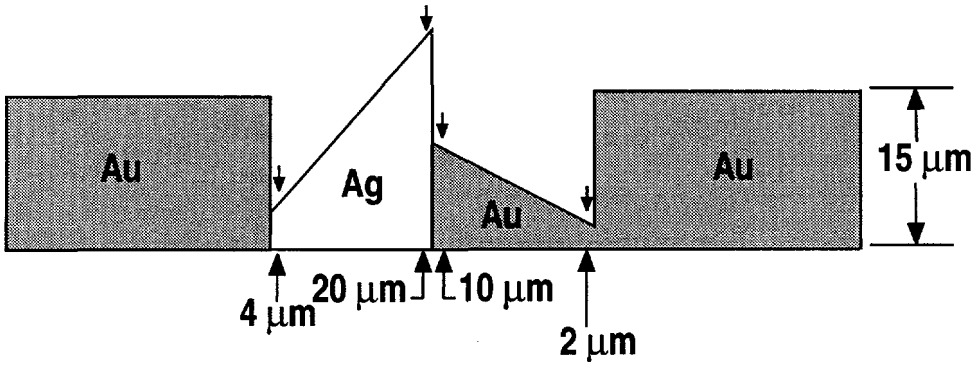

Fig. 3-8. Drawing of gold and silver tube

3. Touch-off on the reference position to adjust for position encoder drift, and then machine the mandrel to remove the silver except for a band at the position of the silver taper.

4. Without removing the mandrel from the lathe, plate a thick layer of gold on the zinc mandrel. (As with the silver, gold by dip-coating was applied to the mandrel to seal the surface before beginning electroplating to prevent reaction of the electroplating solution with the zinc.)

5. Touch off on the reference position again to adjust for position encoder drift, and then machine the specified coating profile in the gold and silver, removing all of the coating at each end of the tube.

A completed gold and silver tube still on the zinc mandrel is shown in Fig. 3-9.

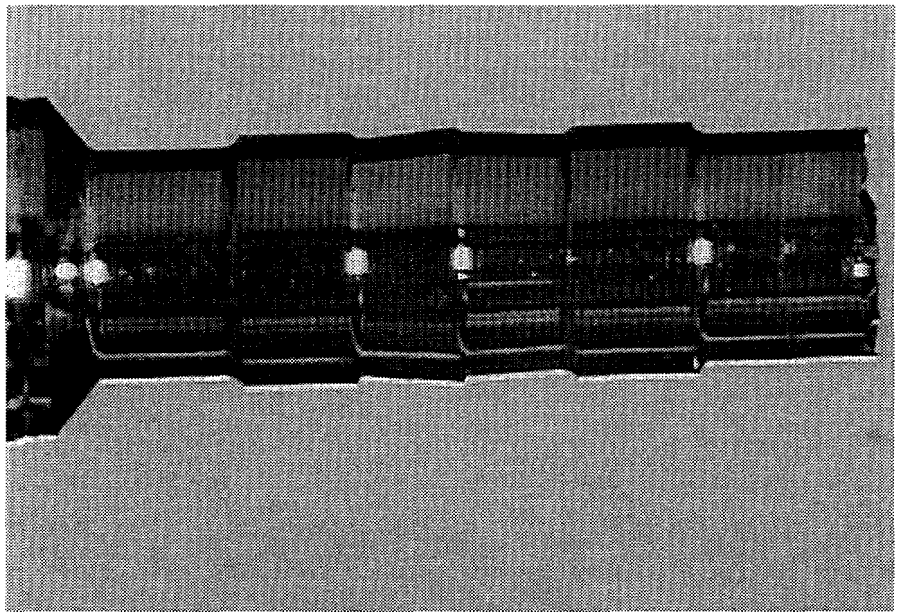

Fig. 3-9. Photo of gold and silver tube

3.3. THIN COPPER DISCS WITH A BESSEL FUNCTION-SHAPED DIMPLE

A cross-sectional drawing showing the thin disc with a Bessel Function-shaped dimple in one side requested by LLNL is shown in Fig. 3-10. The disk material is copper.

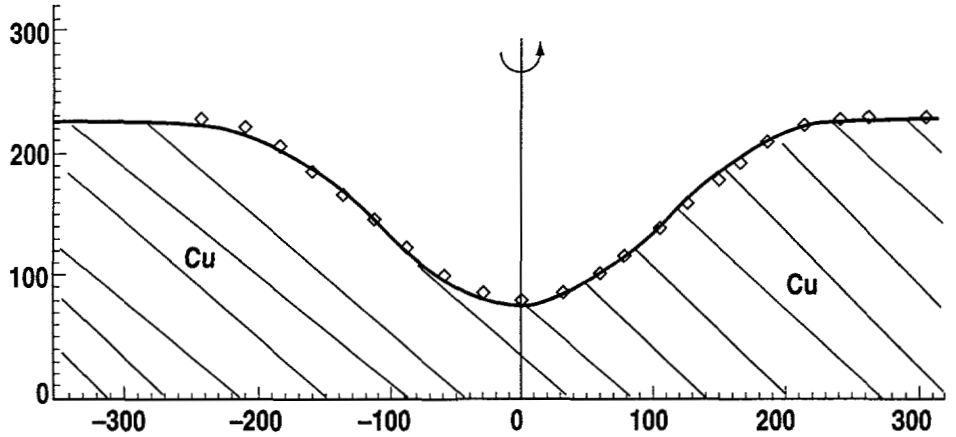

Fig. 3.10. Drawing of disc with dimple

It is not practical to machine a small dimple like the one shown in Fig. 3-10. Tool interference, such as the one shown previously in Fig. 3-3, prevents machining with a standard diamond tool and for the same reason even a specially designed tool such as the one used to cut the re-entrant hole in the top-hats cannot be used to cut the small dimple of Fig. 3-10. Perhaps one way to cut the dimple would be to fabricate a specially shaped drill, but unless the drill was diamond tipped, the surface finish would not be as good as that obtained with normal diamond machining. An alternate approach and the one we chose to produce the dimpled discs was a variation of that used to fabricate hohlraums. In this approach, the negative of the dimple (a Bessel Function-shaped mound) was machined on a face of a zinc cylinder. (Zinc was chosen because it could be dissolved without affecting copper and copper could be electroplated on it.) At some distance from the face, a shoulder was machined on the cylinder for radial and axial reference positions. The cylinder was removed from the lathe and a thick layer of copper was electroplated on it. (It was not necessary to electroplate in the lathe in this case because concentricity on returning to the lathe was not as critical as it was with the tubes.) The cylinder was returned to the lathe; axial and radial references were obtained from the shoulder; and the copper coating was machined to the specified diameter and thickness as shown in Fig. 3-11. The cylinder was then removed from the lathe and the zinc was dissolved leaving behind a copper disc with a Bessel Function-shaped dimple in one side. That the dimple shape in discs made this way adhered well to the shape of a Bessel-Function is shown in Fig. 3-12.

For further information, please contact Dr. J. Kaae (GA)

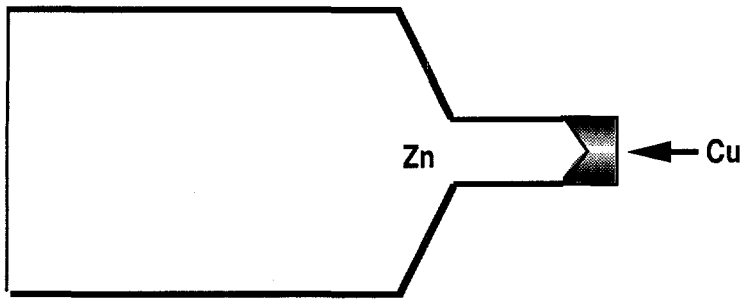

Fig. 3-11. Sketch of copper disc on mandrel

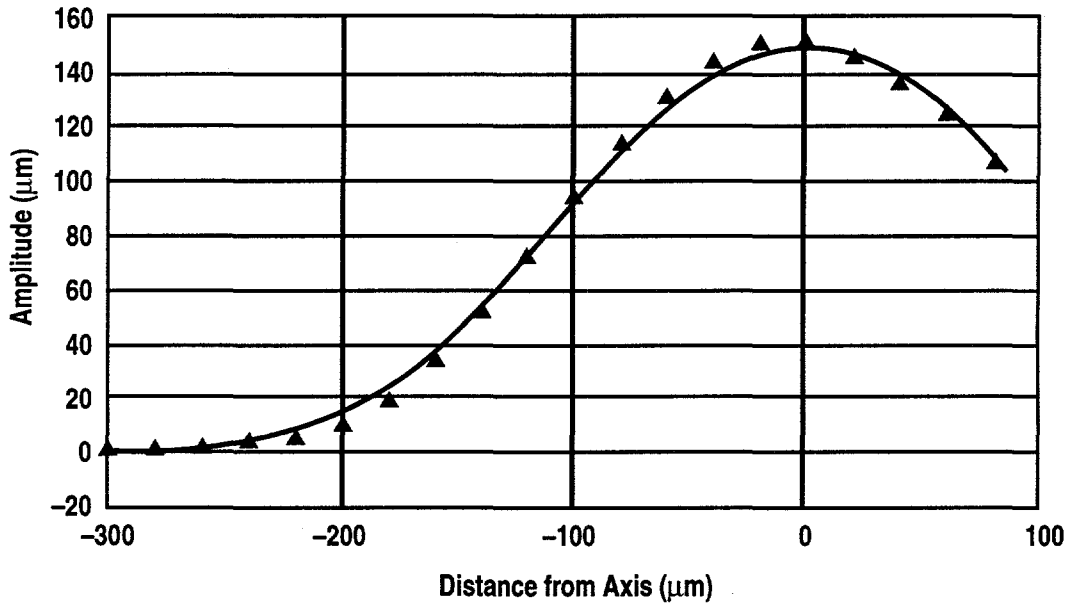

Fig. 3-12. Profile of dimple compared to a Bessel Function

3.4. DEUTERATED POLYETHYLENE FILMS FOR SANDIA TARGETS

Sandia National Laboratory requested us to fabricate relatively thick (~250 μm) deuterated polyethylene films on stainless steel substrates this year. Although Sandia had carried out some initial development work on fabricating these films, procedures for fabricating the films were not nearly complete and we found we had to carry out a development effort in order to successfully fabricate the films.

Deuterated polyethylene powder was available commercially. The films were to be cast on to the stainless steel substrates so we first had to define the best solvent for the commercial powder. Four solvents were evaluated: mesitylene, trichlorobenzene, P-xylene and O-xylene. These solvents were evaluated by mixing a given amount of deuterated

polyethylene powder with a relatively large amount of the solvent, heating the mixture to slightly below the boiling point and holding at this temperature overnight. The effectiveness of the solvent was then measured by measuring the amount of undissolved deuterated polyethylene. O-xylene turned out to be the best solvent.

Both the temperature of the solvent-polyethylene mixture and the temperature of the mold were varied to optimize the film density and the adhesion to the stainless steel substrate. With solvent-polyethylene temperatures higher than 110°C, the mixture would stick to the glass heating flask and pouring of the mixture into the molds was difficult. The mold was made up of a 10 cm × 15 cm aluminum tray containing a 0.6 cm thick silicon wafer on top of which were the stainless substrates. The tray was heated with a hot plate over the range 35°C to 100°C. Tray temperatures near 100°C produced very low-density films with many pores. The optimum tray temperature was 45°C. We produced many films in the optimization process. The best films were produced by mixing the solvent-polyethylene at 110°C, casting into a mold at 45°C in three separate pours. This procedure produced films which adhered well to the stainless substrates but the films were opaque and below the 1.05 g/cc density required by Sandia. The films were densified by heating at 120°C for 30 minutes after which they were clear and had densities above 1.05 g/cc. Pictures of the deuterated polyethylene films on two different substrates are shown in Figs. 3-13 and 3-14.

For further information, please contact Dr. J. Kaae (GA)

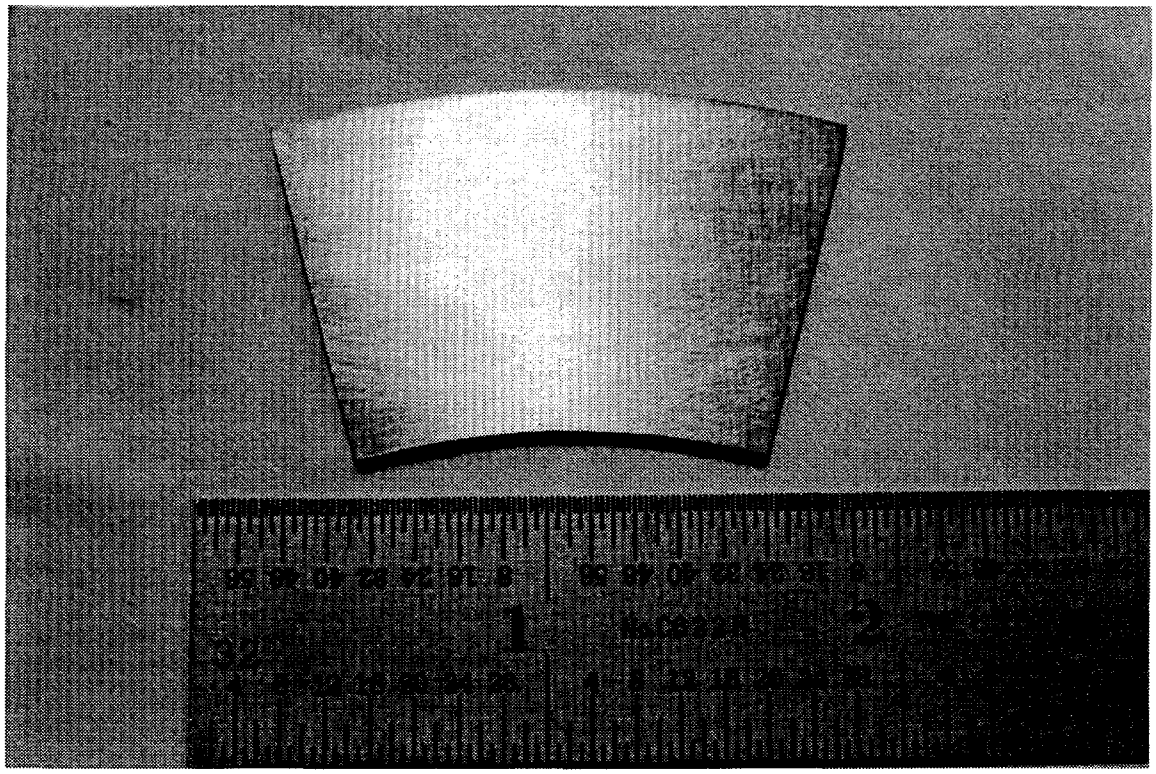

Fig. 3-13. SABRE Target Design for Deuterated Polyethylene Films

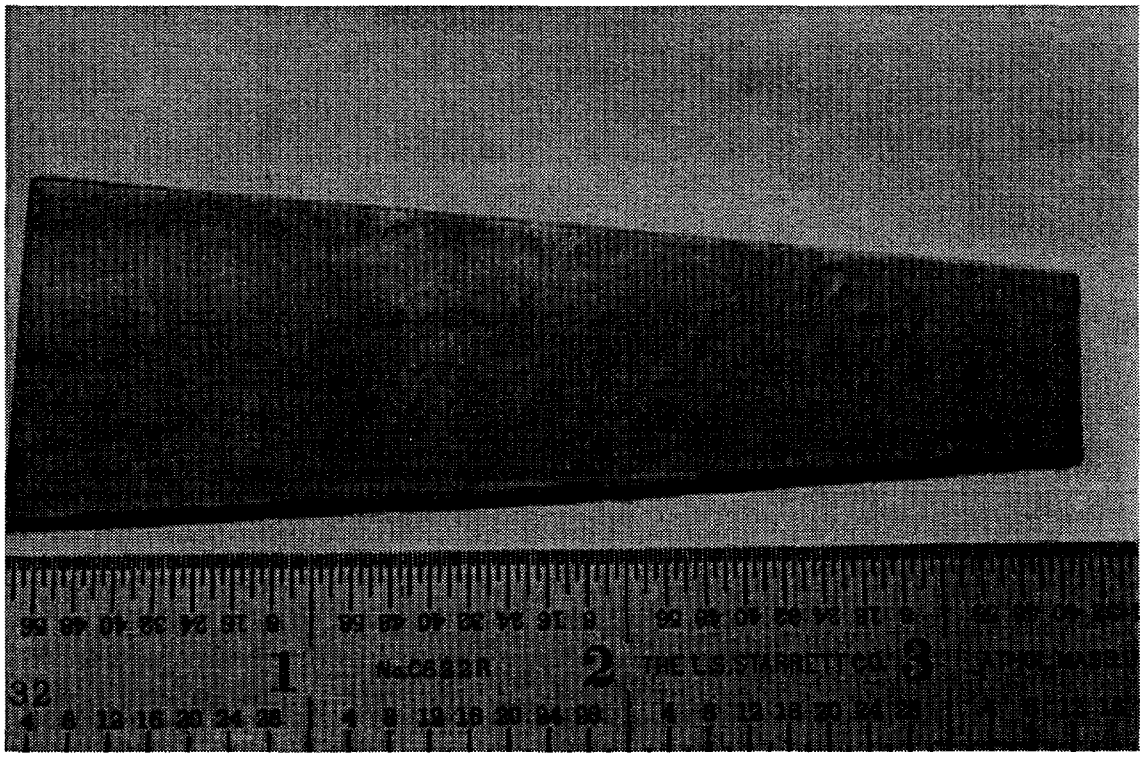

Fig. 3-14. PBFA-II Target Design for Deuterated Polyethylene Films

4. NIKE TARGET DELIVERIES

The targets for the NIKE laser are flat hydrocarbon polymer foils with surface morphology, foil curvature, geometrical dimensions, and chemical composition which meet the specifications set forth in detail by the NIKE project team at NRL. During FY96, WJSA delivered mounted single foil targets with thickness between 10 μm and 100 μm; double foil targets with hydrocarbon top foils and hydrocarbon or opaque second foils, aluminized foils, and foils with patterns impressed in the surface. In addition, we delivered several unmounted foils of the various types mentioned above.

During FY96, we improved the quality of the NIKE laser targets shipped to NRL. Improvements were made in areas of film casting, handling, and target foil mounting processes as described below.

4.1. THICKNESS UNIFORMITY

Previously the flat films we cast on silicon wafers had very good surface smoothness (roughness was generally less than one-fifth of the 10 nm NRL specification), but the thickness of the film varied over the area of the casting. We could easily find several targets of the appropriate thickness from a casting, but much of the material was discarded because it was too thick or too thin. It was determined that thickness variations resulted when the polystyrene-toluene solution dried too quickly, increasing the viscosity of fluid before it spread evenly over the casting area. Attempts were made to lower the solvent evaporation rate by using solvents with lower vapor pressures, lowering the temperature of the casting to retard evaporation, and increasing the partial pressure of the solvent in the air above the casting by decreasing the air volume. None of these attempts seemed to have much effect, so we tried other methods of spreading the fluid evenly over the substrate. By floating the silicon wafer substrate on water in an ultrasonic cleaner, we were able to vibrate the fluid to hasten its spreading. We found that foils cast using this technique were very uniform in thickness with only one or two microns thickness variation over the entire usable surface. Since this method works so well, we fabricated round acrylic boats (Fig. 4-1) to float the wafers in the ultrasonic cleaner tank and routinely use the boats for casting.

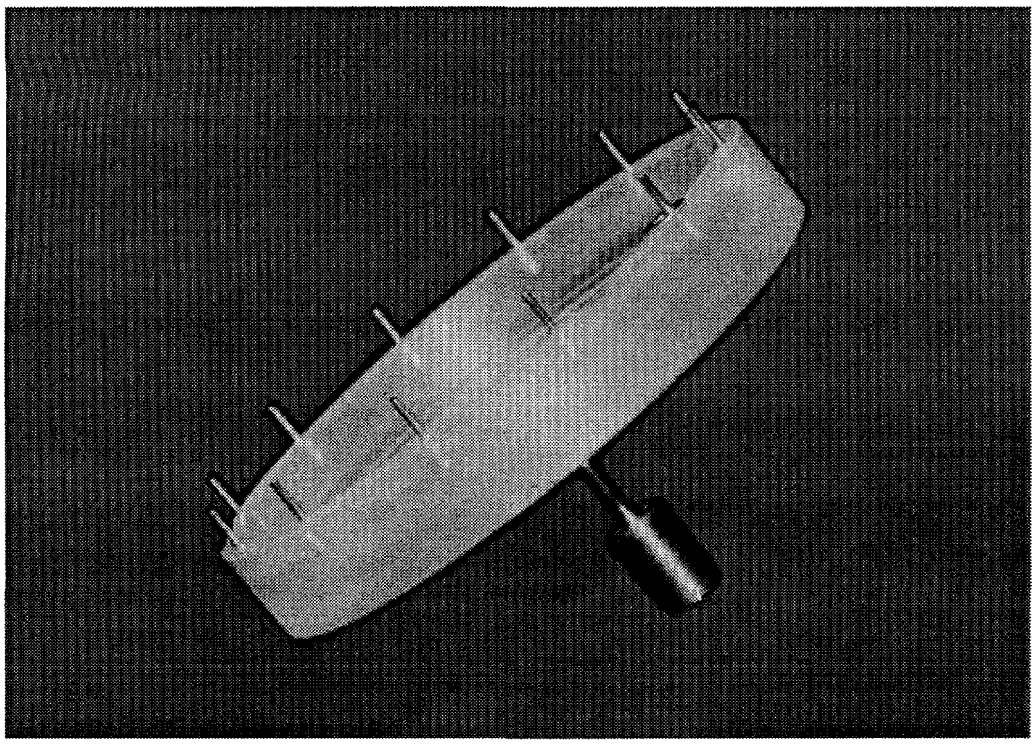

Fig. 4-1. Acrylic boat used to float wafers in ultrasonic tank.

4.2. THICKNESS CONTROL

With increased control over thickness uniformity came a requirement for increased control over thickness. Earlier, to cast a given thickness foil we mixed polystyrene — toluene solutions with concentrations that had yielded the desired thickness (Fig. 4-2). We would then fill the mold or wafer with the solution, let it dry, map the thickness of the entire casting, and choose areas with the thickness we needed). Precision in casting was not necessary since the variation in thickness meant there would likely be some area with the correct thickness even if the mixture and volume were not carefully controlled.

Now that we make very uniform castings we must use precise mixtures and volumes of material. For most castings, we can calculate the thickness simply by calculating the volume of polystyrene deposited and dividing by the surface area of the casting,

$$t = \frac{V_{sol}}{\pi \cdot r^2} \cdot \frac{C_{ps}}{\rho_{ps}}$$

where t is the thickness of the casting, V_{sol} is the volume of mixture deposited, C_{ps} is the concentration of polystyrene in the solution in grams per milliliter, ρ_{ps} is the density of dry

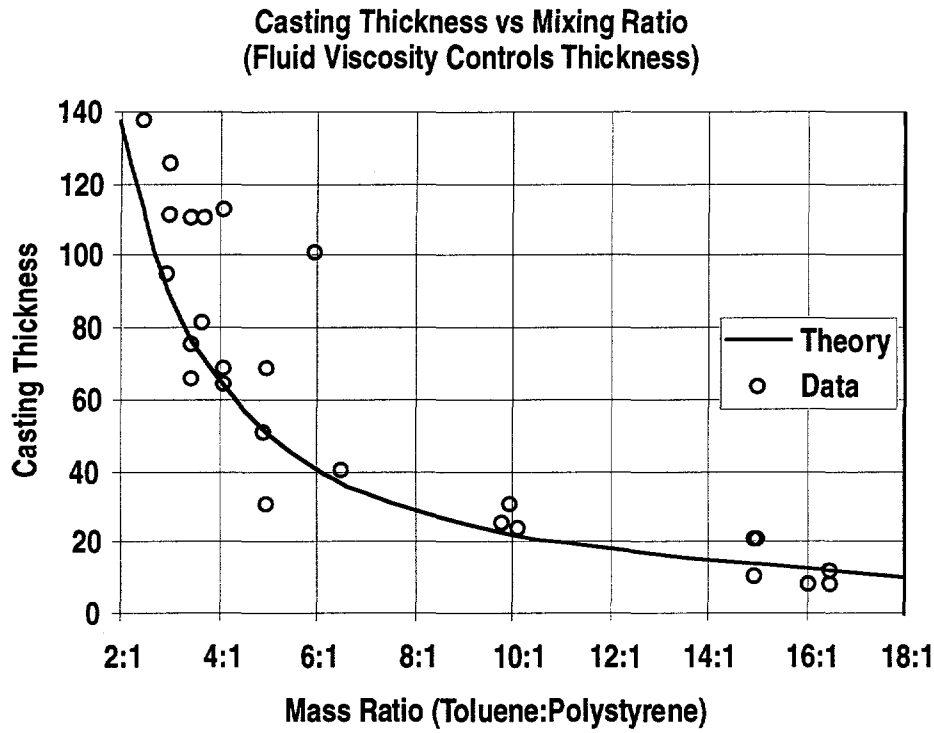

Fig. 4-2. Graph of casting thickness vs. mass ratio (toluene:polystyrene) for obtaining desired film thickness.

polystyrene, and r is the casting radius of the substrate. This approach is generally a good approximation of the targets' thicknesses except around the edges of the casting. As the toluene in the mixture evaporates, polystyrene tends to accumulate at the edge of the casting making a raised circumferential ridge. This boundary region accumulation effect is insignificant in castings with radii larger than about four centimeters, but is dominating in small castings. Controlling the thickness of castings with one or two centimeter radii still requires a great deal of judgment and experience in addition to the calculations we normally perform.

We have also improved our ability to predict thicknesses by increasing control over variables in the thickness equation. Solutions are now mixed as standard solutions rather than by mass ratio, and wafer casting radii are controlled by drawing circular ink "fences" on the wafer with a marking pen. With care the solutions usually do not flow across the ink marks on the wafer so the circular marks provide significant containment boundaries to the casting solutions.

4.3. LEVELING

Previously, we leveled castings by floating the mold or wafer on a eutectic alloy of gallium and indium (75 wt.% Ga — 25 wt.% In). This was successful because the molds were very buoyant in the gallium-indium so they did not tilt on the surface of the liquid. Now that we cast on water, we must prevent thickness gradients by keeping the substrate level as the toluene evaporates. This is especially important because any tilting can cause the solution to run toward the low side, increasing the tilt even more. Our present method is to set up a vertical reference by reflecting a nearly vertical laser beam from the surface of the water in the ultrasonic cleaner (Fig. 4-3). The position of the dot made by the reflected beam is marked on a screen about two meters above the water's surface. A casting substrate is then put in the boat and floated on the water so that the laser beam will now be reflected off the casting surface. We then add or remove weights from the edge of the boat until the dot made by the reflected beam on the screen coincides with the mark made earlier. This assures that the casting surface is level. We make minor leveling adjustments after pouring the solution to compensate for any additional asymmetry introduced. This is done by adding or removing weights to the edge of the boat until the laser beam reflected from the surface of the substrate under the solution is superimposed on the reflection from the surface of the liquid (which should be quite flat and level far away from the edge of the casting).

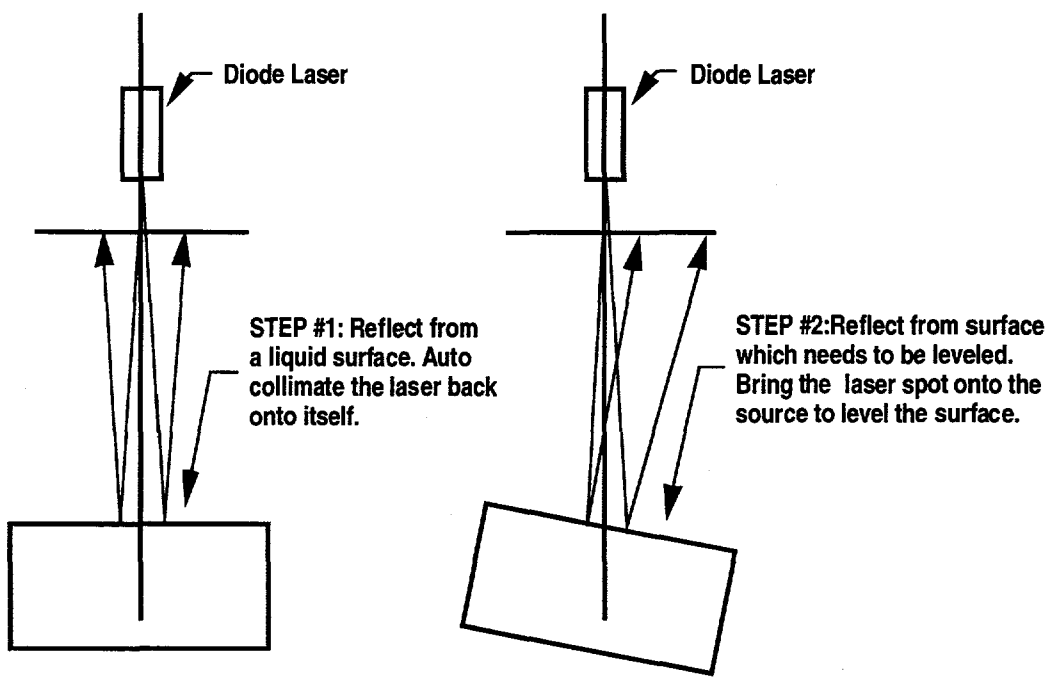

Fig. 4-3. Diagram of method used to level castings with laser beams

4.4. ALUMINUM COATING

To fill the NRL requests for aluminum coated CH foil targets, we constructed a standard bell-jar vacuum system in which CH films could be coated with thermally evaporated aluminum layers.

Using standard practices for evaporation of the aluminum (Al), short lengths of aluminum wire are bent into a hairpin shape, attached to the coils of a tungsten filament and wicked onto the tungsten at moderate temperatures. After the aluminum is distributed on the filament it is allowed to cool.

The CH film is mounted in the bell-jar vacuum chamber and flushed with argon or dry nitrogen and then evacuated to a pressure of about 1 μTorr. The Al coated filament is heated to a temperature of 1500°–1700°C for ~20 seconds, which is sufficient time for the evaporation of the aluminum but not long enough to damage the CH film by IR radiative heating. The mass of the aluminum wire to be evaporated from the filament is set to provide the desired thickness of the layer deposited on the CH film. If lines of coated CH film are to be interlaced with uncoated areas, a mask is placed over the CH film to provide the appropriate pattern of coated and uncoated areas.

After the CH films are coated and characterized, they are removed from the silicon wafers, cut into strips and attached to standard NRL target mounts to serve as NIKE laser targets.

For further information, please contact Dr. C. Hendricks (WJSA)

5. CRYOGENIC SCIENCE AND TECHNOLOGY DEVELOPMENT

The OMEGA laser at the University of Rochester and the National Ignition Facility will need cryogenic targets. We spent considerable effort in support of the ICF labs in understanding and controlling the various solid fuel layering (smoothing) processes (for both D_2 and DT) and on the development of foam targets suitable for liquid layering.

5.1. CR/LL1 CRYOGENIC LAYERING DEVELOPMENT

A major effort was expended on CRLL1 during FY96 to prove the feasibility of IR heating and joule heating techniques for smoothing cryogenic hydrogen ice layers. We demonstrated "proof-of-principle" with both of these techniques. Using joule heating we have made layers smooth to 0.8 μm rms in a cylindrical geometry, as compared to native ß-layers that have been measured smooth to 2.9 μm rms in the same cylindrical geometry. If we remove effects due to the inhomogeneous E-field in our sample cell, we find that joule heating makes layers smooth to 0.26 μm rms for a surface heat flux of 1.33 mW/cm^2 (a typical value used in our experiment). This rms roughness scales inversely with heat flux. IR heating has produced D_2 layers smooth to 0.3 μm in a planar geometry with a volumetric heating rate of 800 mW/cm^3. Experiments on spherical geometries that closely resemble the UR/LLE cryogenic layering system are currently being assembled for both IR and joule heating.

5.1.1. SMOOTHING OF DT ICE BY ELECTRICAL HEATING OF THE SATURATED VAPOR

Introduction. When liquid DT freezes in an isothermal shell, it initially forms a very rough layer on the bottom of the container. Because the ice self-heats, due to radioactive decay of the tritium, with a volumetric rate, q_s, of 5.06×10^{-2} watts/cm^3, there are variations in the temperature of the surface of the ice as the film thickness varies. The thicker areas of the film are warmer and consequently have higher vapor pressures, so material tends to sublime away from these regions and recondense at the cooler areas. If the container is isothermal, this leads to an ice surface that conforms to the surface of the container [Refs. 5-1

through 5-3]. For pure DT, the rate at which the material migrates can be shown to be $R_{DT} = q_s/s\rho_s$ [Ref. 5-3], where s is the heat of sublimation (1550 Joules/mole), and ρ_s (5.18×10^{-2} mole/cm^3) is the density of the solid, with $1/R_{DT} \approx$ 27 minutes. This process is known as "beta-layering". β-layered DT ice surfaces have been characterized optically and found to have roughness in the range of 1.0–1.5 μm RMS for cylindrical layers approximately 100 μm thick and 2 mm in diameter. It is desirable to reduce this value to minimize the effects of mix during the implosion of an ICF capsule and increase the drive flexibility available to experimental designers [Ref. 5-4].

For wavelengths large compared to the surface thickness, h, the increase in surface temperature with increasing h drives the smoothing process. We expect that an increase in $dT(h)/dh$ should result in a smoother surface. One way to increase this quantity is to add an additional heat flux from the saturated vapor to the ice. This heat flux f_s, will increase $dT(h)/dh$ by f_s/k_s where k_s is the thermal conductivity of the ice. This increase will match that produced by the DT self heating when $f_s = q_s h$ or 5×10^{-4} watts/cm^2.

Electrical Conductivity of DT. Measurements of the electrical properties of DT gas have been made by Souers [Refs. 5-5, 5-6]. This data may be used to estimate the free electron density in DT gas with a density of 100 mole/m^3 to be 4×10^{13}/m^3 at 20 K. However, these measurements were done on the gas alone without the additional radiation load of the surrounding DT solid found in our experiment. Souers [Ref. 5-7] estimates the fraction of β-particle energy escaping from a surface layer of DT of areal density 1.4 moles/m^2 as 0.11. This is about five times the β-energy generated in the vapor of an ICF target. Since the free electrons are only about one percent of the charged particles in the gas [Refs. 5-5, 5-6], their recombination rate is approximately independent of density and we can estimate the free electron density in the gas as 2×10^{14}/m^3. The electron mobility μ_e can be estimated from electron mobilities measured in D_2 gas at 76.8 K [Refs. 5-7, 5-8]. For fields of 500 V/cm and densities of 100 moles/m^3 these give $\mu_e = 0.1$ m^2/V-s.

The power coupled into a gas volume by an electric field is:

$$P_{gas} = e n_e \mu_e V_g E^2 \tag{1}$$

where, E is the root-mean-squared electric field and e is the electron charge. To reach a heat flux equivalent to the bulk heat produced by DT in a 2.2 mm diameter target with a 0.1 mm thick ice layer requires $P_{gas} = shq_s = 63$ μW. The corresponding field is $E = 6.85 \times 10^2$ V/cm. Given the electron mobility above and the interior diameter of 2 mm, the electron

transit time through the DT gas space is about 0.3 μs. To avoid the loss of electrons as they drift into the DT ice, we work at a frequency much higher than (1/0.3) μs^{-1}. The desired field can be generated using a resonant cavity with reasonable rf power. For practical reasons, we choose to apply the field at about 1 GHz. Our experimental design allows us to generate these fields in a cryogenic microwave cavity surrounding a cell containing condensed DT.

Experimental Setup. The experimental design was fully described in our FY95 annual report [Ref. 5-9]. It should be noted that our design was overly conservative. We anticipated having to remove up to 10 watts of heat from our microwave cavity to be able to maintain its temperature at 20 K. This was required in order to generate 5000 V/cm in the sample cell, a value chosen based upon the conductivity of DT gas not surrounded by DT ice. As discussed in the previous section, the gas conductivity was much higher than we originally anticipated and therefore our required field was much lower.

We have generated a model for the average field inside our sample cell. This model includes the measured value of the microwave cavity Q to help reduce our calculation uncertainty. We calculate the field to be:

$$E_{cell} = \frac{(950 \pm 120)\ \text{volts}}{\text{cm}} \sqrt{\frac{P_{rf}}{\text{watts}}} \quad . \tag{2}$$

This formula reveals that it takes 1030 mW of rf power to generate an average field of 1000 V/cm inside the sample cell and that it only takes 519 mW of rf power to generate a heat flux equivalent to that of DT.

This result implies that future experiments will have much more modest cryogenic designs. The smaller power dissipation required makes the prospects of fielding a joule heating layering module for a cryogenic ICF target more encouraging.

Data Collection. The roughness of the DT ice surface is characterized optically. A long range microscope looks through windows in the cryostat and cavity, and is focused on the ring centered in the sapphire cell. Images are taken with a Photometrics camera using a Kodak KAF-1400 CCD array, and downloaded to a personal computer for analysis. Images are saved using a 1024 × 1024 subarray of pixels on the CCD. Each 6 μm CCD pixel corresponds to 2.15 μm at the focal plane. Raw images, such as that shown in Fig. 5-1, have a bright central region which makes a transition to a dark outer region where the ice surface blocks the light. Computerized image analysis is carried out on the raw image using a code

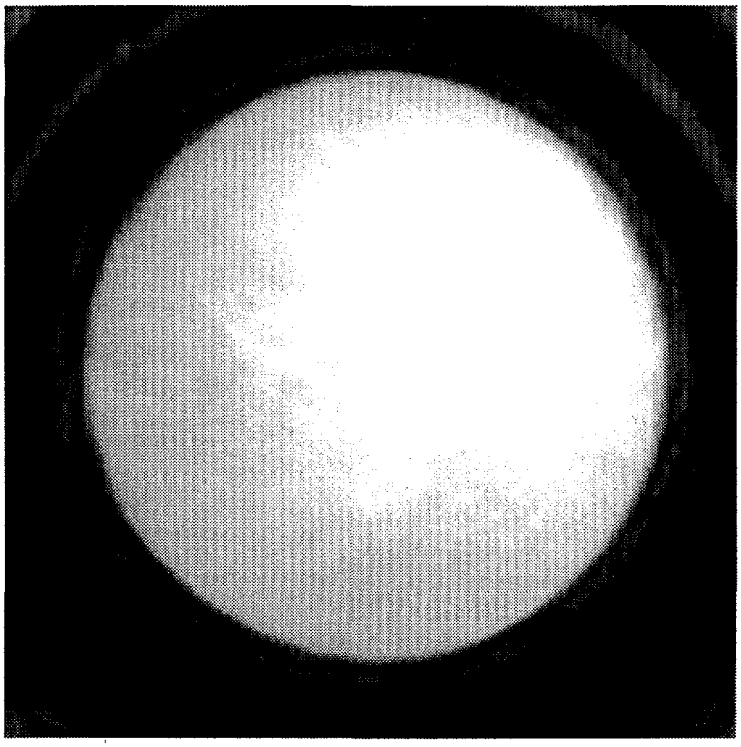

Fig. 5-1. DT ice layer before heating of the DT gas inside the cell.

developed by Evan Mapoles of LLNL. The end result is the rms roughness of the surface and a power spectrum of the surface fluctuations as a function of mode number.

Thermal Analysis. In order to calculate the effect of the rf power dissipation in the DT gas on the DT layering rate a one dimensional calculation has been done for the case shown in Fig. 5-2. It can be shown [Ref. 5-10] that the layering rate R is of the form

$$R = \left(\frac{q_s}{s\rho_s} + \frac{q_g h_g}{s h_s \rho_s}\right)\left\{\frac{h_g k_s}{s h_s D n}\left(\left.\frac{dn_{sv}(T)}{dT}\right|_{T=T_1}\right)^{-1} n_3 + 1\right\}^{-1} \tag{3}$$

where, q_S is the bulk heating in the solid, q_g is the heating in the gas, s is the heat of sublimation of the solid, n_{sv} is saturated vapor density of DT, D is the diffusivity of the gas, and n_3 is the density of ^{3}He. The first term in parenthesis is the result of bulk heating in the solid as has been shown in Ref. 5-3. The first term plus the term in braces has been previously derived in Ref. 5-11. The second term is new and describes the effect of the heating of the gas on the layering rate. For a fixed ^{3}He concentration we expect the layering rate to increase linearly with the power dissipated in the gas, which is proportional to the

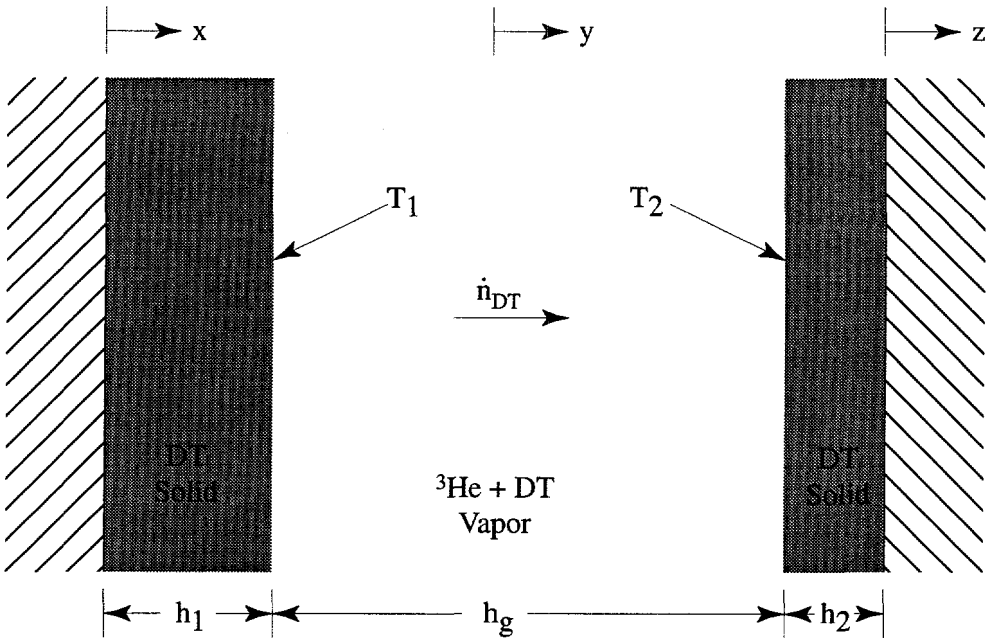

Fig. 5-2. Geometry and variables used in the analysis of the layering rate.

power dissipated in the cavity. Since the average heat flux generated at the DT ice surface f_s is

$$\frac{q_g h_g}{2}$$

in the planar case, the rate induced by the rf heating can be expressed as:

$$R_{rf} = \frac{2f_s}{sh_s\rho_s}\left\{\frac{h_g k_s}{sh_s Dn}\left(\frac{dn_{sv}}{dT}\bigg|_{T_1}\right)^{-1} n_3 + 1\right\}^{-1} . \tag{4}$$

Since this expression is independent of geometry, except for the effects of ^{3}He, it should remain valid in our roughly cylindrical geometry. Since heat flux through the surface is proportional to the square of the electric field, which is proportional to the power into the cavity, we find that the layering rate is proportional to the power into the cavity for a fixed temperature and ^{3}He concentration.

Experimental Results. In order to evaluate the coupling of the electric field to the gas we first measure the rate at which freshly frozen liquid in the cell forms a uniform layer as a function of rf power into the cavity. At each rf power value we allow the ice to evolve into a uniform layer, photographing the layer in the cell at regular intervals. Each photo is analyzed

and the decay of the second mode is fit to an exponential. The fit coefficient of the exponential is then taken as the layering rate at that power.

In order to calculate the heat flux generated by the electric field, we first need to evaluate the effect of the factor in braces in Eq. (4), which depends on the ^{3}He content of the vapor. To do this, we fit the observed layering rates to a model of the form:

$$R(P_{rf}, t) = \frac{aP_{rf} + c}{bt + 1} \tag{5}$$

where, P_{rf} is the rf power into the cavity, t is the age of the DT computed from the elapsed time from the fill of the cell, and a, b, and c are fit parameters. We multiply the rates by bt + 1 and plot the result in Fig. 5-3. These age corrected rates are proportional to the power into the cavity.

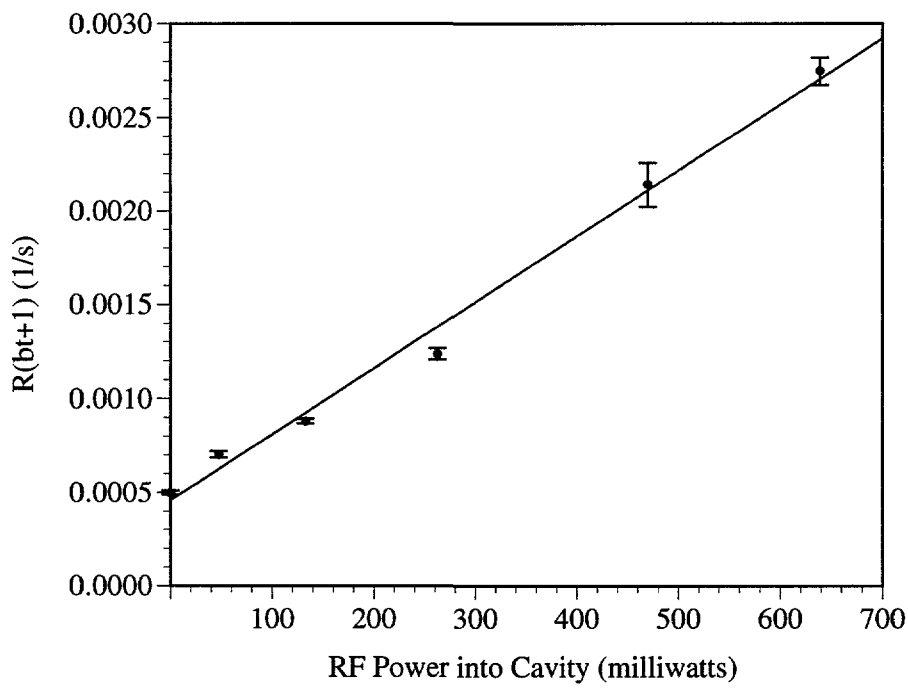

Fig. 5-3. Layering rates corrected for DT age vs. rf power applied to the cavity.

We find $c = (4.5 \pm 0.7) \times 10^{-4}\ s^{-1}$ and $a = (3.5 \pm 0.3) \times 10^{-3}\ s^{-1} \bullet watts^{-1}$. The reciprocal of *c* is just the time required to form a β-layer with no ^{3}He and no rf power. Our value of *c* gives 36 ± 6 minutes which is consistent with existing data for DT [Refs. 5-3 and 5-11]. The slope a can be used to calculate the heat flux produced and therefore the electrical conductivity of the gas. We have $aP_{rf} = f_s/sh'_s\rho_s$ or:

$$f_s = ash'_s\rho_s P_{rf} = (2.65 \pm 0.27)x10^{-3} \text{watts/cm}^2 \left(\frac{P_{rf}}{\text{watts}}\right) \quad . \tag{6}$$

Using Eq. (1) and Eq. (3):

$$\sigma_g \equiv en_e\mu_e = \frac{ash'_s\rho_s}{(V_g/S)}\left(\frac{950 \text{ volts}}{\text{cm}}\right)^{-2} \text{watts} \quad . \tag{7}$$

The volume to surface ratio for our cell is $\left(V_g/S\right) = 3.7 \times 10^{-2}$ cm, however, from Ref. 5-9, the field within the cell is non-uniform and consequently the heat flux at the DT ice surface is also anisotropic. This leads to uncertainty in $\left(V_g/S\right)$, since more or less heat may flow through the surface of interest than the average over the cell. If the ring were part of a spherical surface we would have $\left(V_g/S\right) = 3.3 \times 10^{-2}$ cm, and if it were part of a cylinder of length 2 mm, we would have $\left(V_g/S\right) = 5.0 \times 10^{-2}$ cm. Averaging these possibilities we have $\left(V_g/S\right) = (4.0 \pm 0.9) \times 10^{-2}$ cm. The layer thickness $h'_s = 94.4 \pm 5.1$ μm. Using these we find:

$$\sigma_g = (7.3 \pm 2.8)x10^{-6}(\Omega - m)^{-1} \quad . \tag{8}$$

This is consistent with the numbers quoted previously in the electrical conductivity section for the electron density and mobility in the gas.

When rf power is applied to the cavity, there is a rapid apparent smoothing of the ice surface as seen by comparing Fig. 5-4 with Fig. 5-1. The photograph of Fig. 5-4 was taken after applying 315 milliwatts of rf power to the cavity for 500 seconds. This reduction is also made apparent in Fig. 5-5 by comparing the power spectra of the surfaces before and after applying the rf. The heat flux treated surface is smoother at all wavelengths, but the magnitude of the improvement increases at higher frequencies. Above mode 50, the rf heated surface reaches the noise level of the detection system. The lower smoothing rate at low frequencies is expected since the sample cell electric field [Ref. 5-9] has a substantial non-uniform component. This anisotropy also complicates the analysis of the rate of improvement of the surface with rf power. As the rf field is increased, the field anisotropy induces low frequency perturbations in the ice surface even as the higher frequencies are smoothed.

We define S_n as the RMS roughness of the surface due to modes n and higher, so that:

$$S_n = \sqrt{\sum_{k=n}^{k=128} P_n} \tag{9}$$

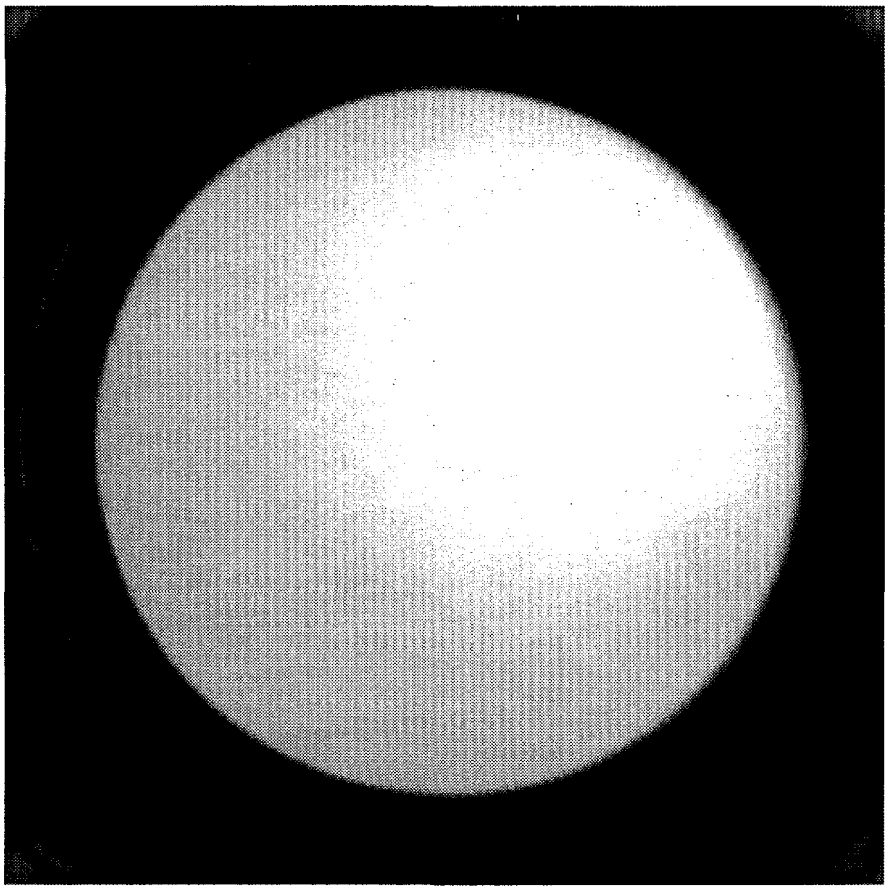

Fig. 5-4. DT ice layer after rf heating of the DT gas in the cell.

where, P_n is the power in mode n. Figure 5-6 shows S_n as a function of rf power for several low values of n. As the rf power is increased, S_n initially falls but then increases as low frequency surface perturbations grow. The rate of increase falls with increasing n since the power spectrum of the electric field near the DT surface also falls rapidly with increasing n. S_n is fitted to a trial function of the form:

$$S_n = a_n P_{rf} + b_n / P_{rf} \tag{10}$$

where, the first term represents the roughness introduced by the field anisotropy and the second represents the smoothing by the heat flux. The a_n's decrease approximately as 1/n and the b_n's scale approximately as $(0.13\mu m - \text{watts})n^{-1/2}/P_{rf}$. If we imagine an experiment in which a perfectly uniform field is applied, we would consider only the effect of the b_n's. Then since the length of the DT surface, $L_n = 2\pi(1\text{mm})/n$, we express the expected RMS roughness of the heated surface using Eq. (10) as:

$$S_1 \approx \frac{0.14\,\mu\text{m}}{(f_s\,/\,\text{milliwatts}/\text{cm}^2)}\sqrt{\frac{L_1}{\text{mm}}} \quad . \tag{11}$$

For further information, please contact Dr. J. Sater (WJSA).

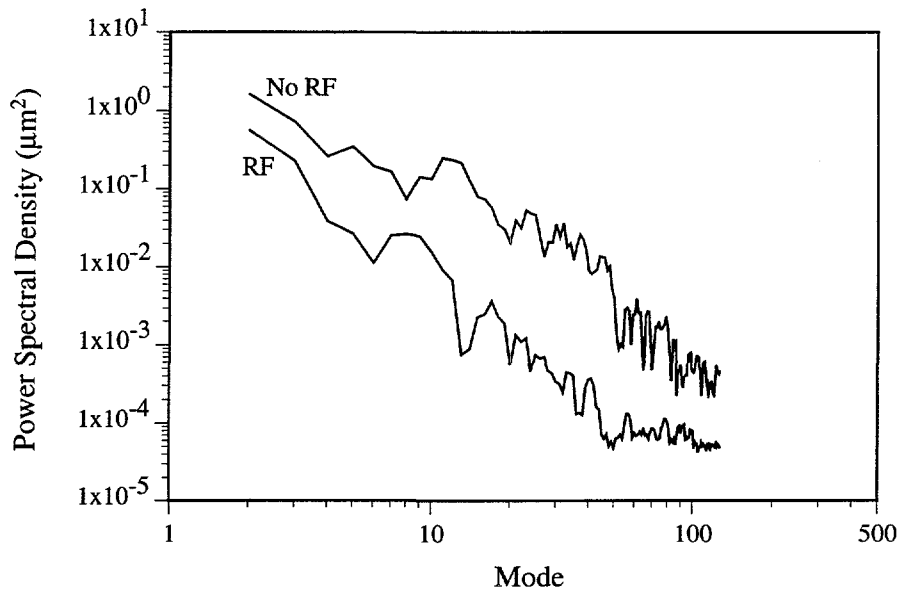

Fig. 5-5. Comparison of the power spectra of the DT ice surface before and after heating.

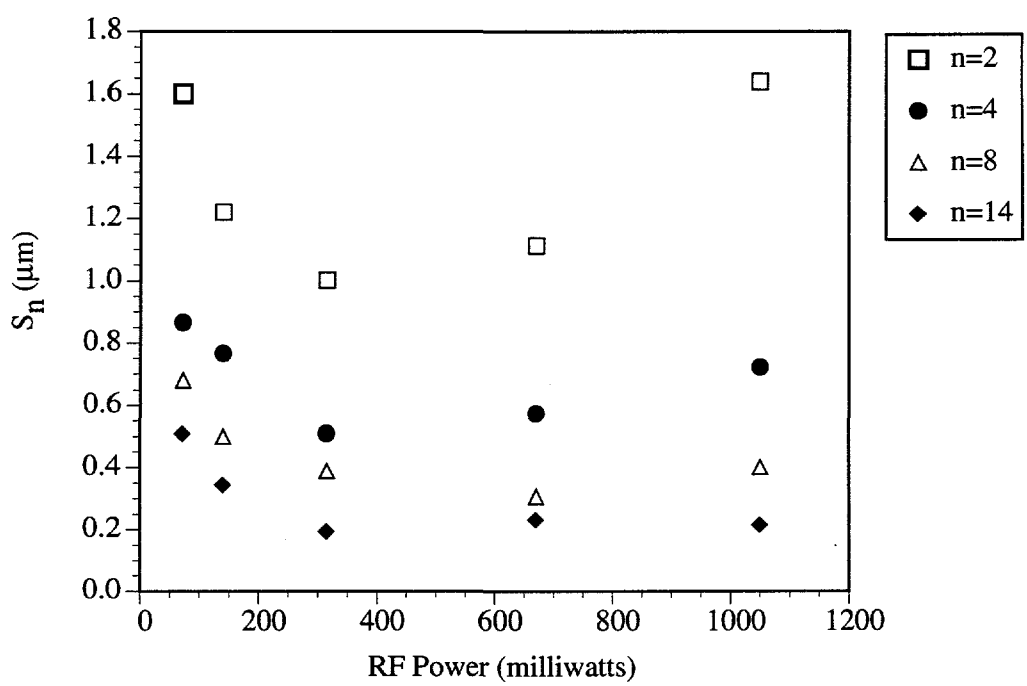

Fig. 5-6. S_n vs. rf power for several n.

5.1.2. IR HEATING SURFACE ROUGHNESS EXPERIMENTS

Current cryogenic target designs require a uniform cryogenic DT fuel layer. There is also a need for nontritiated cryogenic targets, HD or D_2. However, without the β-decay heat generation, no solid redistribution will occur. We are continuing to investigate the possible use of infra-red (IR) radiation to redistribute solid D_2 or HD inside suitable plastic shells by pumping the collision-induced vibration-rotation bands characteristic of the hydrogens [Refs. 5-12 and 5-13]. FY95 experiments involved measuring mass redistribution time constants. FY96 experiments focused on determining the surface roughness of the resultant IR illuminated layer.

Figure 5-7 contains a sketch of the experimental layout. For these experiments a sample cell containing HD or D_2 was illuminated from below by an IR laser beam. The sample cell consisted of a 6 mm sapphire cube with a 5 mm diameter cylindrical hole, a sapphire window at the bottom and an infrasil window at the top of the cell. The hydrogen fill tube was glued into a 381 μm diameter hole in the side of the sapphire cube. The cell was thermally and mechanically attached to the cold tip of a helium flow cryostat. An F-center laser produced the IR light. Layers were formed by two methods. In one case, liquid was condensed in the cell and subsequently frozen. The IR beam was turned on, and the solid redistributed around inside the cell forming a thin layer on the bottom window. For the other method, the solid HD or D_2 coating the bottom window was allowed to evaporate off. Upon turning on the IR, solid again redistributed itself inside the cell, coating the bottom window by vapor deposition. A white light interferometer was used to measure the surface roughness of these layers. In addition, the time development of these layers evolving on the bottom window was viewed and recorded through the side of the cell.

The high spatial coherence of the IR beam presented illumination uniformity problems. To reduce spatial coherence effects in the illumination field and thus smooth the beam, two counter-rotating diffusers were placed in the beam path just before the IR beam entered the cryostat. The diffusers reduced coherence-induced intensity perturbations by introducing speckle into the illumination field. The speckle was then averaged out by rotating the diffusers. Figure 5-8 shows optical path depth interferograms of an HD layer illuminated with IR without beam smoothing and after the beam is smoothed with two rotating diffusers. The bull's-eye pattern seen in the smooth layer results from the gaussian curvature in the

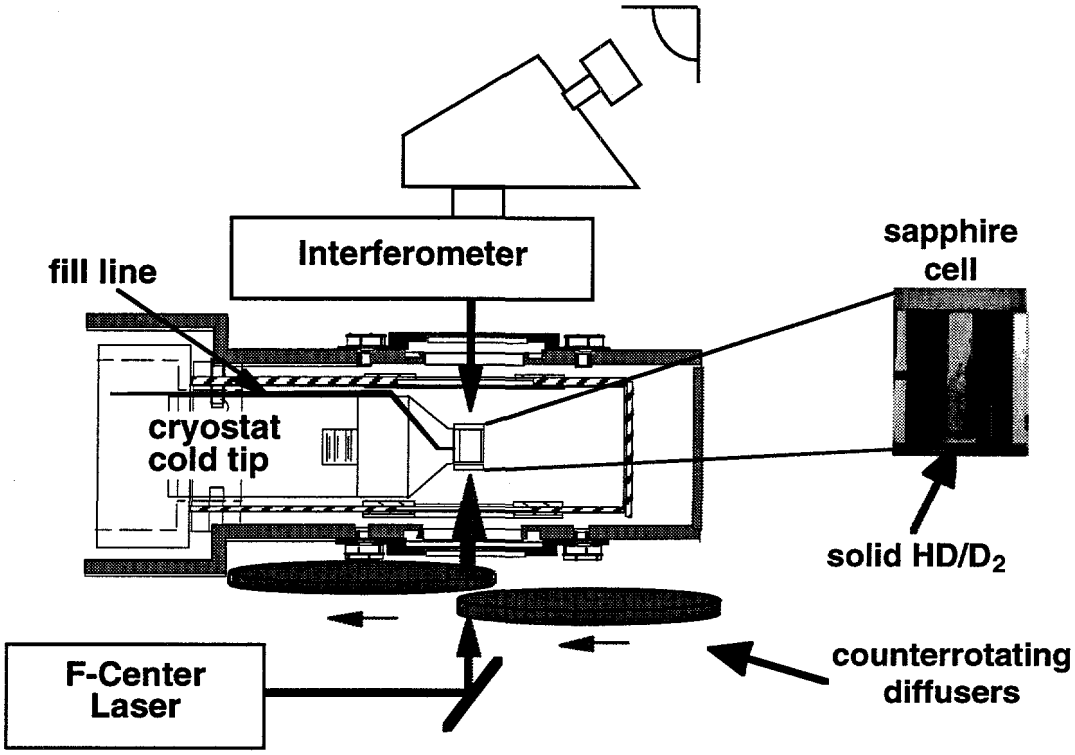

Fig. 5-7. Sketch of the experimental layout.

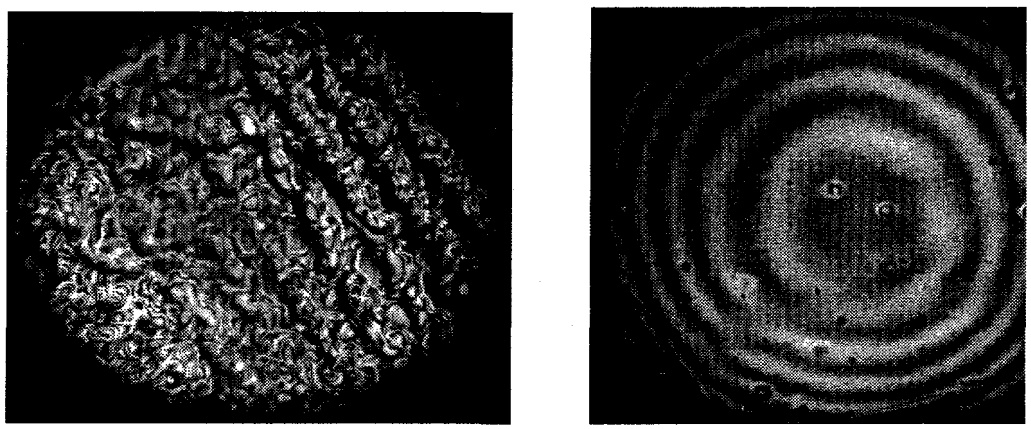

Fig. 5-8. Optical path depth interferograms of HD layers formed by ~50 mW of non-smoothed (left) and smoothed (right) 2.57 μm radiation.

smoothed IR beam causing a gaussian layer curvature. This process of beam-layer smoothing also suggests that the solid can be significantly modified by shaping the incident illumination field.

Hydrogen surfaces can be smoothed by both surface heat flux and bulk heating. Figure 5-9 shows the surface roughness rms versus the bulk heating rate from IR illumination, Q_{IR}, after removing the gaussian layer curvature. The scale length for these rms measurements is 3 μm. The surface roughness decreases with increasing Q_{IR} to values well below the NIF (National Ignition Facility) specification. The ability to smooth the interface, with either bulk heating or surface heat flux, is proportional to the increase in surface temperature with increasing layer thickness, $\delta T/\delta h$. In the case of bulk heating, $\delta T/\delta h \approx Qh/\kappa$, where κ is the thermal conductivity of the solid, Q is the bulk heating generation rate, and h is the layer thickness. For surface heating, $\delta T/\delta h \approx F/\kappa$, where F is the surface heat flux. The solid line in Fig. 5-9 shows a best fit to surfaces smoothed by a surface heat flux. We plot the surface heat flux data by setting $F = Q_{IR}h$ with $Q_{IR} \approx \alpha I$, where α is the absorption coefficient and I is the IR flux incident on the layer. At our highest

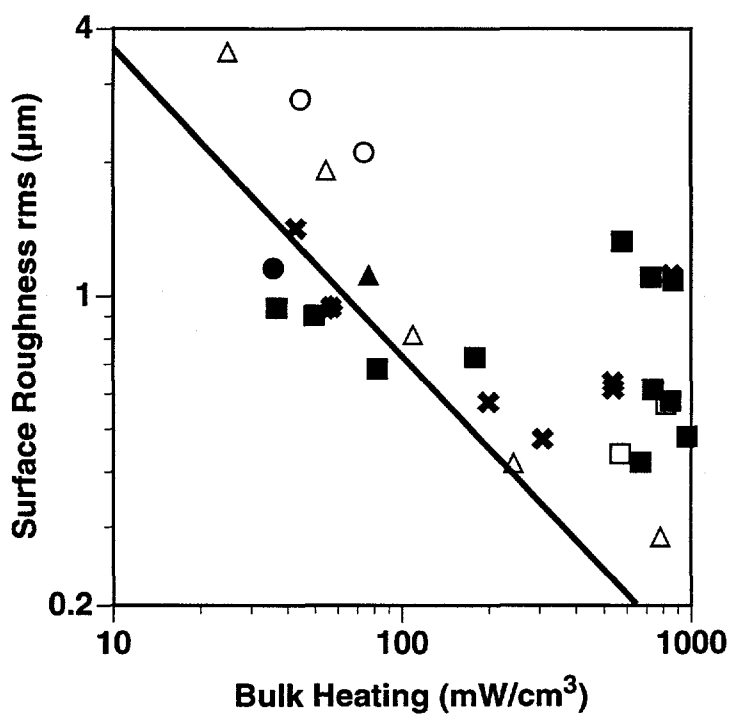

Fig. 5-9. Surface roughness decreases as the heating rate increases to 400 mW/cm^3. The solid line (▬) corresponds to heat flux (Q=F/h). The data are from experiments with the corresponding layer thickness and temperature: (✖) 100 μm at 16.4 K, (O) 170 μm at 16 K, (■) 100 μm at 16 K, (△) 60 μm at 16 K. The native beta layering surface roughness for a 80 μm thick D-T layer is also shown (●) for comparison

heat flux values, we have measured a surface roughness, σ, as low as 0.3 μm rms. This heat flux is about 20 times that for DT ($Q_{IR} \approx 20\ Q_{DT}$) and corresponds to about $0.3\sigma_{DT}$. However, crystal growth has a significant impact on the measurements. Crystals can produce significant surface roughness even at our largest heating rates.

IR-smoothed D_2 layers have a similar spectral shape to DT (Fig. 5-10). However, as the heating rate was increased from 35 mW/cm^3 to 319 mW/cm^3 for the D_2 layers, the overall surface roughness decreased substantially with the smoothing effect at low frequencies (long wavelength) being significantly greater than at higher frequencies. At the higher IR-heating rates, the surface smoothness of the D_2 sample was better than the native beta-layered DT sample.

For further information, please contact Dr. D. Bittner (WJSA).

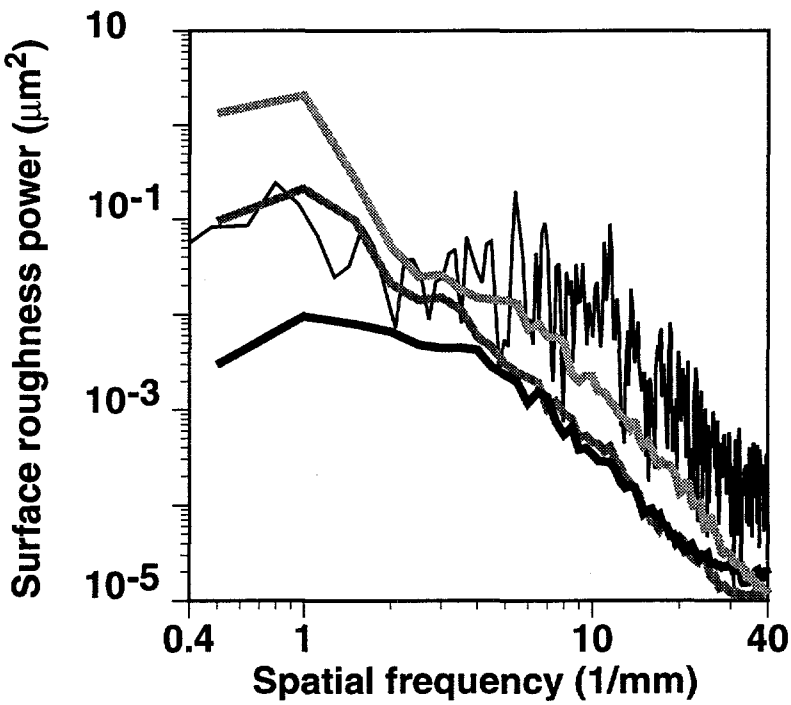

Fig. 5-10. IR smoothed layers (Q=35 mW/cm^3, h=80 μm, Q=40 mW/cm^3, h=70 μm, Q=319 mW/cm^3, h=70 μm) have a similar spectral shape to D-T (—Q=50 mW/cm^3, h=80 μm). IR heating has a much larger smoothing effect on the surface at low frequencies than at high frequencies.

5.1.3. MODELING OF SURFACE ROUGHNESS FOR IR HEATING

To determine our ability to reduce DT or D_2 surface roughness with IR light, we calculate the temperature gradient $\delta T/\delta h$. This is the quantity that causes ß-layering and also smoothes surfaces in the heat flux experiments. Both IR (bulk) heating and surface heat flux can generate a $\delta T/\delta h$, but they are not equivalent. While surface heat flux smoothes a surface at all spatial wavelengths, there is a wavelength dependence for bulk heating.

A thermal modeling effort investigated the surface temperature fluctuations resulting from small sinusoidal thickness deviations in a DT layer. A COSMOS model was constructed of a layer of thickness h with a sinusoidal surface perturbation δh. The thermal gradient was calculated for perturbation wavelengths down to 25 μm with the sensitivity decreasing dramatically as the wavelength decreases. The frequency was calculated by dividing the mean thickness of the layer by the wavelength of the sinusoidal thickness deviation. A range of perturbation amplitudes was also investigated at each of several frequencies with minimal effect on $\delta T/\delta h$.

From computer modeling we find:

$$\frac{\delta T}{\delta h} = \frac{Qh/\kappa}{\left(1+\left(\frac{2\pi h}{\lambda}\right)^2\right)^{1/2}}$$

where, λ is the wavelength of the surface perturbation. In the long wavelength limit $\delta T/\delta h = Qh/\kappa$, where $Q \approx \alpha I$ is the bulk heat generation rate from IR illumination, α is the absorption coefficient, I is the IR flux incident on the layer, h is the layer thickness, and κ is the thermal conductivity. Computational results presented in Fig. 5-11 show that a surface heat flux (dashed line) is more efficient in smoothing high frequency surface perturbations than is bulk IR heating.

For further information, please contact E. Monsler (WJSA).

5.1.4. MODELING OF IR ILLUMINATION SCHEMES INSIDE A HOHLRAUM

If smoothing by IR heating is to be performed in a target shell, the illumination must be uniform. A model of the light propagation inside a hohlraum will allow the problem to be investigated. An initial concept is to use the cylindrical wall of the hohlraum as a diffuse

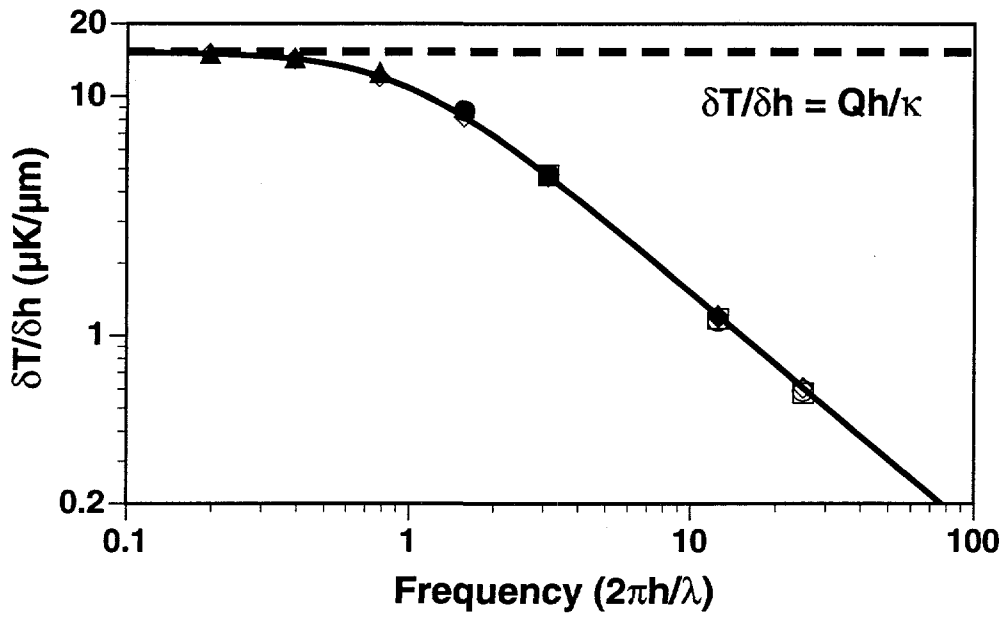

Fig. 5-11. Temperature gradient (dT/dh) for a 100 μm thick layer with various sinusoid amplitudes (△ 4μm, ◇ 2μm, □ 1μm, ■ 0.5μm,. and ○ 0.25μm).

reflector (similar to an integrating sphere) and shine IR in through the end windows onto the wall. The best way to simulate this is with Monte-Carlo methods and raytracing code.

A code written at LLNL called MONTE was used for these calculations. What can be calculated by MONTE is the exchange factor from any tile surface to any other tile surface, among a set of surfaces comprising an enclosure. It cannot consider multiple media nor the behavior of photons passing from one medium to another. Thus, calculations cannot determine if the photons entering the shell enter the solid ice layer. However, under a range of possible shell thicknesses and radii, all photons entering the shell should enter the ice. At this point, we assume that if the shell surface is uniformly illuminated, the ice will be as well.

The geometry of the enclosure is shown in Fig. 5-12. The walls of the hohlraum are considered to be 96% diffusely reflecting, and 4% absorbing. There are two planes of symmetry, each 99.99999% specularly reflecting. The shell and window surfaces are taken to have an index of refraction of 1.6, and to specularly reflect based on the incoming angle of the light. The "pole" of the shell is considered to be the point nearest the window, on the axis of symmetry.

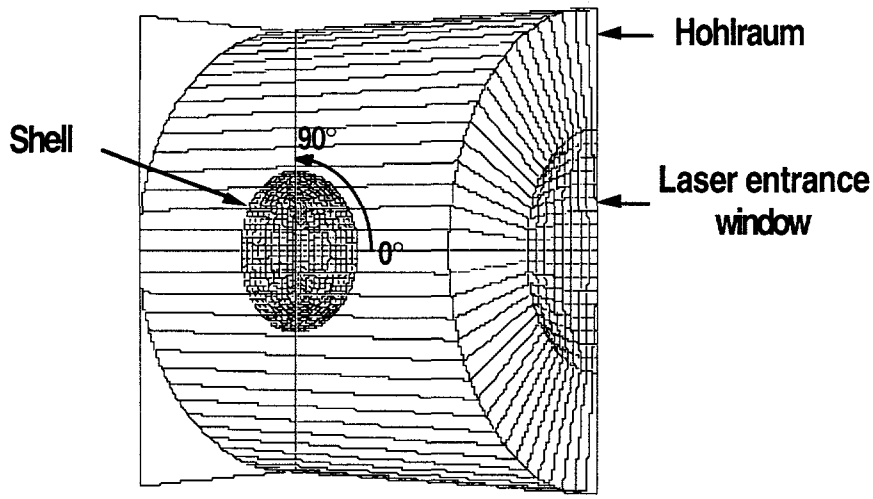

Fig. 5-12. Geometry of the tiled enclosure comprising 1/4 of hohlraum.

The results of the calculations, for the central three emitting regions of the window, are shown in Fig. 5-13. All three curves show increased intensity on the portion of the shell nearest the emitting region, as well as a general decrease in intensity from pole to equator. The general pole to equator decrease indicates that no combination of diffuse intensities from the window will generate uniform illumination. Therefore, other illumination schemes were considered, such as beams shining from the window regions toward the wall of the hohlraum. The intensity on the shell due to one of these beams, directed at the equator of the hohlraum, is also shown in Fig. 5-14. This figure depicts the resultant relative intensity calculated by taking a simple linear combination of intensity distributions. The intensity is uniform to within approximately 1.5%. This is a non-optimized calculation but it does indicate that it should be possible to generate uniform illumination on a capsule inside a hohlraum using IR illumination.

For further information, please contact E. Monsler (WJSA).

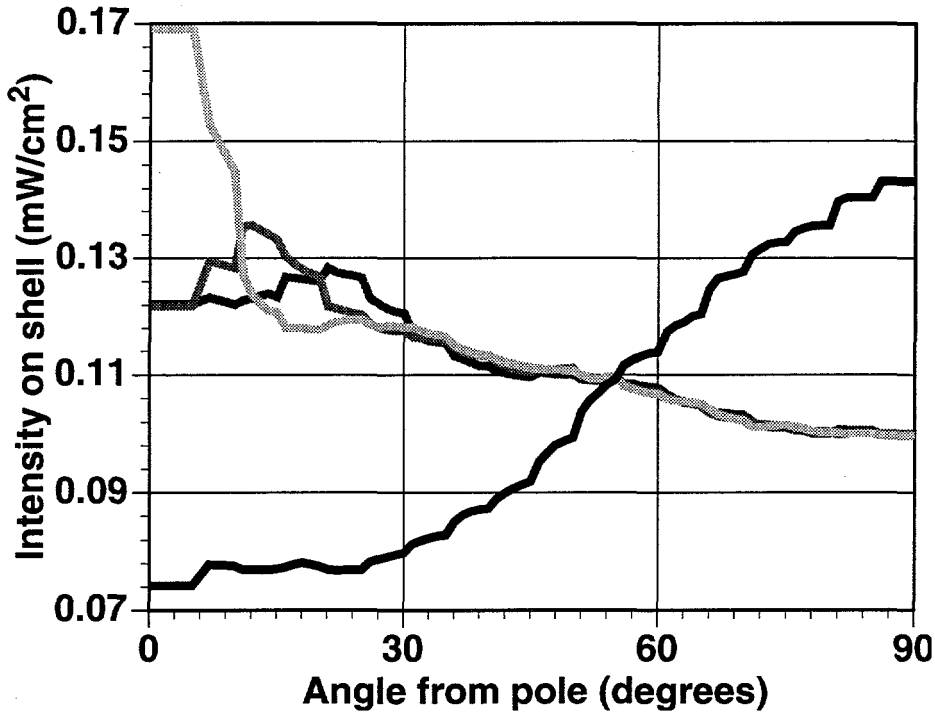

Fig. 5-13. Intensity entering the shell due to equal power emitted from various regions (0.333mm<r<0.5mm, 0.167mm<r<0.333mm, Central disc, r<0.5mm, Beam at equator)

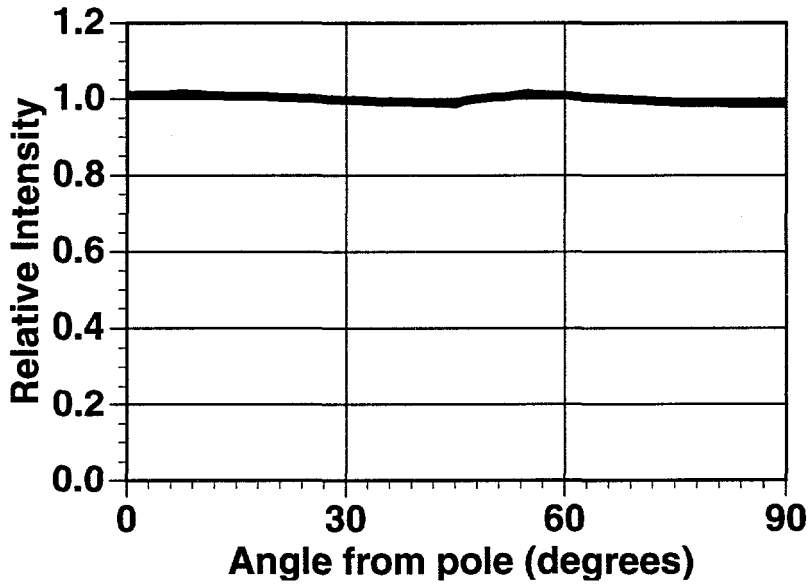

Fig. 5-14. Linear combination of intensity distributions

5.2. BETA LAYERING SUPPORT AT LANL

The FY96 beta-layering work at LANL included both D_2 and DT solid layering experiments in 2 mm toroidal cells using an internal heater for solid layer smoothing. Two separate 2 mm toroidal cells of the same type and configuration were used in these experiments, with the newer cell modified to reduce dead volume and allow individual temperature control of the layering cell and D_2/DT fill line. We used these cells to measure D_2 and DT solid surface RMS roughness and layering rate constants. The two toruses were designed to minimize the "light piping" effect observed in earlier 1 mm torus experiments where it was found that light transmitted by the solid layer dramatically reduced layer edge contrast, making it difficult to accurately define edges and thereby surface roughness. Further, the cell contains an axial heater to allow solid D_2 and DT layering and smoothing.

The first series of FY96 experiments involved the measurement of RMS surface roughness for "heat-assisted" and beta-layered solid DT. Figure 5-15 shows surface roughness evolution for (1) beta-layering at 19.65 K, (2) temperature decremented DT solid layering, and (3) 1125 μw heat-assisted DT layering. Temperature decrementing means that the temperature is reduced in steps as compared to temperature incrementing in which the

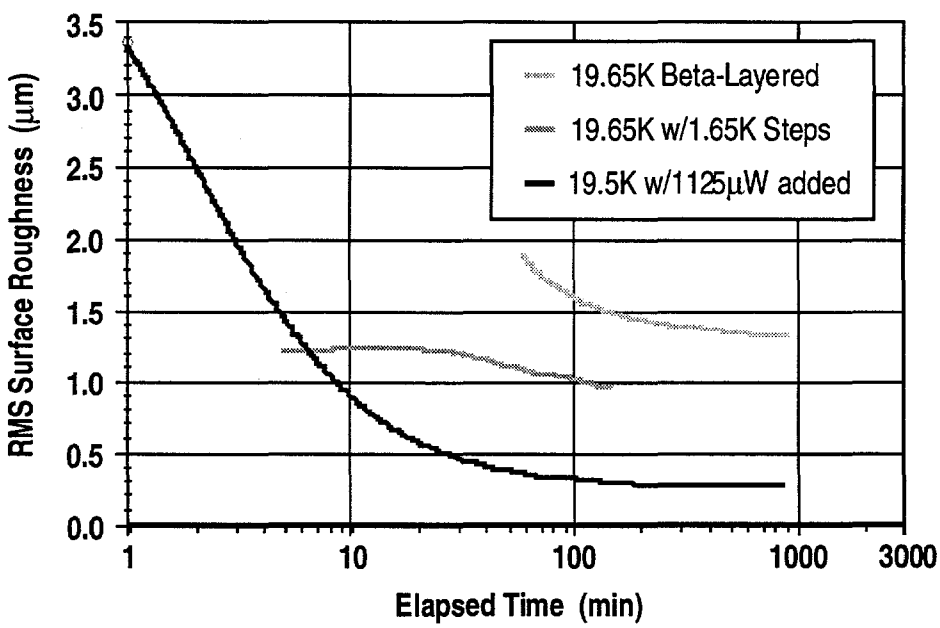

Fig. 5-15. Surface roughness evolution for native beta-layered DT solid layers at 19.65 K and 18 K, and for a DT solid layer smoothed with 1.125 mW heater power. The 19.65 K surface is very close to the DT triple point of 19.79 K, and could be somewhat unstable, causing the high value of surface roughness shown.

temperature is raised in steps. The temperature decrementing experiment was performed after equilibration of the solid DT at 19.65 K, a temperature which may have been too warm for the layer to maintain its integrity, causing the relatively large surface roughness shown. Figure 5-16 shows the surface roughness evolution for beta-layered DT solid, equilibrated at 19.0 and 19.5 K. This graph illustrates both the effects of equilibration temperature and layer thickness on surface roughness and roughness evolution. For example, at 19.0 K the 130 μm thick layer degrades much faster than the 80 μm layer, as a likely result of the larger helium buildup in the 130 μm layer.

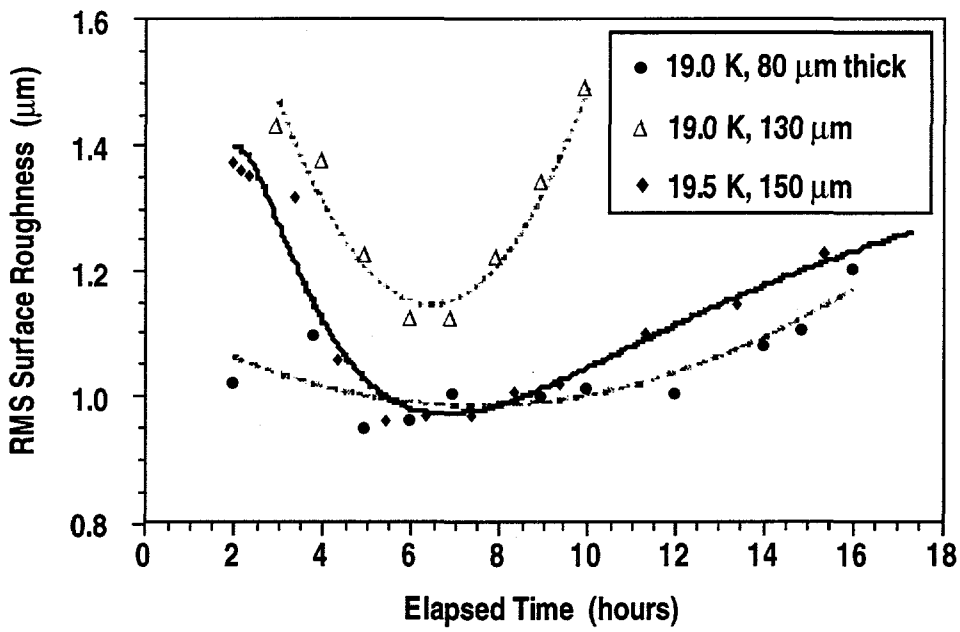

Fig. 5-16. Time evolution for DT solid surface roughness at 19 K and 19.5 K, for 80 μm and 130 μm solid layer thicknesses for native (no external heating) beta-layering. This graph shows the solid DT thickness dependence of RMS surface roughness, as well as equilibration temperature effects.

The next series of experiments were performed after the initial toroidal cell had been replaced by the second torus that had the same geometry and internal characteristics, but had reduced dead volume and the cell thermally insulated from the cryostat cold plate to allow individual temperature control of the toroid and the D_2/DT fill line. This feature allowed us to melt the solid layer in the cell, while the solid in the fill line remained frozen, thereby keeping the amount of material in the cell constant from run to run. The experiments performed thus far in this new cell have been restricted to D_2 solid layering studies, but with

a large variety and number of experiments to examine statistical behavior, and several solid layer processes. There were essentially four separate classes of D_2 layering experiments, each defined by the initial and final conditions.

The first class of experiments is described as "freeze-thaw cycling," in which an equilibrated (smoothed) D_2 solid layer is melted, then refrozen and allowed to re-equilibrate at a specific temperature and heater power. The process is then repeated for 12–24 cycles to gather statistics on the process. Results from one such experiment are shown in Fig. 5-17, with the equilibration performed at 18 K and 0.5 mW heater power. This graph shows D_2 layering to be a stochastic process, as the layer begins as an entirely new layer each cycle. The D_2 initial condition here is refrozen liquid, and the final condition is the re-equilibrated layer. DT layering experiments are to be started in FY97.

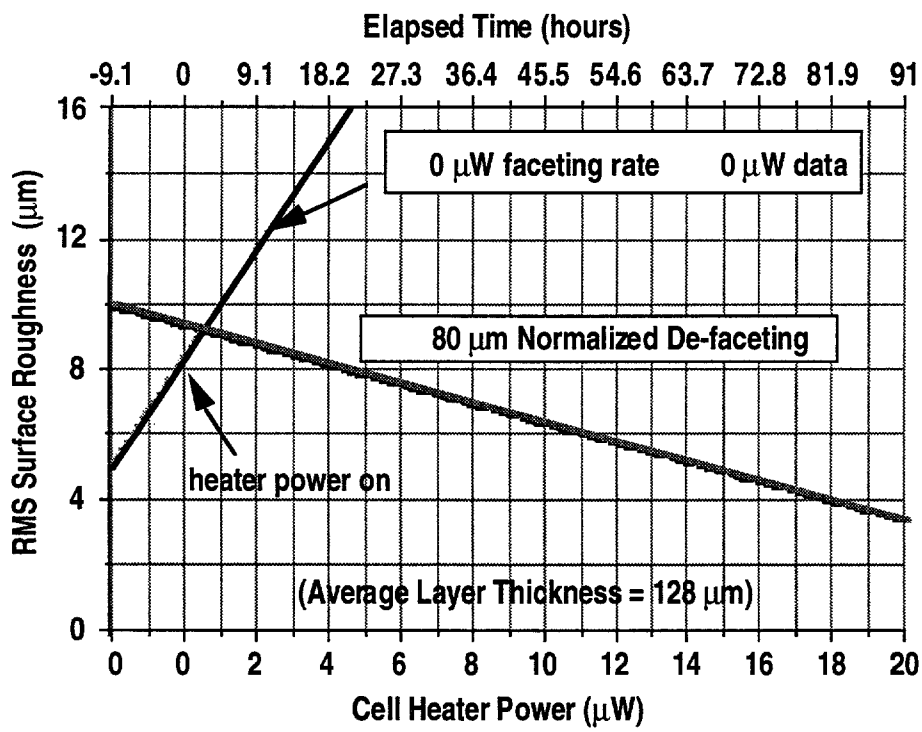

Fig. 5-17. D_2 solid layer freeze/thaw cycling at 0.5 mW heater power and 18 K equilibration temperature. An equilibrated D_2 solid layer is first melted, then re-frozen and then smoothed at 0.5 mW for a period estimated to be long enough for layer equilibration. Four equally spaced images are then acquired and the process repeated over 12 cycles. Since each re-freeze produces a slightly different layer, the process is stochastic which produces the data scatter shown.

The next class of experiments is one in which an equilibrated layer is allowed to facet (roughen) at a specific heater power and cell temperature, for a specific amount of time. The process is then reversed and the layer is re-smoothed at a given heater power until fully equilibrated. One such experiment is shown in Fig. 5-18. In this figure the layer is faceted at zero power, and smoothed at 2.0, 1.0, 0.5, and 0.25 mW. A number of such experiments were performed, at a variety of faceting and smoothing powers, then data for the final equilibrated RMS roughness gathered. The initial conditions for these experiments are the faceted D_2 solid layer, and the final conditions are the fully equilibrated (smoothed) D_2 solid layer.

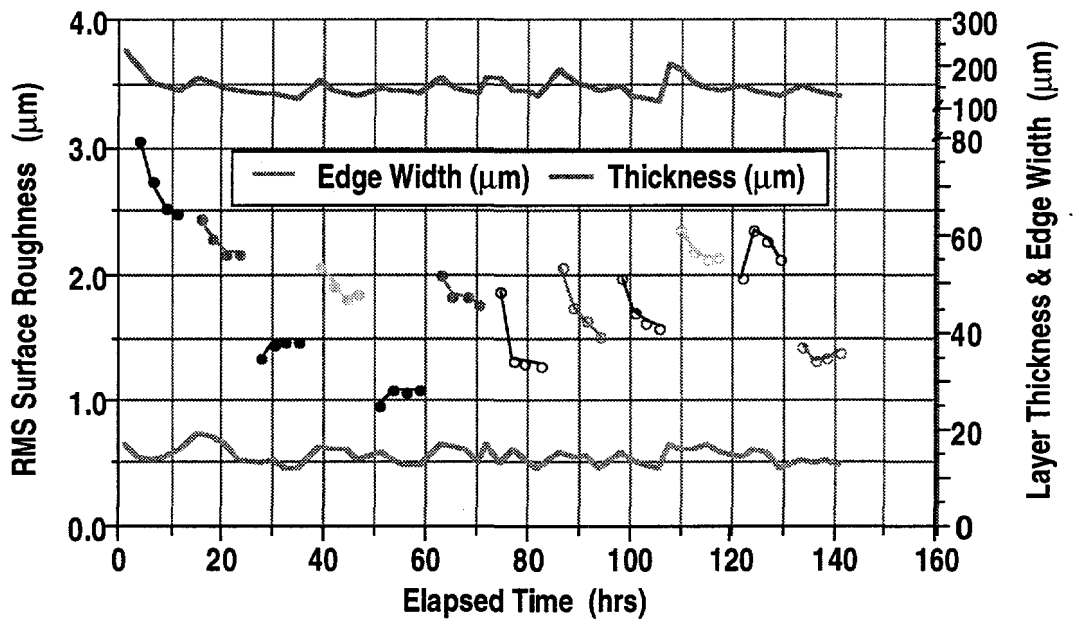

Fig. 5-18. D_2 solid layer facet/smooth cycling at 18 K, zero faceting power and smoothing powers from 2.0 mW to 0.25 mW. The layer is allowed to facet at zero power for about 7 hrs, after which the cell heater is energized at 2.0 mW until the layer equilibrates. The process in repeated with heater powers decremented to 1.0, 0.5, and 0.25 mW during the smoothing cycle.

The third class of experiments performed were those called "equilibration power stepping," in which an initially roughened layer was progressively smoothed with increasing amounts of heater power, then allowed to progressively roughen with decreasing amounts of heater power. The fully equilibrated solid layer roughness was then measured. Figure 5-19 shows the results of such an experiment, in which a fresh layer was allowed to roughen at zero power for a period of time, then smoothed at 0.25, 0.5, 1.0, and 2.0 mW, then roughened at 1.0, 0.5, and 0.25 mW. The initial conditions here are the previously equilibrated D_2 solid

layer, prior to the application of the next power step, and the final conditions are the equilibrated layer after the application of the next power step.

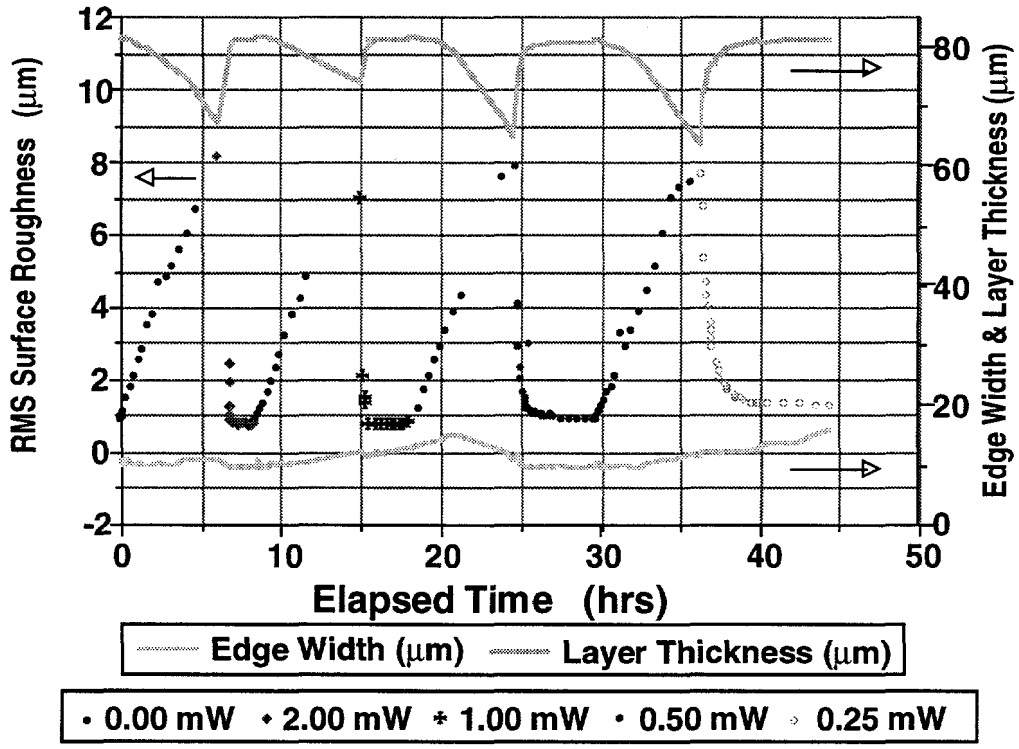

Fig. 5-19. D_2 Solid layer equilibration power stepping at 18 K. A D_2 solid layer is first melted, re-frozen, then allowed to equilibrate at 0.1 mW heater power. The power is then incremented in steps to 0.25, 0.5, 1.0, and 2.0 mW, with the layer being allowed to equilibrate during each step. After the 2.0 mW equilibration step, the power is decremented in the same manner. This graph shows the RMS surface roughness dependence on heater power, and a hysteresis effect during power decrementing.

The final class of experiments consisted of faceting (roughening) the D_2 solid layer at zero power for a specific amount of time at 18 K, then turning on the heater power at a very low level (2 μW), then stepping the power up to 18 μW in 2 μW increments at equal time intervals. This experiment allowed us to observe that actual smoothing begins at a very low power (≤2 μW) and progresses as the power is incremented. Figure 5-20 shows this experiment, with the initial dotted line representing the probable zero power faceting track (based on another experiment), with the power turned on at 2 μw, then incremented at equal time intervals to 18 μW. The initial conditions in this experiment were the zero power faceted D_2 layer after about 12 hours, and the final conditions were the RMS roughness 9.1 hours after the application of the next power increment.

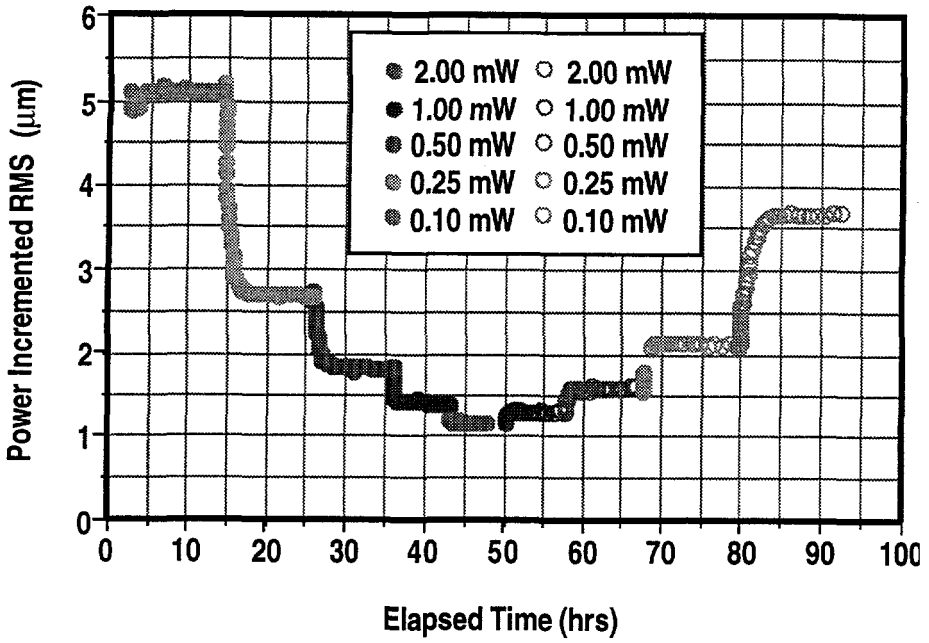

Fig. 5-20. Low power de-faceting (smoothing) of a D_2 solid layer surface at 18 K. First, a D_2 solid layer is melted and re-frozen at 18 K, then allowed to facet at zero power for about 12 hours (the dotted line shows the faceting path using data from a previous experiment). The upper x-axis shows elapsed time, with time zero being the moment heater power is turned on, and the lower x-axis shows the heater power at those times. At time zero the heater power is turned on at 2 μW and equilibrated for 9.1 hours. At each 9.1 hour interval the heater power is incremented by 2 μW up to a total of 18 μW. This graph shows that very low power is needed (2 μW) to turn faceting (roughening) into smoothing.

For further information, please contact J. Sheliak (GA)

5.3. IR LAYERING SPHERE

In all the techniques which add heat to enhance DT ice layering, uniformity of heat distribution is critical. For IR heating, it is difficult to compensate for the redistribution of the incoming light because of refraction and reflection of the incident radiation. We have done computer modeling to evaluate the potential of putting the cryotarget inside an integrating sphere (a highly reflecting, but non-specular cavity) so that every point on the surface receives the same intensity and distribution of incident light, if not for the light entrance, inspection, and support ports in the sphere wall which spoil the uniformity of the illumination.

Because the shell causes a tiny perturbation in the integrating sphere (2 mm diameter shell, 25 mm diameter sphere), the calculation can be broken into two parts: (1) a radiosity calculation of the brightness distribution of the interior of the integrating sphere (Fig. 5-21); and (2) the heating in each layer caused by a ray as a function of the angle between its source and the local surface normal (Fig. 5-22). These two angular distributions are convoluted together to produce a map of the heating distribution in the plastic and ice layers (Fig. 5-23).

The brightness distribution in the integrating sphere is determined from the Radiosity equation:

$$B(\Theta,\Phi) = P(\Theta,\Phi) \times \int \big(B(\theta,\phi)+I(\theta,\phi)\big) \times V(\theta,\phi,\Theta,\Phi)\, dA(\theta,\phi) \qquad (1)$$

where, $B(\Theta,\Phi)$, $R(\Theta,\Phi)$, $I(\theta,\phi)$ are the brightness, reflectance, and light input, respectively, at point (Θ,Φ), and $V(\theta,\phi,\Theta,\Phi)$ is the visibility of point (θ,ϕ) from (Θ,Φ). This is solved by iterating the equation starting with $B(\Theta,\Phi) = 0$, and $I(\Theta,\Phi) = 1$ at the location of the light sources and 0 otherwise. Each iteration corresponds to one absorption/remission step for a photon. Because the average photon bounces only 10 times, this calculation converges quickly. For the results shown in Fig. 5-21, we iterated Eq. (1) thirty times.

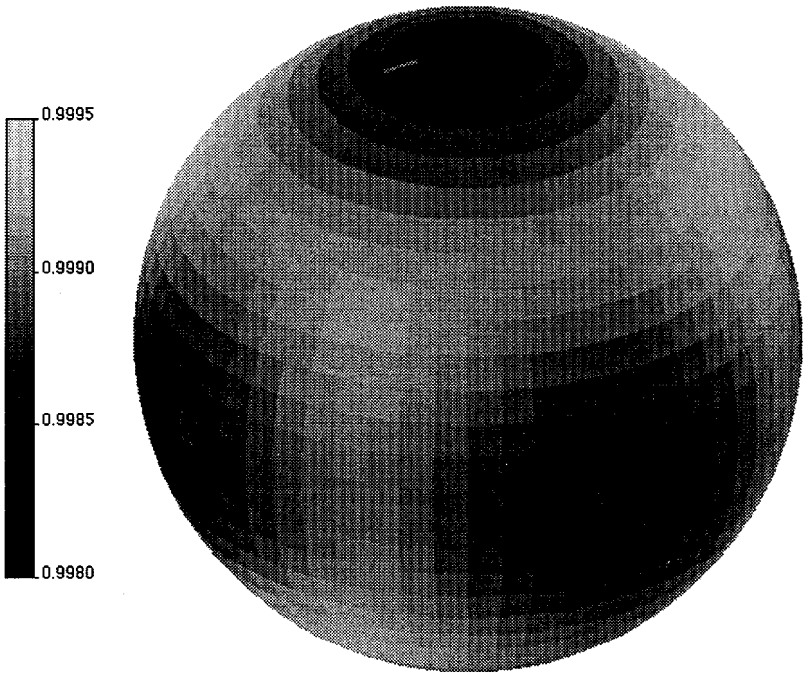

Fig. 5-21. Calculated brightness map of interior of integrating sphere. The inspection holes are black, but otherwise the brightness varies <0.1%.

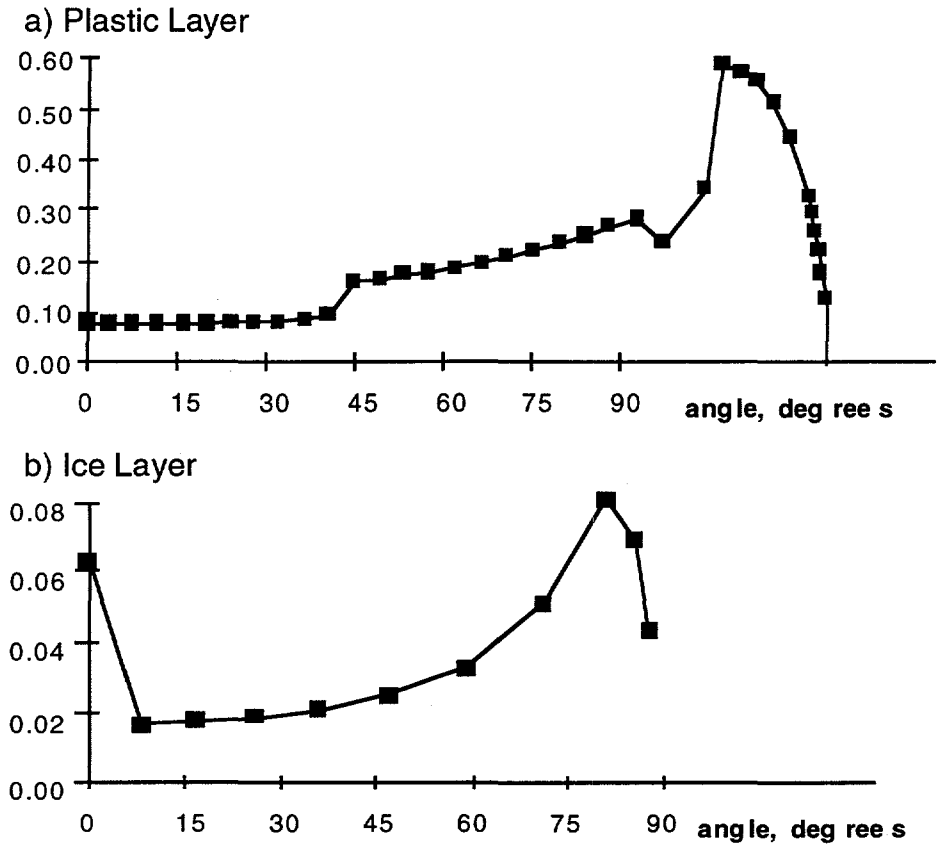

Fig. 5-22. Power absorbed in (a) the plastic layer, and (b) the ice layer as a function of the angle between the source and the local surface normal.

The calculation of the heating caused by each ray was done by ray-tracing. The absorption in each layer was calculated as a function of incident ray angle. The calculation was done for each polarization separately and included multiple reflections within each layer, and reflections back from adjacent layers. An effective path length was calculated from the absorbed power, and used to determine the point at which the ray had entered the layer, and then to backtrack to estimate the location of its source. Because of multiple reflections, the sources were not nearly so localized as this procedure assumes, so the structures shown in the figures below should be considerably smeared out. That would have the consequence of reducing the heating fluctuations shown in Fig. 5-22.

The heating of the shell, $H(\Theta,\Phi)$, is determined from Eq. (2), and the results plotted in Fig. 3(a) for the plastic layer and 3(b) for the ice layer.

$$H(\Theta,\Phi) = \int h\big(\zeta(\Theta,\Phi,\theta,\phi)\big)\, B(\theta,\phi)\, dA(\theta,\phi) \quad . \tag{2}$$

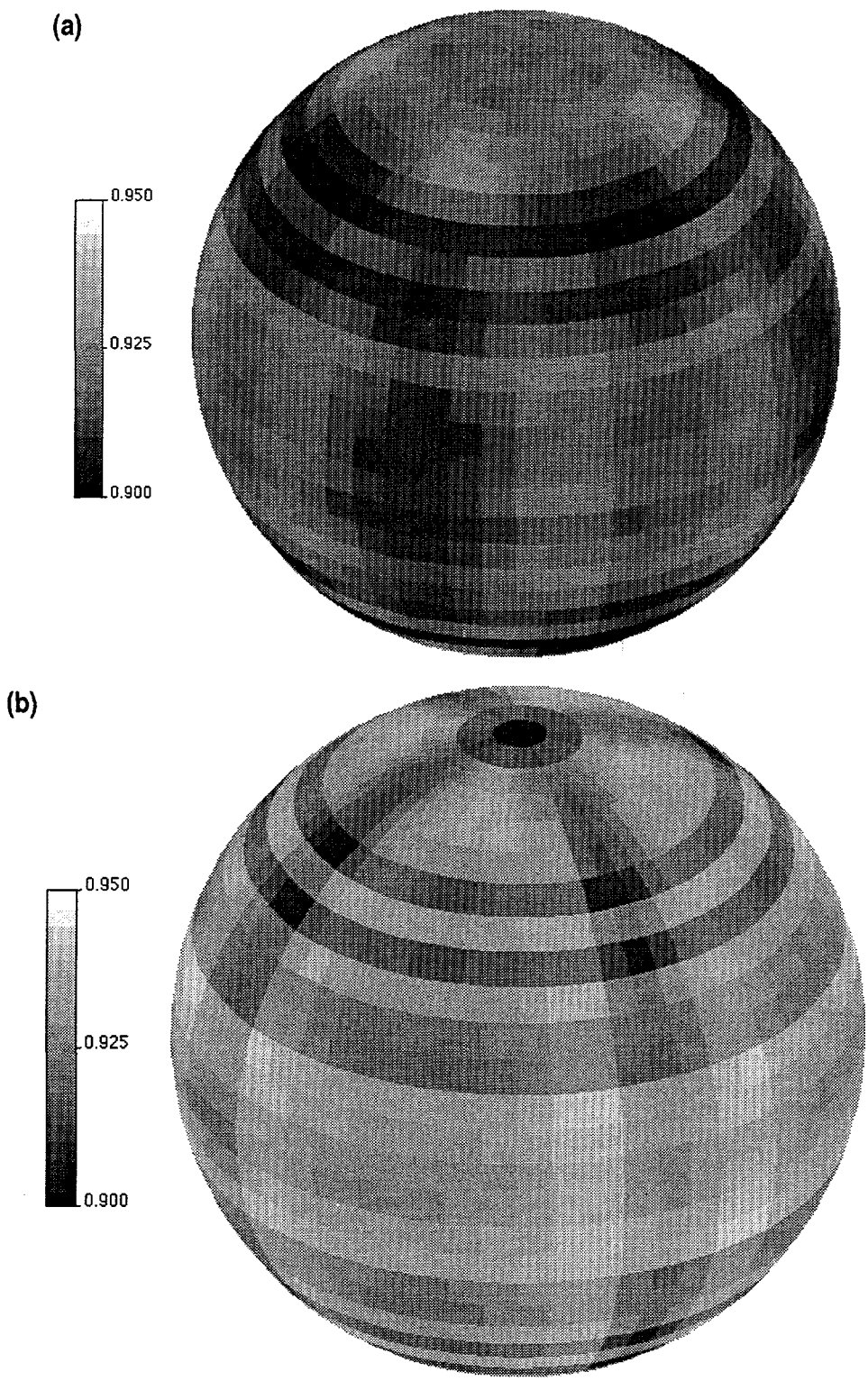

Fig. 5-23. Normalized heat input into (a) plastic layer and (b) ice layer as a function of location on the cryotarget. The values vary by approximately ±1%.

The symmetry of the fluctuations should have the same cubic symmetry as that of the integrating sphere, with cooler regions away from the inspection holes. The pattern is roughly as expected, with fluctuations in temperature of about ±1%. In addition, there are polar bands, which seem too strong to be real. They may just be an artifact of the finite element calculations.

The integrating sphere is very wasteful of light. The shell intercepts <1% of the light emitted from the surface of the sphere, and absorbs <2% of that light in the ice layer. Since photons bounce about ten times before escaping, they get ten chances to be absorbed in the ice layer, and 0.1% of the light injected is absorbed in the ice. Beta decay heats DT ice at 50 mW/cm^3; that corresponds to 35 μW in this modeled cryotarget. A 35 mW laser is required to provide heating equal to beta heating of DT.

Since virtually all the power is lost in the integrating sphere surface or through the inspection holes, the power required scales with the square of those dimensions.

Since refraction and absorption in the plastic layer substantially reduce the heat getting to the ice layer, any reductions in plastic thickness, or absorption would increase the power deposited in the ice, but would require redoing the modeling with new assumptions to predict the size of the change.

In summary, an integrating sphere can be used to heat the ice layer of a NIF capsule with satisfactory uniformity, ±1%. Assumptions in constructing the computer simulation were conservative and would only increase the calculated perturbations from the actual perturbations.

The integrating sphere diameter used in this study, 25 mm, can fit in the current experimental apparatus. An IR-assisted layering experiment would require a >35 mW light source. Such an experiment is under construction at LLNL.

Much more heat is deposited in the plastic layer of the cryotarget than in the ice layer. Any irregularities in that layer will affect the underlying ice temperature. In addition, that heat must be dissipated into the surrounding gas, and buoyancy effects there could also distort the ice temperature. Reducing the plastic thickness from the values used in this work could reduce those problems. Dave Bernat, of GA, produced the sphere mapping of the temperature distributions.

For further information, please contact Dr. R. Stephens (GA)

5.4. FOAM SHELL DEVELOPMENT

This was a joint task with Lawrence Livermore National Laboratory (LLNL). Contributors included Stephen Buckley, Stephan Letts, and Robert Cook (LLNL), Diana Schroen-Carey (WJSA) and Stephen Lambert (STI). This report outlines the work done in FY96, the third and final year of the task whose stated goal was "the production of 1 to 2 mm diameter, 50 mg/cc, low-Z foam shells with 90 to 100 μm walls and a 5 to 10 μm full density overcoat to be used in cryogenic liquid layering experiments".

We successfully produced methacrylate foam shells by droplet generator microencapsulation in FY94. The optical transparency of the foam was poor due to the large (~1 μm) cell size. In FY95, we adapted this microencapsulation process to fine-celled resorcinol-formaldehyde foams to obtain foam shells having the required optical properties. In FY96, we focused upon the full density overcoat. The specifications for the overcoat were conformity to the foam shell, optical transparency, and surface finish of 500 Å RMS or better, "with the potential for further optimization".

Producing conformal, transparent overcoats across a wide range of thicknesses was relatively easy, and we were pleased by the range since the stated goal of 5 to 10 microns was appropriate for current cryogenic experiments, however, it met none of the anticipated target applications. The outer capsule thickness desired for current OMEGA designs is ~1 μm while the projected thickness for NIF designs is 150 to 200 microns. There were two obvious routes to obtaining the NIF design thickness. The first approach was to produce a thin, OMEGA type coating, with very good surface finish which could serve as a substrate for a more standard overcoating process, such as plasma polymerization. This approach had appeal since we have used plasma polymer in cryogenic applications, we know how to apply a barrier layer over plasma polymer, and plasma polymer deposition allows for dopants to be applied within the coating. The second approach was to build the layer in a single process. This approach had the appeal of simplicity. The difficult aspect was obtaining the desired surface finish appropriate for either approach.

5.4.1. Aerogel Foam Shell Production

Resorcinol-formaldehyde (RF) is a low density foam characterized by very small (<<1 μm) cell size. This small cell size scatters very little light, so the foam has excellent optical properties [Ref. 5-14]. The two stage RF chemistry had been developed at LLNL by

Pekala, et al. [Ref. 5-15]. In the first stage, aqueous solutions of resorcinol and formaldehyde react under basic conditions to form nanometer-sized particles. This can take several hours and is dependent upon the concentrations of the reactants and their ratios. In the second stage, under acidic conditions, the particles begin to aggregate and assemble into a stiff interconnected structure that resembles a "string of pearls". This polymeric network fills the original volume of the aqueous solution. It is not possible to directly remove the water without collapsing the polymer structure. The water must be replaced by a solvent which is itself replaced by CO_2. The CO_2 is removed using a supercritical drying technique which never exposes the polymer to the capillary forces of a liquid-gas interface.

Foam shell production begins with the creation of preforms by a triple-orifice droplet generator. The preforms consist of an interior oil-phase droplet which is surrounded by the ungelled aqueous RF solution. This oil-in-water drop is formed by two concentric orifices that are inserted in a tube, i.e., the "third" orifice. This tube delivers an exterior oil phase in an axial flow that strips the droplets off the two orifices. It is this process that sets the outer diameter of the shell as it is a function of the axial flow rate and diameter of the delivery tube. The wall thickness of the shell is determined by the ratio of the flow rates of the interior oil phase and the RF phase. The interior and exterior oil phases need not be chemically identical, in fact, there are advantages to them being different. The critical property for the internal organic phase is that it is density matched to the RF solution. The critical characteristic for the external organic phase is that it has low water solubility. During the production of RF form shells, we explored some of the possible oil phases. Suitable and unsuitable combinations of exterior and interior oil phases are so marked in Table 5-1. Unsuitable combinations resulted in shells with very poor concentricity. (For a complete discussion of the production of RF foam shells, see LLNL Report TAT 95-068, "Resorcinol-Formaldehyde Foam Shell Progress Report".)

TABLE 5-1
COMBINATION OF INTERIOR AND EXTERIOR OIL PHASES

Interior Oil Phase	Exterior Oil Phase	
	Mineral oil + 40 wt.% carbon tetrachloride	Mineral oil + 40 wt.% tetrachloroethylene (TCE)
1-methyl naphthalene	Suitable	Unsuitable
1-methyl naphthalene + 2 wt.% TCE	Unsuitable	Suitable
Mineral oil + 37 wt.% TCE	—	Suitable

5.4.2. Shell Overcoating

Shell overcoating had to meet the task description and had to be chemically compatible with the RF foam and CO_2 drying. Interfacial polymerization was specified as the technique of choice as it was expected to produce conformal coatings with good surface finish. The technique of interfacial polymerization over foam shells was developed at the University of Osaka (ILE) for overcoating methacrylate foam shells [Ref. 5-16]. Isophthaloyl dichloride was reacted with polymers containing many pendant hydroxy groups, such as poly(vinyl alcohol) (PVA), hydroxyethyl cellulose (HEC), and poly(vinylphenol) (PVP).

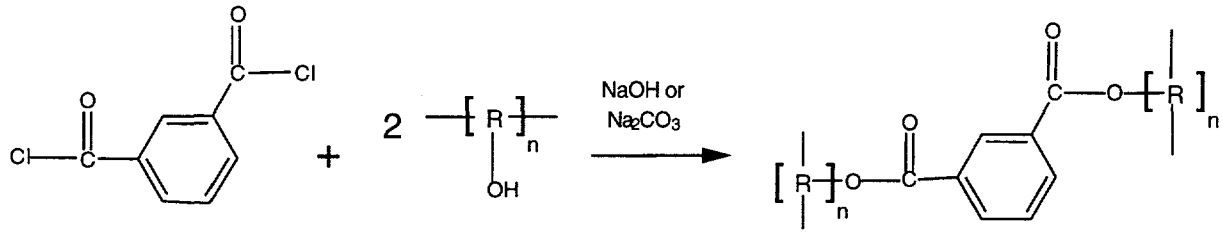

We preferred using the organic acid chloride solution as the interior phase. This minimized the personnel exposure to the acid chlorides and minimized the volume of organic solvent required.

To determine the range of properties possible with the acid chloride chemistry, we set up matrices of experiments that varied the organic phase solvent (cyclohexane, p-chlorotoluene), the acid chloride (sebacoyl chloride, benzoyl chloride, isophthaloyl chloride, and 1,3,5 benzene tricarbonyl chloride), and the aqueous phase reactant (two polymers: PVA, and PVP at 4 molecular weights, and four small molecules: biphenol, bis(4-hydroxyphenol)methane, piperazine, and tris(2-aminoethyl)amine.) We began the experiments by overcoating RF foam shells. This was valuable for proving chemical compatibility and demonstrating the ease with which we could produce conformal coatings. Using the same reaction conditions (such as equivalence of reactants, ambient temperature and twenty minute reaction time) the thickness of the overcoats varied from sub-micron to 150 microns. Representative SEM micrographs of fracture surfaces of the overcoated foam shells are shown in Fig. 5-24. Characterizing the overcoating was often difficult due to the preponderance of RF in the finished shell, therefore, we also made empty shells. Interferograms of two thin walled shells are shown in Fig. 5-25. These interferograms show the extreme thinness of the interfacial walls, and the high degree of uniformity across the wall. Figure 25(a) shows an intact shell with a wall thickness of approximately 0.6 μm. The typical bull's eye pattern is not seen due

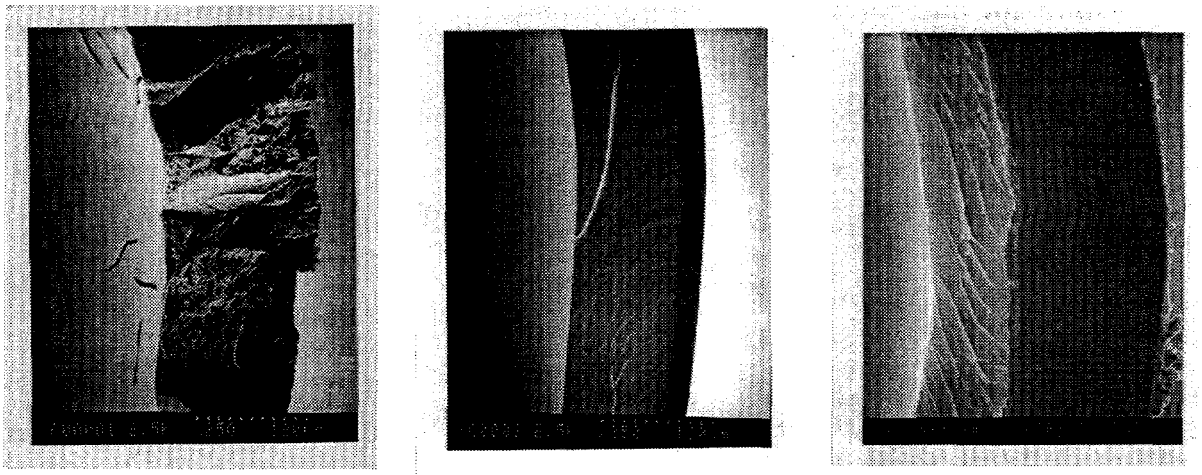

Fig. 5-24. In all three SEM micrographs, the interfacial polymer layer is to the right of a foam layer. The thicknesses are approximately 2 microns, 24 microns, and 150 microns.

to the shell's very high aspect ratio, >1400. There is simply not enough additional polymer at the edges to cause the pattern. Figure 5-25(b) shows a section of a shell wall approximately 0.3 μm thick. Note the consistent one fringe displacement across the film. The high degree of uniformity is a result of the reaction mechanism. The polymer wall builds by the reaction of molecules from both the water and organic phases. The choice of reactants determines the cross-link density of the polymer which determines the wall thickness required to block transport of reactant molecules. Thus, the reaction can be self-limiting.

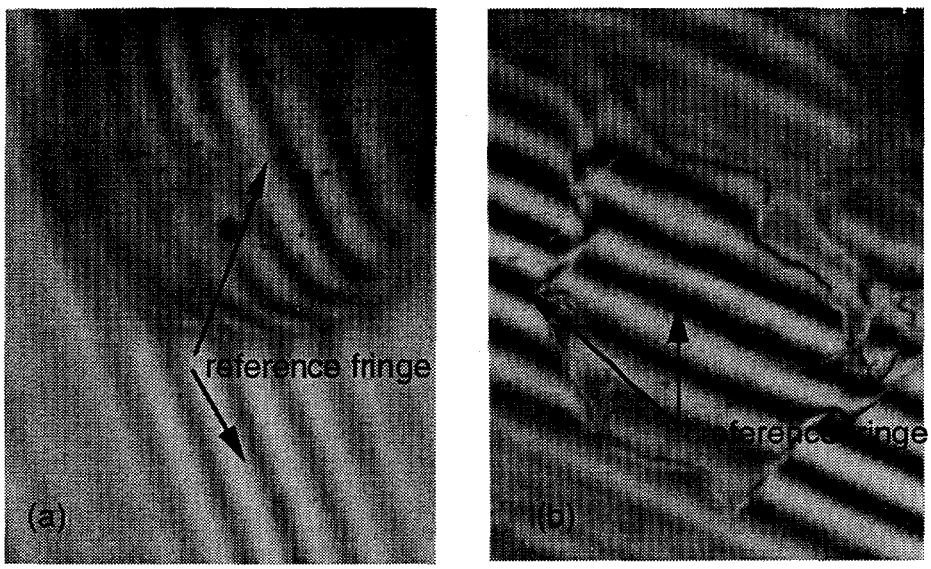

Fig. 5-25. These two interferograms show the extreme thinness of the interfacial walls, and the high degree of uniformity across the wall. (a) shows an intact shell and (b) shows a section of wall from another shell.

Surface finish of the coating was the most elusive specification to characterize, understand, and attain. Characterization was difficult due to the time required for use of techniques such as Atomic Force Microscope (AFM) and SEM and the limitations of each technique. The SEM analysis is limited as it provides qualitative information but not numerical analyses such as a root-mean-square (RMS) value. The AFM analysis was of limited use as we were unable to successfully characterize the thin walled empty shells. Understanding surface finish was further complicated by seemingly random, irreproducible surfaces, especially with thick walled shells. Attaining the desired surface finish was not attained until we discovered the source of the irreproducible results: we discovered that even slight variations in the rinsing of the shells after the reaction could have significant effect on surface. Rinsing with isopropanol produced the most dramatic change, as shown in Fig. 5-26. These two SEM micrographs show shells produced by the same chemistry, but the first shell was rinsed with water while the second shell was rinsed with isopropanol. The water washed surface has a rough, layered appearance, while the isopropanol washed surface has spherical residue laying upon a smooth surface. Unfortunately there was insufficient time to optimize the rinsing protocol, thus, we do not know if we have obtained the best finish possible. Further experiments in this area should be done to determine the optimal solvent(s) and exposure time before any definitive "best" surface finish can be stated. However, the highly cross-linked thin walled shells often produced quite smooth surfaces as can be seen in Fig. 5-27. It appears to be smooth enough to be suitable as an OMEGA type target or as a substrate for additional coating to produce a NIF type target.

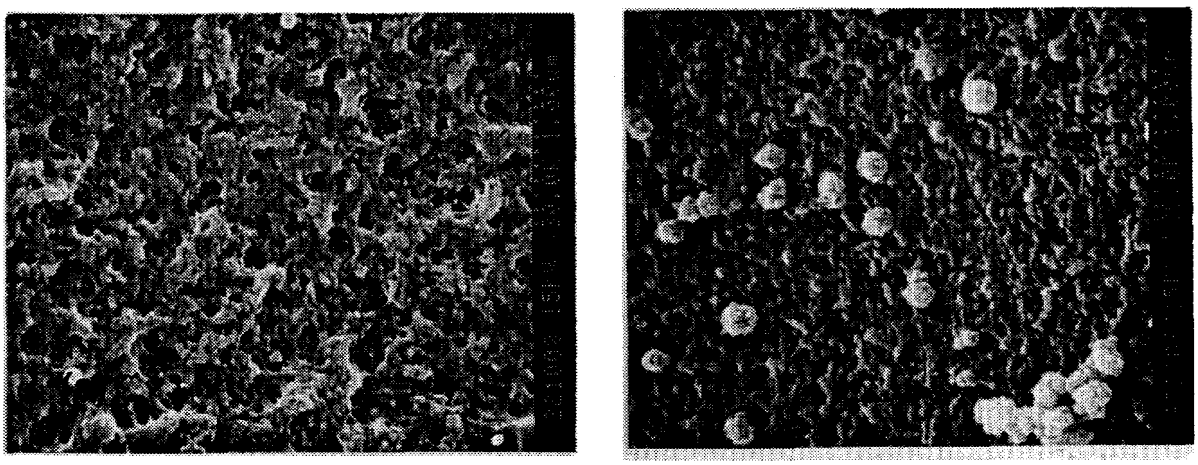

Fig. 5-26. These two micrographs show the change in surface finish that can be attained by changing the rinsing protocol: (a) shows the surface after a water rinse, (b) shows the surface after an isopropanol rinse.

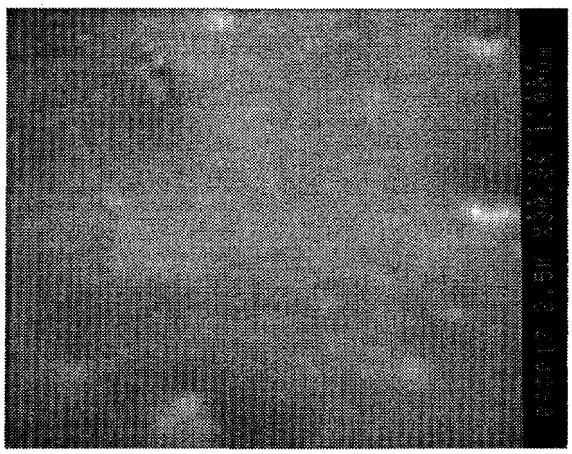

Fig. 5-27. This SEM micrograph shows the surface finish of a thin (<1 micron) wall.

Acknowledgment

We would like to thank Ed Lindsey and Evelyn Fearon, both of LLNL, for their assistance in characterizing shells, especially in the time consuming analysis of surface finish.

For further information, please contact D. Schroen-Carey (WJSA).

5.5 REFERENCES

[5-1] J. R. Miller, Los Alamos Scientific Laboratory Report LA-6245-PR, December 1975, p. 82; *Methods and Apparatus for Producing Cryogenic Inertially Driven Fusion Targets*, U.S. Patent 4,292,340 (January 1987).

[5-2] A. J. Martin, R. J. Simms, and D. L. Musinski, KMS Fusion, Inc. Report No. 1348 (1985, unpublished); A. J. Martin, R. J. Simms, and R. B. Jacobs, *J. Vac. Sci. Technol.* A **6**, 1885 (1988).

[5-3] J. K. Hoffer and L. R. Foreman, *Phys. Rev. Lett.* **60**, 1310 (1988).

[5-4] S. Hann, S. Pollaine, J. Lindl, et al., ICF Quarterly Report **3**, Lawrence Livermore National Laboratory Report UCRL-LR-105821-95-4, p.81, (1995).

[5-5] P. Clark Souers, E. M. Fearon, and R. T. Tsugawa, *Cryogenics* **21**, 667 (1981).

[5-6] P. Clark Souers, E. M. Fearon, and R. T. Tsugawa, *J. Vac. Sci. Technol.* A **3**, 9 (1985).

[5-7] P. Clark Souers, *Hydrogen Properties for Fusion Energy*, (University of California Press, Berkeley, 1986) p. 216.

[5-8] A. G. Robertson, *Aust. J. Phys.* **24**, 445 (1971).

[5-9] General Atomics Inertial Confinement Fusion Annual Report, (GA-A22305, UC-712), p. 5-1, (1995).

[5-10] E. R. Mapoles, J. Sater, J. Pipes, E. Monsler, to be published.

[5-11] T. P. Bernat, E. R. Mapoles, J. J. Sanchez, *Lawrence Livermore National Laboratory Inertial Confinement Fusion Quarterly Report* **1**, No. 2, UCRL-LR-105821-91-2, pp. 57–61(1991).

[5-12] General Atomics Inertial Confinement Fusion Annual Report, (GA-A22305, UC-712), p. 5-9 (1995).

[5-13] G. W. Collins, et al., "Infra-Red Redistribution of D_2 and HD Layers for Inertial Confinement Fusion," J. Vac. Sci. Technol. A **14**, p. 2897 (1996).

[5-14] G. E. Overturf III, R. Cook, S. A. Letts, S. R. Buckley, M. R. McClellan, D. Schroen-Carey, *Fusion Tech.* **28**, 1803 (1995).

[5-15] R. W. Pekala, C. T. Alviso and J. D. LeMay, "Organic Aerogels: A New Type of Ultrastructured Polymer," *Chemical Processing of Advanced Materials*, L. L. Hench and J. K. West, eds. , John Wiley and Sons, Inc., New York, 1992. pp. 671–683.

[5-16] M. Takagi, M. Ishihara, T. Norimatsu, T. Yamanaka, Y. Izawa, and S. Nakai, "Development of Foam Shell with Plastic Ablator for Cryogenic Laser Fusion Target," J. Vac. Sci. Technol. A **11**, 2837 (1993).

6. OMEGA TARGET SYSTEM ENGINEERING

During FY96, significant progress was made in the design of the OMEGA Cryogenic Target System. This included major design changes, reduction in equipment, and process simplifications. In February 1996, a decision was made to relocate the Transfer Station from under the target chamber in "La Cave" to Room 157 and place it in the same glove box as the Fill Station using the Moving Cryostats (MC) to transfer individual targets from Room 157 to La Cave. Making this change reduces congestion under the target tank and will make operation of the Transfer Station independent of target shots since it is no longer in La Cave. A second major design change was the decision to insert and remove targets through the bottom of the cryostats to simplify maintenance. Special emphasis was placed on simplifying the process and equipment to improve operation and maintenance, increasing reliability and safety, and reducing equipment cost. To achieve this a number of process steps and the associated equipment were eliminated.

For the Fill Station these improvements included: replacement of the two cryovalves with one room temperature valve; redesign of the Permeation Cell to seal hydraulically, not mechanically (thus simplifying operating procedures and eliminating one cryostat penetration); insertion and removal of the targets from the bottom; and adopting the LANL dewar design for the cryostat. The Preliminary Design Review for the Fill Station was held at the end of August 1996.

The decision to locate the Transfer Station in Room 157 inside the glove box resulted in a revised design approach for the Cold Transfer System (CTS). The CTS now consists of two major parts: The Cold Transfer Cryostat (two CTCs) and the Cryostat Rail System (CRS), both located within the glove box. The Conceptual Design Review of the CTS was completed. The Conceptual Design Review of the Transfer Station was held in May 1996 and preliminary design has continued.

During the FY96, significant progress was also made in the Cryogenic Target Positioning System (CTPS) design. One major change was that the MC now transports individual targets from room 157 through the hallway to La Cave. The Conceptual Design Review was held in July 1996.

6.1. D_2 EQUIPMENT TESTING

A prototype Fill Station (FS) and CTC have been designed, constructed, and operated at General Atomics with D_2 to demonstrate the fill process and to provide input to the final design.

A series of thermal and mechanical performance tests of the prototype fill station and the cold transfer cryostat were successfully completed. These tests demonstrated acceptable performance of both systems. Modifications to the Fill Station were carried out to improve cool down time and temperature uniformity, and to simplify operation of the equipment.

The process of high pressure filling and transport of cryogenic targets was demonstrated: GDP polymer target shells were filled to high pressures (~1100 atm) with D_2, cooled to below 31 K, removed from the Fill Station and, after verifying fuel filling, cryogenically transported with the Cold Transfer Cryostat. They were then returned to the Fill Station to visually observe retention of the D_2 during the transport and were heated to observe destruction of the targets.

The project milestone entitled "Filled Shell Performance Demonstration" was completed with the filling and cryogenic transport of mounted targets. These tests demonstrate the feasibility of high pressure filling, cooling, and transporting of cryogenic polymer targets with the UR/LLE C-mount design.

Both unmounted and mounted targets were filled. In the first test six unmounted targets had been placed into individual holes in a specially designed multi-shell target rack. The filling with deuterium was accomplished stepwise to a final pressure of ~700 atm, for a total fill time of ~10 hours. Examination of the targets with a long-distance microscope clearly showed a liquid meniscus (Fig. 6-1). The targets were rapidly heated and showed changes in the appearance of the meniscus as heating progressed, followed by sequential explosion of the six targets. Room temperature optical microscope examination of the rack showed only finely divided shards remaining in the target holes.

The second successful deuterium fill was carried out with a target mounted with spider web on a convoluted C-mount supplied by UR/LLE. The target was filled to ~1100 atm with D_2, cooled to ~20 K to condense the deuterium in the target, pumped to remove the excess deuterium, picked up by the CTC, transported to the mobile power cart, and returned to the permeation cryostat. In contrast to the unmounted filled targets which burst when heated, the

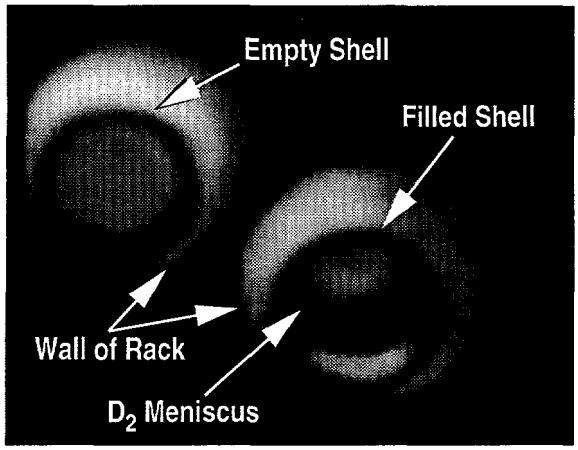

Fig. 6-1. Filled shells have distinctive appearance (filled shell on right).

mounted target exhibited rapid emptying of the deuterium upon heating. Our hypothesis is that the GDP coating developed micro-cracks through which the deuterium could escape, but the parylene overcoat (not present on unmounted targets) prevented catastrophic failure of the shell. Microscope and SEM investigation confirmed the presence of cracks in the shell after loss of the deuterium.

A third fill demonstration was conducted with shells at various stages of the mounting process. The objective of this fill was to systematically examine the effects of mounting on survival during filling. Five targets (one C-mount and four unmounted shells) were loaded into a single target rack and filled to ~1100 atm with D_2. The target shells consisted of the C-mount, two unmounted shells (previously burst tested at 10 atm to verify their integrity), an unmounted shell with no burst test, and one demounted (mounted on a C-mount and cut from the spider webs) shell. Visual examination of the five cryogenic shells after filling showed the characteristic meniscus in each target that we have observed previously in filled shells. Upon rapid heating, all five shells exhibited first a redistribution of the deuterium (loss of meniscus) followed by violent destruction of the shell as before. All the shells failed within a fairly small time frame, and indicated no significant difference between the mounted and unmounted shells with respect to cryogenic burst pressure.

Overall, the thermal and mechanical testing and the prototype equipment operations during the D_2 demonstration fills led to simplification of the process and equipment. As a result of this testing, the emphasis on simplification has been incorporated into the design of all the DT equipment, not just the fill station components.

6.2. DT EQUIPMENT DESIGN

The design of the DT equipment was started in FY96 and culminated in a Preliminary Design Review held at the end of August 1996.

6.2.1. FILL STATION (FS)

In addition to meeting the design requirements, special emphasis was placed on simplification of the equipment. The goals of this simplification effort were to improve operation and maintenance, increase reliability and safety, and to reduce equipment cost. Lessons learned from the prototype fill station were incorporated in the new design. These include: replacement of the two cryovalves with one room temperature valve; redesign of the Permeation Cell to seal hydraulically, not mechanically (thus eliminating one penetration in the cryostat and complex operating procedures); insertion and removal of the targets from the bottom; and adopting the LANL dewar design for the cryostat. A sketch of the DT Fill Station is shown in the Fig. 6-2.

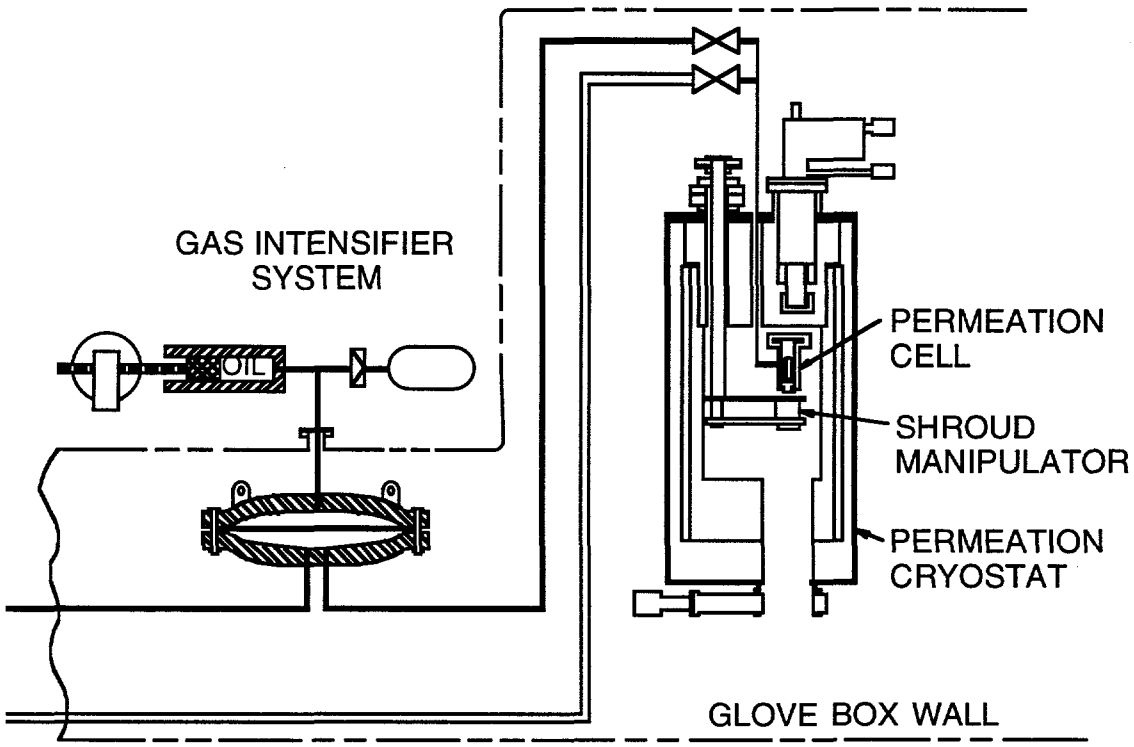

Fig. 6-2. DT Fill Station

The process begins when a group of four mounted targets in a target rack are placed inside the permeation cell by the CTC. The target rack is locked in place by a breech lock and the pressure seal made by helium gas pressing on a diaphragm. The existing UR/LLE Tritium Filling Station supplies room temperature DT at pressures up to 150 atm. The pressure is then boosted to a maximum of 1500 atm by the Gas Intensifier System. This pressure must be applied slowly to allow the DT to permeate through the wall of the targets. Once the desired pressure is obtained, the permeation cell is cooled to approximately 20 K to condense the DT. The permeation cell is inside the permeation cryostat which operates at a steady state temperature of about 20 K. The cryostat is a large mouth dewar with the mouth sealed by an insulating plug. This allows access to the internal components without the use of cryogenic flange seals. Cooling is provided through the use of cryocoolers and liquid nitrogen. The DT fuel which is in the Permeation Cell but not inside the target is pumped back to the LLE Tritium Filling Station. The CTC then removes the cold, filled targets from the Fill Station and moves them to the Transfer Station.

6.2.2. COLD TRANSFER SYSTEM (CTS)

The design of the CTS was started in FY96 and the conceptual design was completed. The design of the DT system was based on the design of the prototype and incorporated the lessons learned during testing with D_2. However, the decision to move the Transfer Station in Room-157 into the glove box resulted in a revised design approach for the CTS. The CTS now consists of two major parts: The two CTCs and the CRS. Both the CTC and the CRS are located within the glove box. A sketch of the CTS is shown in Fig. 6-3.

The CTC places the room temperature target rack with unfilled targets into the Fill Station, specifically, the Permeation Cell, seals the cell, removes the cold target rack from the Permeation Cell and the Permeation Cryostat, and inserts the target rack into the Transfer Station while maintaining the required temperature and atmosphere (nominally 20 K and 50 mTorr of helium, respectively). The CRS moves the CTC from the entry port located on the underside of the Fill Station to the entry port located on the underside of the Transfer Station (TS).

The Cryostat Rail System, which accommodates up to two CTCs, consists of pairs of rails on which the CTCs move between the Fill Station and the Transfer Station. There is a main rail line broken into four segments and a spur line for potential storage of filled targets

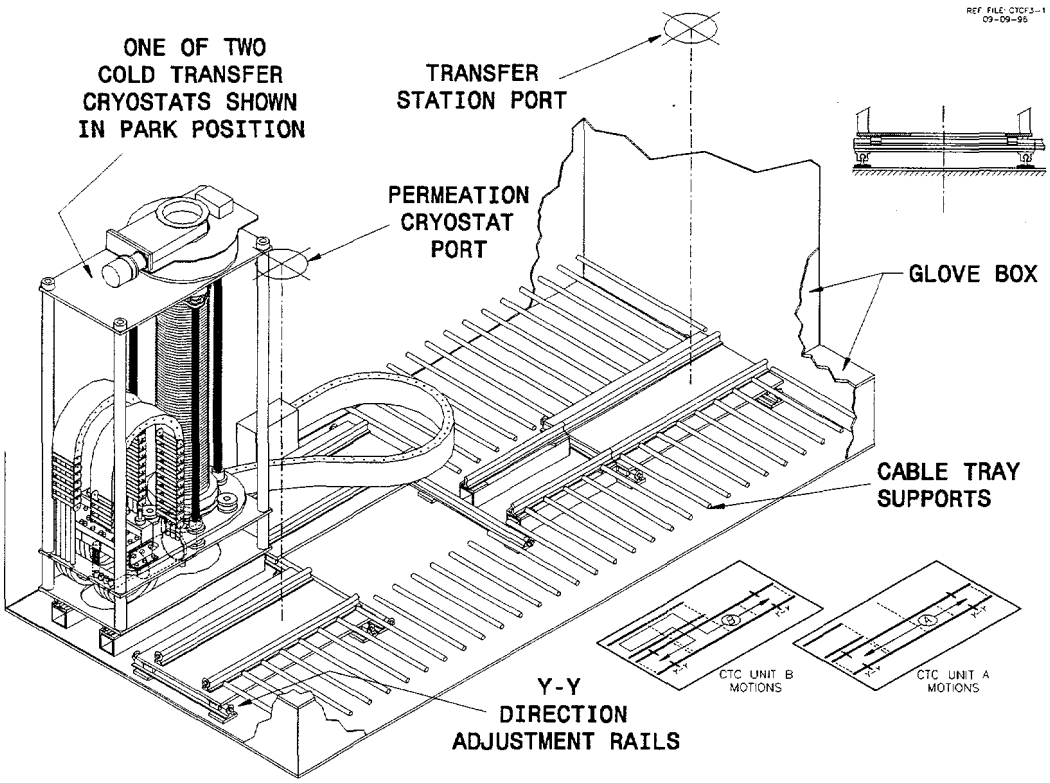

Fig. 6-3. The over-all layout of the Cold Transfer System with one of the Cold Transfer Cryostats removed. The motions of the two cryostats, A and B, are shown in the lower right.

inside one of the CTCs. The design allows the CTCs to be adjusted laterally to align with the entry ports of the FS and TS and to be switched between the main line and the spur line.

The CTC consists of a flexible outer metal bellows that forms the outer vacuum wall of the CTC, a shroud that cocoons the Target Rack/Cell Plug (TR/CP) in a leak tight chamber for cold transfer, and a manipulator that is located inside the shroud of the CTC and is used to grasp the TR/CP. When a CTC enters or leaves the Fill Station or the Transfer Station, its shroud is removed by a shroud manipulator provided by the FS or TS. This exposes the TR/CP manipulator for TR/CP pick-up or delivery. The manipulator uses a spring-loaded ball plunger mechanism pulled by a cable to grasp the TR/CP. The manipulator is set upon a compliance plate that allows compliance in any direction and ± 2° of tilt. The Shroud is cooled through a copper cold finger attached to a cryocooler. A triad of ball screws is used to drive the shrouded manipulator up past the gate valve into the PC or TS while collapsing the flexible metal bellows that forms the outer vacuum wall of the CTC. Loading the empty targets is accomplished by removing the shrouds and placing the TR/CP into the CTC manually. A sketch of a CTC is shown in Fig. 6-4.

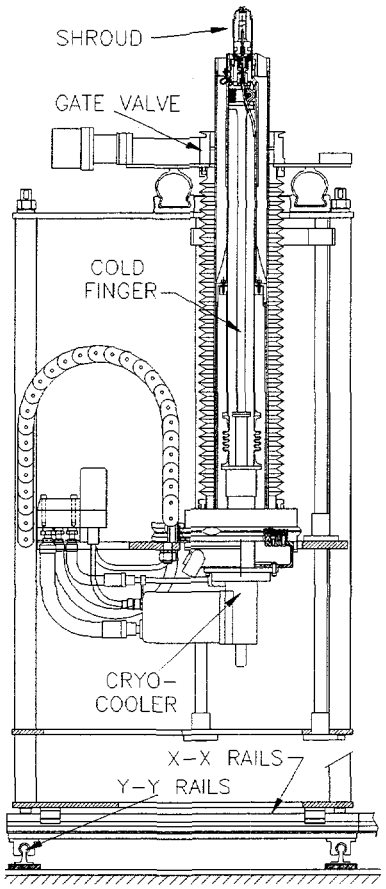

Fig. 6-4. A Cold Transfer Cryostat shown with shroud partially extended.

6.2.3 TRANSFER STATION

The design of the Transfer Station continued in FY96 and a Conceptual Design Review was held in May. The Transfer Station removes one filled target from the target rack and places it onto the Moving Cryostat stalk. A sketch of the Transfer Station is shown in Fig. 6-5.

The CTC mates with a gate valve on the bottom of the Transfer Station. After the CTC is raised inside the Transfer Station, the CTC shroud is removed by the shroud manipulator. Next the target rack lid is gripped by the Target Rack Lid Remover and raised to expose the filled targets. The target rack is then rotated to align the desired target with the Target Manipulator.

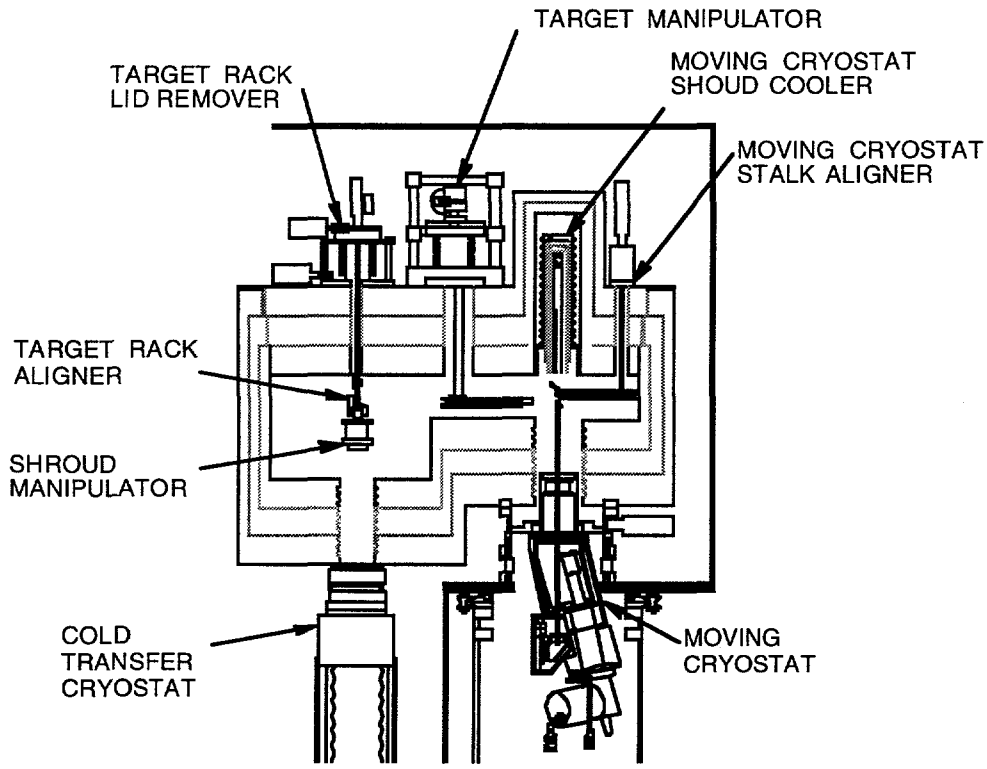

Fig. 6-5. Transfer Station.

On the other side of the Transfer Station is a second gate valve at the bottom which is connected to a horizontal flange on the glove box wall. The MC airlock attaches to the other side of this flange. The MC is brought up inside the Transfer Station by a rail system, and the MC shroud is removed and cooled by the MC Shroud Cooler.

To place a target in the Moving Cryostat, a single mounted target is removed from the target rack by the Target Manipulator. The Target Manipulator then rotates 180 degrees and places the target onto the Moving Cryostat stalk. The MC shroud is replaced and the MC lowered down into its airlock.

6.2.4 CRYOGENIC TARGET POSITIONING SYSTEM (CTPS)

During FY96, significant progress was made in the CTPS design. The selection was made between the Cryogenic Elevator and Moving Cryostat concepts and the scope of the CTPS was expanded to incorporate transfer of individual targets from Room-157 to La Cave. The design of the selected concept has proceeded through the conceptual design phase into preliminary and final design.

The MC concept was selected over the Cryogenic Elevator. This selection was made after successfully testing of the prototype Cryogenic Parting Joint. This joint permits easy and smooth removal of the layering shroud from the target for the laser shot while providing good heat transfer from the shroud to the cryocooler. Verification that the predicted heat transfer rates could be achieved across the Parting Joint's metal surfaces permitted selection of the MC concept.

Implementation of the MC concept requires a Transfer Station (TS) in which individual targets are loaded into the MC. Initially the TS was considered part of the CTPS and located under the target tank in La Cave. In February, a decision was made, at the request of LLE, to locate the TS in the tritium fill glove box in Room 157 and use the MC to transfer the target through the hallway to La Cave. Making this change reduces congestion under the target tank and will permit manned operation of the TS at shot time since it is no longer in La Cave. The new scenario requires that the MC be housed in a secondary containment vessel, the Moving Cryostat Transfer Cart (MCTC).

Once these decision had been agreed on, the conceptual design of the balance of the CTPS proceeded rapidly. This allowed us to have a conceptual design review in July. Since then, significant progress has been made in the design of each major subsystem of the CTPS. A detailed 3-D CAD model of the MC defined each part of this intricate assembly. Engineering sketches and layouts defined space allocation and functional operation of the MCTC, Moving Cryostat Elevator (MCE), Lower Pylon (LP) and Upper Pylon (UP). Design decisions addressed each of the MCs numerous technical challenges and the concepts were tested in the laboratory as necessary.

Various concepts for the MCTC were developed. Key MCTC design issues addressed included the overall package size, the "umbilical" which provides pneumatics, instrumentation, and power to the MC, the method of elevating the MC from the MCTC, and the logistics of moving from one part of the LLE facility to another. The umbilical spooler is based on commercial designs but with significant modifications to fit within the available space. After a trade study of several designs, Serapid Corp.'s "rigid chain" was selected as the basis for the Moving Cryostat Elevator, which pushes the Moving Cryostat from its resting position in the MCTC to the elevations that it must reach in the Transfer Station, the Maintenance Station, and at the Target Chamber center.

Fixed position location of the MC at tank center is a major issue. It is provided by a kinematic mount consisting of three hardened tooling balls, located on the MC, which mate

with cone, groove and plane fiducials at the top of the LP. Fine target positioning is provided by commercial room temperature piezoelectric screw x-y-z micro positioning stage.

A piezoelectric screw driven rotary stage provides 360 degrees of rotation which permits characterization by Phase Shift Interferometric Tomography, as developed by LLE, and rotational micro positioning to place the support wire of the target C-mount between laser beams. The positioning stages are located in a room temperature region near the base of the Moving Cryostat and act through a flexure mounted target support stalk to position the cryogenic target. The compound target support stalk provides vibration resistant target support while minimizing heat transfer from the micropositioner region to the cryogenic region of the MC. An elastomeric pneumatic seal contains low pressure helium exchange gas and provides the primary tritium boundary.

Design concepts were developed for the Lower Pylon (LP) and the Upper Pylon (UP). The LP design effort primarily concentrated on interface issues and support of the MC for characterization. UP design effort focused on the shroud puller, which removes the MC shroud assembly so that the target can be shot, and the support structure which the UP. The current shroud puller concept uses a linear motor to provide the force, acceleration, and speed required to remove the shroud before it is heated significantly.

For further information, please contact Dr. G. Besenbruch (GA).

7. PUBLICATIONS

Alexander, N., "Cold Transfer System for Omega Cryogenic Target System," in the *Proceedings of the Eleventh Target Fabrication Specialists' Meeting*, Orcas Island, Washington, September 8–12, 1996.

Alexander, N., Besenbruch, G., Baugh, W., Beal, C., Boline, K., Brown, L., Egli, W., Follin, J., Gibson, C., Goodin, D., Gram, R., Hansink, M., Hoffman, E., Lee, W., Letzring, S., Mangano, R., McDaniels, J., Nobile, A., Nasise, J., Schultz, K., Stemke, R., Torres, T., "The Cryogenic Target Handling System for the Omega Laser," in the *Proceedings of the Sixteenth IAEA Fusion Energy Conference*, Montreal, Canada, October 7–11, 1996.

Bahrs, T., Hendricks, C., Walsh, T., Motta, B., "Techniques for Assembly of High-Quality Polymeric Thin-Film Targets," in the *Proceedings of the Eleventh Target Fabrication Specialists' Meeting*, Orcas Island, Washington, September 8–12, 1996.

Bernat, D., Stephens, R., "Algorithm for Better X-Radiography Analyses," in the *Proceedings of the Eleventh Target Fabrication Specialists' Meeting*, Orcas Island, Washington, September 8–12, 1996.

Besenbruch, G., "Omega Cryogenic Target System Status," in the *Proceedings of the Eleventh Target Fabrication Specialists' Meeting*, Orcas Island, Washington, September 8–12, 1996.

Bittner, D., Monsler, E., Collins, G., Letts, S., Tiszauer, D., Feit, M., Mapoles, E., Bernat, T., "Forming and Smoothing D_2 and HD Layers for ICF by Infra-Red Heating," in the *Proceedings of the Eleventh Target Fabrication Specialists' Meeting*, Orcas Island, Washington, September 8–12, 1996.

Boline, K., Brown, L., "Cryogenic Target Positioning System for Omega," in the *Proceedings of the Eleventh Target Fabrication Specialists' Meeting*, Orcas Island, Washington, September 8–12, 1996.

Boone, T., "Large Chlorinated Polymer Shell Production via Microencapsulation: Process Development and Optimization," in the *Proceedings of the Eleventh Target Fabrication Specialists' Meeting*, Orcas Island, Washington, September 8–12, 1996.

Buckley, S., Letts, S., Wilemski, G., Fearon, E., Vu, D., Cook, R., Schroen-Carey, D., "Processing and Properties of NIF Scale Targets Using Interfacial Polycondensation," in the *Proceedings of the Eleventh Target Fabrication Specialists' Meeting*, Orcas Island, Washington, September 8–12, 1996.

Burmann, J., Mapoles, E., "Cryogenic Testing of Liquid and Solid Layering Cells," in the *Proceedings of the Eleventh Target Fabrication Specialists' Meeting*, Orcas Island, Washington, September 8–12, 1996.

Burnham, A., Alford, C., Dittrich, T., Makowiecki, D., Wallace, R., Honew, E., King, C., Steinman, D., "Evaluation of B_4C as an Alblator Material for NIF Capsules," in the *Proceedings of the Eleventh Target Fabrication Specialists' Meeting*, Orcas Island, Washington, September 8–12, 1996.

Collins, G., et al., "Infra-red Redistribution of D_2 and HD Layers for Inertial Confinement Fusion," J. Vac. Sci. Technol. A **14**, 2897 (1996).

Czechowicz, D., Elsner, F., Mcquillan, B., Sixtus, M., "The Manufacture of PAMS Shells by Osaka Droplet Generator," in the *Proceedings of the Eleventh Target Fabrication Specialists' Meeting*, Orcas Island, Washington, September 8–12, 1996.

Egli, W., "Cryogenic Hohlraum Test Apparatus for National Ignition Facility (NIF)," in the *Proceedings of the Eleventh Target Fabrication Specialists' Meeting*, Orcas Island, Washington, September 8–12, 1996.

Gibson, C., "Preliminary Design of the DT Fill Station for the Omega Cryogenic Target System," in the *Proceedings of the Eleventh Target Fabrication Specialists' Meeting*, Orcas Island, Washington, September 8–12, 1996.

Gibson, J., Greenwood, A., Steinman, D., "Wall Thickness Variation Measurement," in the *Proceedings of the Eleventh Target Fabrication Specialists' Meeting*, Orcas Island, Washington, September 8–12, 1996.

Goodin, D., Alexander, N., Baugh, W., Gibson, C., Mangano, R., Stemke, R., Torres, T., "Demonstration of Filling of Polymer Targets with the Omega D_2 Fill Station," in the *Proceedings of the Eleventh Target Fabrication Specialists' Meeting*, Orcas Island, Washington, September 8–12, 1996.

Hendricks, C., Walsh, T., Motta, B., Bahrs, T., "Reduction of Random Variables in the Production of Polymeric, Thin Film Targets," in the *Proceedings of the Eleventh Target Fabrication Specialists' Meeting*, Orcas Island, Washington, September 8–12, 1996.

Hoffman, E., "Design of the Transfer Station for the Omega Cryogenic Target System," in the *Proceedings of the Eleventh Target Fabrication Specialists' Meeting*, Orcas Island, Washington, September 8–12, 1996.

Hoppe, M., Stephens, R., "Characterization of Dopants in ICF Targets," in the *Proceedings of the Eleventh Target Fabrication Specialists' Meeting*, Orcas Island, Washington, September 8–12, 1996.

Husband, D., Stephens, R., "Making ICF Mandrels of Poly-Alpha-Methylstyrene Using a Drop Tower," in the *Proceedings of the Eleventh Target Fabrication Specialists' Meeting*, Orcas Island, Washington, September 8–12, 1996.

James, W., Morosoff, N., Stephens, R., "Properties of Beryllium Loaded Plastic Films," in the *Proceedings of the Eleventh Target Fabrication Specialists' Meeting*, Orcas Island, Washington, September 8–12, 1996.

Kaae, J., "Tool Design for Cutting Conically Shaped Reentrant Holes in Hohlraum Mandrels," in the *Proceedings of the Eleventh Target Fabrication Specialists' Meeting*, Orcas Island, Washington, September 8–12, 1996.

Kim, K., Feng, Q., "A Novel Technique for Noncontact Coating of Microspheres Using Acoustic Levitation and Modulated Charged Liquid Cluster Beam," in the *Proceedings of the Eleventh Target Fabrication Specialists' Meeting*, Orcas Island, Washington, September 8–12, 1996.

Lambert, S., Overturf, G., Wilemski, G., Letts, S., Cook, C., "Fabrication of Low-Density Foam Shells from Resorcinol-Formaldehyde Aerogel," in the *Proceedings of the*

Eleventh Target Fabrication Specialists' Meeting, Orcas Island, Washington, September 8–12, 1996.

Letts, S., D., Buckley, S., Fearon, E., Hamilton, K., Cook, R., Schroen-Carey, "The Role of Reactant Transport in Determining the Properties of NIF Shells Made by Interfacial Polycondensation," in the *Proceedings of the Eleventh Target Fabrication Specialists' Meeting*, Orcas Island, Washington, September 8–12, 1996.

Mapoles, E., Sater, J., Monsler, E., Pipes, J., "Smoothing of Solid DT ICF Targets by Electrical Heating," in the *Proceedings of the Eleventh Target Fabrication Specialists' Meeting*, Orcas Island, Washington, September 8–12, 1996.

McQuillan, B., Czechowicz, D., Nikroo, A., Elsner, F., Hoppe, M., Steinman, D., Miller, W., "Overview of the PAMS/GDP Process to Produce Shells," in the *Proceedings of the Eleventh Target Fabrication Specialists' Meeting*, Orcas Island, Washington, September 8–12, 1996.

McQuillan, B., Czechowicz, D., Sixtus, M., "Control of PAMS Shell Outside Diameter and Wall on the Osaka Droplet Generato," in the *Proceedings of the Eleventh Target Fabrication Specialists' Meeting*, Orcas Island, Washington, September 8–12, 1996.

McQuillan, B., Elsner, F., "Sonication of Wet PAMS Shells to Improve Yield," in the *Proceedings of the Eleventh Target Fabrication Specialists' Meeting*, Orcas Island, Washington, September 8–12, 1996.

Miller, W., Brown, L., Gibson, J., Grant, S., Hoppe, M., Woodhouse, D., "Large Glass Shells-The Effects of Helium and Water Vapor," in the *Proceedings of the Eleventh Target Fabrication Specialists' Meeting*, Orcas Island, Washington, September 8–12, 1996.

Miller, W., Brown, L., Grant, S., Woodhouse, D., "Modifications to Drop Tower Used for Glass Capsule Production at General Atomics," in the *Proceedings of the Eleventh Target Fabrication Specialists' Meeting*, Orcas Island, Washington, September 8–12, 1996.

Morosoff, N., James, W., Stephens, R., "Production of Beryllium Loaded Plastic Films," in the *Proceedings of the Eleventh Target Fabrication Specialists' Meeting*, Orcas Island, Washington, September 8–12, 1996.

Motta, B., Hendricks, C., Walsh, T., Bahrs, T., "Metal Coatings on Polymer Films," in the *Proceedings of the Eleventh Target Fabrication Specialists' Meeting*, Orcas Island, Washington, September 8–12, 1996.

Nikroo, A., Hoppe, M., McQuillan, B., "Titanium Doped Glow Discharge Polymer Films," in the *Proceedings of the Eleventh Target Fabrication Specialists' Meeting*, Orcas Island, Washington, September 8–12, 1996.

Nikroo, A., Hoppe, M., Woodhouse, D., "Deposition and Characteristics of Chlorine Doped Glow Discharge Polymer Films," in the *Proceedings of the Eleventh Target Fabrication Specialists' Meeting*, Orcas Island, Washington, September 8–12, 1996.

Nikroo, A., Hoppe, M., Woodhouse, D., Steinman, D., "Production of Doped and Undoped Glow Discharge Polymer Mandrels by the Depolymerizable Mandrel Technique," in the *Proceedings of the Eleventh Target Fabrication Specialists' Meeting*, Orcas Island, Washington, September 8–12, 1996.

Nikroo, A., Pontelandolfo, J., Steinman, D., "Alternative Permeation Barriers to Polyvinylalcohol for Nova Sized Mandrels," in the *Proceedings of the Eleventh Target Fabrication Specialists' Meeting*, Orcas Island, Washington, September 8–12, 1996.

Pontelandolfo, J., "Casting of Thick Deuterated Polyethylene Films," in the *Proceedings of the Eleventh Target Fabrication Specialists' Meeting*, Orcas Island, Washington, September 8–12, 1996.

Schneidmuller, C., "Planning and Control of the ICF Target Support Tasks," in the *Proceedings of the Eleventh Target Fabrication Specialists' Meeting*, Orcas Island, Washington, September 8–12, 1996.

Schroen-Carey, D., Letts, S., Buckley, S., "Analysis of the Effect of pH on Poly(vinylphenol)," in the *Proceedings of the Eleventh Target Fabrication Specialists' Meeting*, Orcas Island, Washington, September 8–12, 1996.

Schroen-Carey, D., Letts, S., Buckley, S., Cook, R., "Characteristics of Barrier Layers Produced on R/F Foam Shells by Acid Chloride Interfacial Polymerization," in the *Proceedings of the Eleventh Target Fabrication Specialists' Meeting*, Orcas Island, Washington, September 8–12, 1996.

Sheliak, J., Hoffer, J., Sanchez, J., Collins, G., "Heat-Assisted Layering of Solid Deuterium in a Toroidal Cavity," in the *Proceedings of the Eleventh Target Fabrication Specialists' Meeting*, Orcas Island, Washington, September 8–12, 1996.

Steinman, D., Czechowicz, D., Miller, W., Nikroo, A., "Nova Composite Capsules Made Using PAMS Mandrels," in the *Proceedings of the Eleventh Target Fabrication Specialists' Meeting*, Orcas Island, Washington, September 8–12, 1996.

Stemke, R., "Optical Methods for Viewing Targets," in the *Proceedings of the Eleventh Target Fabrication Specialists' Meeting*, Orcas Island, Washington, September 8–12, 1996.

Stephens, R., "Light Scattering Limitations to Interferometric Characterization of Foam Shells," Fusion Technol. **28**, 1809 (1995).

Stephens, R., Collins, G., "Analysis of Performance of Integrating Sphere of IR Enhanced DT Ice Layering," in the *Proceedings of the Eleventh Target Fabrication Specialists' Meeting*, Orcas Island, Washington, September 8–12, 1996.

Walsh, T., Hendricks, C., Motta, B., Bahrs, T., "Techniques for Characterizing High-Quality Polymeric Thin-Film Targets," in the *Proceedings of the Eleventh Target Fabrication Specialists' Meeting*, Orcas Island, Washington, September 8–12, 1996.